

5-2019

Silicon Based Schottky Diodes and MOS Capacitors for Sensing Singly and Multiply Charged Ions with Low Kinetic Energy

Daniel Blaine Cutshall III
Clemson University

Follow this and additional works at: https://tigerprints.clemson.edu/all_dissertations

Part of the [Electrical and Computer Engineering Commons](#)

Recommended Citation

Cutshall, Daniel Blaine III, "Silicon Based Schottky Diodes and MOS Capacitors for Sensing Singly and Multiply Charged Ions with Low Kinetic Energy" (2019). *All Dissertations*. 2399.

https://tigerprints.clemson.edu/all_dissertations/2399

This Dissertation is brought to you for free and open access by the Dissertations at TigerPrints. It has been accepted for inclusion in All Dissertations by an authorized administrator of TigerPrints. For more information, please contact kokeefe@clemson.edu.

SILICON BASED SCHOTTKY DIODES AND MOS CAPACITORS
FOR SENSING SINGLY AND MULTIPLY CHARGED
IONS WITH LOW KINETIC ENERGY

A Dissertation
Presented to
the Graduate School of
Clemson University

In Partial Fulfillment
of the Requirements for the Degree
Doctor of Philosophy
Electrical Engineering

by
Daniel Blaine Cutshall II
May 2019

Accepted by:
Dr. William R. Harrell, Committee Chair
Dr. Chad Sosolik
Dr. Eric Johnson
Dr. Pingshan Wang

ABSTRACT

This study provides the foundation for the development of radiation detection technology of slow ions by investigating the fundamental interactions of slow ion beams with electronic devices. Silicon samples with a 50 nm oxide layer were irradiated with 1 keV Ar^{Q+} beams ($Q = 4, 8, \text{ and } 11$) at normal incidence in order to investigate the relatively unexplored effects of slow highly charged ions (HCIs) on electronic devices. After irradiation, an array of metal contacts was deposited onto the oxidized silicon samples to create metal oxide semiconductor (MOS) capacitors, which were then characterized using high frequency capacitance-voltage (C-V) measurements. The slow HCI irradiation was found to result in stretchout and shifting of the C-V curves, indicating the presence of dangling Si bond defects at the semiconductor/oxide interface and trapped oxide charge, respectively. Near quadratic charge state dependencies were also observed for both the stretchout and the shift seen in the C-V curves, in agreement with charge state dependent stopping power of HCIs previously reported.

The interaction of slow singly charged ions with Schottky diodes was also investigated, in part to serve as a baseline for experiments with slow HCIs by isolating the effects of the kinetic energy of the ions. Diodes with two different Schottky contact thicknesses (~ 26 nm and ~ 360 nm) were irradiated by Na^+ beams at normal incidence with energies 0.5 keV, 1.0 keV, 1.5 keV, and 2.0 keV. No instantaneous change in diode current was observed while the diodes were under irradiation; however, noticeable changes in Schottky barrier height, ideality factor, and reverse leakage current were noted after irradiation. The diodes irradiated at 2.0 keV showed signs of degradation consistent

with reports from the literature, but at the three lower ion beam energies the diodes showed an improvement in the ideality factor accompanied by an increase in Schottky barrier height and an initial decrease in reverse leakage current. Although the direct mechanism for these diode improvements is not fully understood, it is proposed that the changes arise from increased spatial homogeneity of the Schottky barrier height across the diode.

ACKNOWLEDGMENTS

First and foremost, I would like to thank my wife Maria for her constant and unconditional support of my endeavors. Her encouragement and belief in my choices helped me through the particularly difficult days and the times when it seemed like there was no end in sight. I cannot imagine being able to complete my degree without her support.

I am extremely thankful to my advisor Dr. William R. Harrell, without whom my research would not have been possible. He taught me all of the technical material I needed to know in order to perform my research, helped me learn to use all of the equipment in his lab, and also provided me guidance in my professional development. The lessons he taught me have led me to become a better researcher and a better educator.

I also owe a great debt of gratitude to the other members of my committee, particularly the co-chair, Dr. Chad Sosolik. Without being able to use his ion beam systems I would quite literally have no data in this dissertation. Thankfully, whenever I needed Kinard's invaluable equipment, Dr. Sosolik was always there to help. I am also grateful for all of the guidance and wisdom that Dr. Sosolik provided over the years. I am also very thankful to the other committee members, Dr. Eric Johnson and Dr. Pingshan Wang, for their valuable input during my comprehensive exam which caused me to refocus my research.

Dr. Jim Harriss is another person who has helped me substantially during my time in graduate school. I am thankful for his help with sample preparation, EBIT operation, and equipment training. I appreciate that he always focused on my deep understanding of processes instead of just ensuring that I could follow an algorithm.

I also would like to thank Dr. Daniel Noneaker for his assistance during my transition to graduate school and for always showing a genuine interest in my progress. He is also responsible in part for encouraging me to apply for the GAANN fellowship, which I ultimately received. For that I am thankful to him and the U.S. department of education.

There are a multitude of fellow graduate students, primarily working with Drs. Harrell and Sosolik, who I am indebted to for all of the help that they provided me over the years. I greatly appreciate Radhey Shyam and Githin Alapatt helping to introduce me to the equipment and procedures for the physics and electronics characterization labs, respectively. I appreciate all of the help with sample irradiation in the EBIT that Daniel Field and Dhruva Kulkarni provided, and I am particularly grateful to Dhruva for always helping me to think of new ways to look at and analyze data. I am also thankful to Patrick Johnson and David McCall for their help with the Schottky diode experiments, and for being kind enough to wait for me to finish my experiments before remodeling the ion beam chamber. I appreciate all of my colleagues in Dr. Harrell's lab, Shiva Chinnam, Deep Shah, Gowtham Prithivi, and Eyob Tarekegn, who were very helpful with coordinating equipment usage in the lab and were always very pleasant to talk to when things were a little slower.

I am also thankful to Dr. Sung-O Kim, Jae Young Kim, and Do Yeob Kim for introducing me to research as an undergraduate student and helping me determine that graduate school was the right path for me.

I am extremely grateful to have such a wonderful family that was always supportive and encouraging during the lengthy course of my studies. I am particularly thankful to my parents for paying for my undergraduate education, because without that amazing gift I might not have felt comfortable pursuing graduate school. I am also very thankful to my mom and mother-in-law for their help watching my son so that I was able to accomplish more work in the last year and half of the program. And a special thank you to my son Lucas for kicking my butt into gear and getting me working harder to graduate in a timely manner.

Finally, I want to thank all of the students that I had the privilege to teach over the years. My time spent teaching helped reaffirm my decision to pursue a career in education, and the joy I got from teaching helped keep me motivated on the long trek towards completing my degree.

TABLE OF CONTENTS

	Page
TITLE PAGE	i
ABSTRACT	ii
ACKNOWLEDGMENTS	iv
LIST OF TABLES	x
LIST OF FIGURES	xi
CHAPTER	
1 INTRODUCTION	1
2 RADIATION DETECTION	4
2.1 Introduction	4
2.2 Charge Particulate Detectors – Principles and Examples	5
2.3 Solid State Detectors	7
2.4 Detecting Slow Ions	12
3 SLOW HIGHLY CHARGED IONS AND THE ELECTRON BEAM ION TRAP	14
3.1 Introduction	14
3.2 HCI Physics	15
3.3 EBIT Operating Principles	21
3.4 HCI Surface Interactions	26
4 EFFECTS OF SLOW HCI IRRADIATION ON MOS CAPACITORS	33
4.1 Introduction	33
4.2 Experimental Procedure	50
4.3 HCI Radiation Effects on C-V Characteristics – Qualitative	56
4.4 Data Analysis	64
4.5 Charge State Dependence of C-V Curve Changes – Quantitative	70

Table of Contents (Continued)

	Page
4.6 Summary and Conclusions	77
5 EFFECTS OF SLOW Na^+ IRRADIATION ON SCHOTTKY DIODES.....	79
5.1 Introduction.....	79
5.2 Experimental Procedure.....	97
5.3 Kine-Current	103
5.4 Radiation Tolerance.....	109
5.5 Summary and Conclusions	117
6 FUTURE WORK.....	119
6.1 MOS Capacitors.....	119
3.2 Schottky Diodes	124
3.3 Prototype Slow HCI Sensor	128
APPENDICES	133
A: Publications.....	134
B: Guides and MATLAB Code for Analysis with MOS Work.....	135
B.1 Procedure for Gaussian Analysis	135
B.2 Code for interpolating data points.....	137
B.3 Code for creating Gaussian fit and integrating across surface	140
C: MATLAB Code for Analysis with Schottky Diode Work	143
C.1 Code for plotting curves in various scenarios.....	143
C.2 Code for extracting diode parameters from I-V data	153
C.3 Code for extracting diode parameters from C-V data	156
C.4 Code for determining the peak reverse current magnitude and the voltage point at which compliance is reached	159
D: Miscellaneous Procedural Guides and Manuals	162
D.1 Guide for operating the Edwards thermal evaporator.....	162

Table of Contents (Continued)

	Page
D.2 Guide for performing high frequency C-V measurements with the HP 4280A.....	166
D.3 Guide for performing quasi static C-V measurements with the HP 4140B.....	171
D.4 Guide for performing manual C-V sweeps with the Agilent E4980A LCR meter	177
D.5 Basic operational guide for HP 4156B precision semiconductor parameter analyzer	179
D.6 Operation manual for the singly charged ion beamline in Kinard 13	181
D.7 Guide for performing 4-pt probe measurements.....	185
D.8 Guide for performing bias temperature stress (BTS) measurements.....	189
D.9 Guide for mounting Schottky diode on platen.....	191
REFERENCES	193

LIST OF TABLES

Table		Page
5.1	Ion range, standard deviation (straggle) for ion range, maximum electron energy, minimum number of electrons created per ion, and a rough approximation of electron range for the Na ⁺ beam energies used	104
5.2	Total ion dose for all diodes with both thick (~360 nm) and thin (~26 nm) Schottky contacts	110
5.3	Initial values, final values, and associated percent change for ideality factor and barrier height extracted from in-situ I-V curves for both thick (~360 nm) and thin (~26 nm) Schottky contact diodes	115

LIST OF FIGURES

Figure	Page
2.1	Depletion region in a PN junction diode which is devoid of mobile charge carriers. Also shown is the electric field inside of the diode structure (negative valued because it is pointing from right to left, in the negative x direction)10
3.1	Difference in energy deposition methods for ions impacting a solid target. Red lines indicate recoil trajectories and blue areas are due to electron induced electronic excitation.....17
3.2	Hollow atom formation and neutralization during interaction between a slow HCI and the target surface.....20
3.3	Schematic model of the EBIT alongside a photograph of the actual EBIT setup in Kinard Hall at Clemson University22
3.4	Representation of the key EBIT components which create and trap the HCIs25
3.5	Example of hillock (a) and crater (b) formation on surfaces from individual HCI impacts28
3.6	Transmission electron microscope (TEM) image of a very thin and uniform SiO ₂ layer deposited on Si with HCI assistance in an IBAD process.....31
4.1	Structure of metal oxide semiconductor (MOS) capacitor (layer sizes not to scale).....35
4.2	Band diagram of the MOS system illustrating the four basic modes: (a) accumulation, (b) flatband, (c) depletion, specifically the midgap point where the semiconductor is intrinsic at the oxide/semiconductor interface [$ q\phi_S = q\phi_B $], and (d) the onset of strong inversion [$ q\phi_S =2 q\phi_B $]. $q\phi_S$ is the total band bending and $q\phi_B$ is the Fermi level in the semiconductor bulk38
4.3	Capacitance voltage (C-V) curve for a p-type MOS capacitor displaying frequency dependence. Curve (a) illustrates low frequency/quasi static curve and curve (b) illustrates the high frequency curve.....46

List of Figures (Continued)

Figure	Page
4.4	Various types of charge imbalances that occur in MOS capacitors.....48
4.5	Si/SiO ₂ sample containing 25 MOS capacitors arranged in a 5x5 array52
4.6	Typical beam profile for Ar ^{Q+} irradiation (Q=8 is shown).....55
4.7	C-V curves for two different capacitors on separate samples. One sample was irradiated and the other one is pristine. Sample was irradiated with Ar ⁸⁺ to a fluence of 4.20x10 ¹³ ions/cm ² . The midgap shift and stretchout between midgap and inversion points are also shown60
4.8	HCI beam alignment with different sample structures (drawn to scale). Dashed circles filled with transparent pink color represents FWHM of HCI beam (3 mm diameter). Solid gray circles represent capacitors. (a) FWHM of HCI beam fully overlaps with single 3 mm diameter capacitor, (b) FWHM of HCI beam partially incident on four capacitors in array structure (1 mm diameter capacitors with 2.5 mm center-to-center spacing), and (c) FWHM of HCI beam fully incident on one capacitor in array structure.....65
4.9	Numerical representation of the stretchout between midgap and inversion in Volts for the 5x5 capacitor array shown in Fig. 4.1 (i.e. the V _{MG} - V _{INV} values for the 25 capacitors) with the 2D Gaussian fit overlaid (R ² = 0.9407). The stretchout values of the Gaussian fit range from approximately 0.5 V (dark blue) to a little above 14 V (dark red)68
4.10	Average V _{MG} - V _{INV} values for each of the nine irradiated samples. Sample averages were obtained by using the 2D Gaussian fit of the voltage data. The fluences in this plot have been adjusted from the nominal fluence using equation (4.18) from Section 4.4.3.....71
4.11	Average stretchout between midgap and inversion for all samples of a given charge state minus the corresponding stretchout seen in the pristine sample. Also shown is a power law fit showing that stretchout between midgap and inversion varies as Q ^{-1.7}73

List of Figures (Continued)

Figure	Page
4.12	Average V_{MG} values for each of the nine irradiated samples. Sample averages were obtained by using the 2D Gaussian fit of the voltage data. The fluences in this plot have been adjusted from the nominal fluence using equation (4.18) from Section 4.4.3.....75
4.13	Average midgap voltage for all samples of a given charge state minus the average midgap voltage seen in the pristine sample. Also shown is a power law fit showing that shifts of midgap voltage vary as $Q^{-1.8}$76
5.1	Simple Schottky diode structure (a) cross sectional view and (b) aerial view. (layer sizes not shown to scale).....82
5.2	Band diagram of (a) metal and semiconductor separated and (b) after coming together to form a Schottky diode.....86
5.3	Various conduction mechanisms in a Schottky diode: (1) thermionic emission, (2) tunneling, (3) recombination in the depletion region, (4) diffusion of electrons, and (5) diffusion of holes (recombination in the bulk).....90
5.4	Schottky-barrier lowering due to the image force between an electron in the semiconductor and a positive image charge in the metal. Also shown is the qualitative change in barrier height for forward and reverse biases94
5.5	Schottky diode mounted on stainless steel platen using Ag paint99
5.6	Process flow for irradiation of Schottky diodes. Red boxes indicate times when the ion beam is incident on the diode and green boxes indicate times when the ion beam is off. (617) and (2400) indicate measurements are taken with the Keithley 617 and Keithley 2400, respectively.....102
5.7	Percent differences between diode I-V sweeps with a 1.5 keV Na^+ beam incident on the diodes and with the Na^+ beam turned off for (a) a thin Schottky contact device and (b) a thick Schottky contact device107

List of Figures (Continued)

Figure	Page
5.8	In-situ I-V curves taken prior to 0.5 keV irradiation, after 10 minutes of irradiation, and after 90 minutes of irradiation for (a) a thin Schottky contact device and (b) a thick Schottky contact device112
5.9	In-situ I-V curves taken prior to 2.0 keV irradiation, after 10 minutes of irradiation, and after 90 minutes of irradiation for (a) a thin Schottky contact device and (b) a thick Schottky contact device113
6.1	Sputter yields from a silicon surface irradiated with 4 keV Xe ⁸⁺ at various incidence angles. It can be seen that the Si ⁺ sputtering was more dependent on the kinetic energy of the HCI, whereas the proton sputtering was dependent on the potential energy and independent of the kinetic energy123
6.2	(a) Pre and post irradiation forward I-V curves shown on a semi-log plot. (b) Pre and post irradiation reverse I-V curves. Changes in average barrier height (c) and ideality factor (d) of the Schottky diode. For parts (c) and (d) the <i>Day</i> axis can be understood as 0 = preirradiation, 1 = post irradiation; day of irradiation, 2 = day after irradiation, etc.127
6.3	Simple schematic for a prototype slow HCI sensing apparatus.....129

CHAPTER 1

INTRODUCTION

The detection and monitoring of radiation are important in several different application areas including space operations, nuclear energy production, and medicine [1-11]. At its core, radiation detection relies on understanding how the incident radiation interacts with the devices and device materials that are acting as the radiation detectors. Of particular interest is the detection of slow highly charged ions (HCIs), which naturally occur in certain space environments [12, 13] and in nuclear reactors [2, 5, 10]. Preliminary research has also suggested that slow HCIs could be useful in numerous applications ranging from nanofabrication to cancer therapy [11, 14-19]. Due to the relatively short time that slow HCIs have been producible in lab settings at a reasonable cost, the basic mechanisms of slow HCI interactions with electronic materials and electronic devices are still not fully understood. The distinguishing property of HCIs is that they carry a potential energy which is equivalent to the ionization energy required to create the HCI, and for the case of slow HCIs this potential energy is comparable to or even greater than the kinetic energy of the ions, which leads to fundamentally different interactions between the HCIs and materials as compared to singly charged ions. Therefore, the primary goal of this work is to gain a better understanding of how silicon-based devices respond to slow HCI irradiation with low kinetic energies (on the order of keV). Chapter 2 provides a more detailed background on the principles of radiation

detection, and explains several advantages that have led to the predominance of solid-state detectors based on silicon technology. Based on the operating principles of traditional solid-state radiation detectors, the need for new detector technology for sensing slow charged-particulate radiation is presented. A more detailed background on HCIs, how they are produced using an electron beam ion trap (EBIT), and some preliminary work showing how slow HCIs interact with materials is presented in Chapter 3.

Metal oxide semiconductor (MOS) capacitors were chosen to investigate the fundamental interactions of slow HCIs with devices due to their relatively simple structure, their sensitivity to charge imbalance in the device, and the ubiquity of the MOS structures in modern electronics. Oxidized silicon wafers were exposed to 1 keV ion beams of Ar^{4+} , Ar^{8+} , and Ar^{11+} created in the Clemson University EBIT, and after irradiation an array of metal contacts was deposited onto the oxidized silicon wafers to create MOS capacitors. The first subsection in Chapter 4 provides background on the basic structure and operation of MOS capacitors as well as a description of the capacitance-voltage (C-V) measurement techniques that were employed to track changes in the MOS capacitors after exposure to slow HCIs. The remaining subsections in Chapter 4 describe in detail the experimental procedure and the observed results.

The relatively unexplored nature of the interaction of slow HCIs with electronic devices and materials makes it an exciting and interesting research topic; however, it is important to also consider the detection of slow singly charged ions. Although the detection of slow singly charged ions is important in and of itself, experiments aimed at

understanding how these ions interact with materials and devices can serve as a baseline for similar experiments with slow HCIs by isolating the effects due to the kinetic energy of the ions. In order to investigate the interaction mechanisms of slow singly charged ions with electronic devices, Schottky diodes with thin (~26 nm) and thick (~360 nm) Schottky contacts were exposed to Na^+ beams with kinetic energies between 0.5 keV and 2.0 keV. The primary goal of these experiments was to detect a current arising from the hot electrons generated in the Schottky contact by the incident ions. This kine-current is analogous to chemi-currents which have been reported to result from hot-electrons created by chemical reactions at the rectifying contacts of Schottky diodes [20-23]. The basics of Schottky diode operation and structure are presented in the first subsection of Chapter 5, and the remaining subsections of Chapter 5 describe the experimental procedure and results.

Any good research project, particularly one that is foundational such as the work described in this dissertation, typically results in more questions than answers. As such, Chapter 6 details future work with both MOS capacitors and Schottky diodes that should be carried out in order to obtain a better understanding of the fundamental interaction mechanisms between slow ions and electronic devices. A basic prototype for a slow HCI detector is also proposed, but there is still much work to be done before such a sensor can be realized.

CHAPTER 2

RADIATION DETECTION

2.1 INTRODUCTION

Radiation detectors have a myriad of applications in a variety of diverse fields including medical imaging, personal safety, space exploration, and high energy physics. In general, radiation sources can be grouped into two broad categories; charged particulate radiation and uncharged radiation. The former consists of protons, electrons, alpha particles, and heavy ions, whereas the latter consists of neutrons, gamma rays, and x-rays. The remaining chapters of this dissertation are concerned with charged particulate radiation, particularly heavy ions; therefore, the following discussion will focus primarily on the considerations associated with detecting such radiation. For the interested reader, references [24-27] contain a much more detailed description of radiation detectors and the associated physics. In Section 2.2 we introduce the basic principles of detecting charged particulate radiation as well as some of the early types of detectors. In Section 2.3 we discuss detectors based on semiconductor materials and devices, and the need for new detection technology for slow highly charged ions is discussed in Section 2.4.

2.2 CHARGE PARTICULATE DETECTORS – PRINCIPLES AND EXAMPLES

The core principle behind radiation detectors, regardless of the type of radiation to be detected, is how the incident radiation interacts with the material of the detector. Once the interaction mechanisms are understood, a scheme can be developed for quantizing the amount and/or energy of the incident radiation. In general, charged particles which are incident on any matter will lose energy at a gradual rate, primarily through inelastic (electronic interactions) and elastic (nuclear interactions) transfer of energy to the target material. This transfer of energy from the incident radiation to the target material is known as stopping power and is given by:

$$-\frac{dE}{dx} = S_{Total} = S_n + S_e \quad (2.1)$$

where E is energy, x is distance traveled by the radiation into the target material, S_{Total} is the total stopping power, S_n is the portion of the stopping power due to nuclear interactions, and S_e is the portion of the stopping power due to electronic interactions. The negative sign in equation (2.1) indicates the energy is being transferred to the target material from the incident radiation. A detailed expression for stopping power was first derived by Bohr, and then later expanded upon by Bethe and Bloch using quantum mechanics [25, 26]. The result is known as the Bethe-Bloch formula for stopping power and is given by:

$$-\frac{dE}{dx} = \frac{4\pi N_A r_e^2 m_e c^2 \rho Z Q^2}{A \beta^2} \left[\ln \left(\frac{W_{max}}{I} \right) - \beta^2 - \frac{\delta}{2} - \frac{C}{2} \right] \quad (2.2)$$

where N_A is Avogadro's number, r_e is the classical radius of the electron, m_e is the rest mass of the electron, c is the speed of light in vacuum, ρ is the density of the target medium, Z is the atomic number of the target material, Q is the charge state of the ion, which is an integer value equal to the number of electrons removed to create the ion, A is the mass number of the target material, β is a correction factor, W_{max} is the maximum energy transferred in a single collision, I is the ionization potential of the target material, δ is a density correction factor, and C is a shell correction factor. From equation (2.2) it can be seen that the stopping power is dependent on properties of both the detector material and the incident radiation, as would be expected.

For most practical applications, only the portion of the stopping power related to the electronic interactions is considered when developing detectors. This is reasonable because the nuclear stopping power only begins to dominate towards the end of the charged particle's path in the material [28]; and furthermore, for typical radiation sources with high kinetic energies, the portion of the path where nuclear stopping dominates is negligible. The electronic stopping of radiation in matter results in ionization of the target atoms or excitation of the target electrons depending on the intrinsic properties of the target material and the energy of the incident radiation. Gas-filled detectors such as ion chambers, proportional counters, and Geiger tubes are some of the earliest radiation detecting devices which operate by collecting ions and free electrons that are created as the incident radiation passes through a gas. The same basic principle of collecting the charged particles in the target material after the incidence of ionizing radiation has also been applied to liquid filled detectors [26]. The operation of scintillation detectors is

slightly different in that the target atoms are not ionized, but rather the electrons are excited while still being bound to the atoms. In order for the electrons to only be excited and to avoid ionization, scintillation detectors are typically constructed from materials with higher ionization energies such as oxides. As the electrons return to the ground state, photons are emitted that can then be collected and converted into an electrical signal by light detection equipment such as photomultiplier tubes or photodiodes. Understanding these basic radiation detection principles and detector structures is important, but as will be discussed in Section 2.4, these traditional techniques are not suitable for the detection of ions with kinetic energy on the order of 1 keV or lower.

2.3 SOLID STATE DETECTORS

Although there are still application areas where gas-filled detectors and scintillation detectors excel, in most applications using a solid-state semiconductor detector is preferable. Some of the advantages offered by solid-state detectors are [25, 27]:

- i. Small ionization energy compared to gas-filled and scintillation detectors (~ 3 eV in common semiconductors, ~ 30 eV in gas-filled detectors, and ~ 100 eV for scintillation detectors)
- ii. High atomic density which allows for smaller size detectors
- iii. High charge carrier mobility which leads to fast charge collection times
- iv. Excellent mechanical rigidity which allows for self-supporting structures
- v. Ability to change field configurations in the device via doping

- vi. Mature processing techniques for materials due to extensive use of semiconductors in the electronics industry

Advantages (i.) and (ii.) also indicate that more charge carriers will be produced per incident quanta of radiation, which means solid-state detectors have a greater energy resolution compared to gas-filled and scintillation detectors. They also have greater spatial resolution when used as position sensitive detectors. The high charge carrier mobility also means that solid-state detectors are better suited to radiation environments with higher fluence (i.e. more radiation arriving per unit time), because the effects of each quanta of radiation can be collected at a much faster rate. Detectors based on n-type silicon are the most common [25, 26] due to the mature industry surrounding the production of silicon-based electronics. Silicon crystals with $\langle 111 \rangle$ orientation are probably most widely used because they allow for minimal nuclear stopping of the incident radiation in the detector for the case of charged particulate radiation. Another advantage of using silicon based detectors is the potential to easily incorporate them into the same circuits as other electronic devices on a silicon wafer.

The semiconductor device that is most commonly used for radiation detection is the rectifying junction of a diode. Both PN junction diodes and Schottky diodes, referred to as surface barrier detectors, are commonly used as radiation detectors. During the formation of the diode junction, a space charge region (also called the depletion region) is created immediately on either side of the junction in a PN diode, and only in the semiconductor region of a Schottky diode. All of the mobile charge carriers have been removed from this depletion region, and the remaining fixed charge due to the ionized

dopant atoms in the semiconductor lattice lead to an electric field in the depletion region. The depletion region for a PN junction and the associated electric field are shown in Figure 2.1. As the radiation moves through the depletion region, ionization will occur, creating electron-hole pairs which will be swept out of the depletion region by the electric field and eventually collected at the electrodes. Only those electron-hole pairs that are created in the depletion region are able to contribute to the output signal, because electron-hole pairs in other areas of the device quickly recombine. It is also possible for some of the electrons and holes created by the radiation to recombine or become trapped by impurities in the semiconductor lattice in the depletion region before being collected. In order to minimize these detrimental effects that can lead to non-linearity in detector response, it is of the utmost importance that the initial semiconductor be as pure and free of defects as possible.

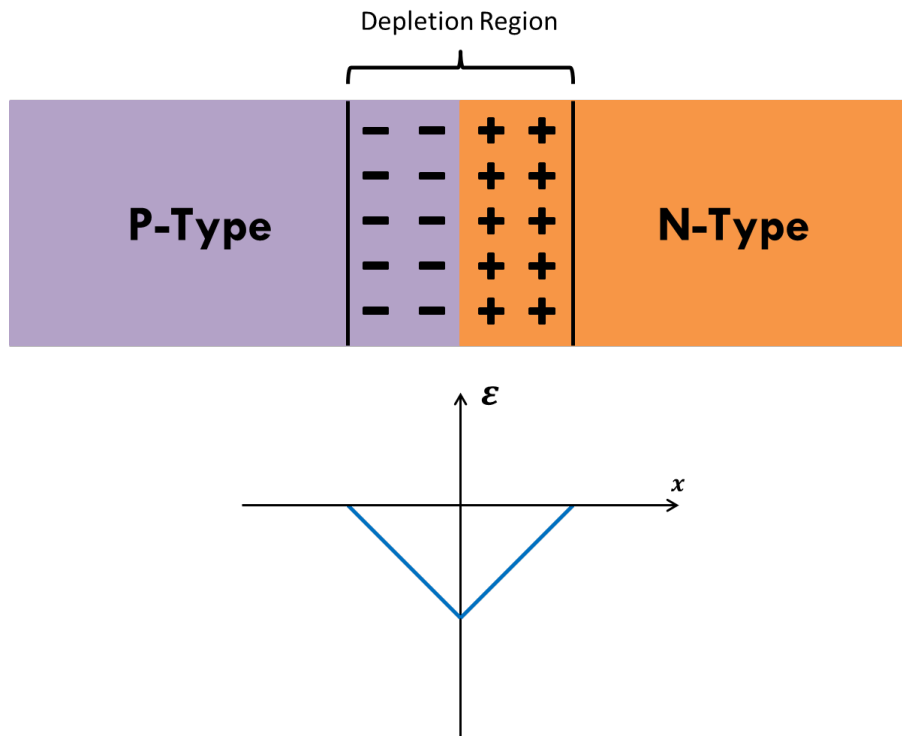


Figure 2.1: Depletion region in a PN junction diode which is devoid of mobile charge carriers. Also shown is the electric field inside of the diode structure (negative valued because it is pointing from right to left, in the negative x direction)

It is possible to operate diode detectors at zero applied bias in order to improve the signal to noise ratio due to the lack of any leakage current. The main downside of doing this is that the active volume for detecting radiation, the depletion region, is relatively small. Therefore, it is almost always the case that diode detectors are operated in reverse bias. Not only does this increase the size of the depletion region, but it also reduces the system capacitance which in turn reduces the system noise. The size of the depletion region can be increased by increasing the reverse bias voltage, but care must be taken to avoid breakdown voltages that will cause irreparable damage to the device. With appropriate selection of device geometry, doping, and operation bias, detectors can be constructed to operate in a fully depleted mode such that the depletion region extends through almost the entire width of the semiconductor wafer. A compensated, intrinsic region can also be created between the p-type and n-type regions of a PN junction diode to create a PIN diode which has a larger depletion region (effectively the entire intrinsic region).

It is important to also consider the depth into the diode detector that the incident radiation must travel before it reaches the depletion region. Any part of the detector that the radiation must travel through while not contributing to the output signal is known as an entrance window or dead layer. Ideally the dead layer should be kept as small as possible in order to maintain accurate detection. For surface barrier detectors this can be accomplished by having a Schottky contact that is a very thin layer of metal (on the order of tens of nanometers). For PN junction detectors a thin dead layer is achieved by highly

doping a narrow region on the surface such that a p^+-n or n^+-p junction is formed and the depletion region is almost entirely in the lower doped region.

The main drawback of solid-state detectors is their relative susceptibility to radiation damage over time. The deleterious effects primarily arise from the displacement of atoms from their lattice sites which create point defects or defect clusters depending on the type of incident radiation. This type of damage is primarily due to the nuclear stopping which occurs near the end of the radiation particle's path in the detector. The overall results of these defects are charge traps which create easier paths for recombination and also lead to non-linearity in detector response. The defects will also cause an increase in the reverse leakage current which decreases the signal to noise ratio of the detector. Fortunately, these effects can be countered by operating the detectors at lower temperatures and higher reverse biases. Depending on the specific types of defects introduced by radiation, annealing can also be a useful technique for restoring the detector quality.

2.4 DETECTING SLOW IONS

Slow ions with low kinetic energy (on the order of 1 keV or lower), present a challenge when attempting to detect them with the traditional solid-state detectors described in the previous section. The primary difficulty associated with using traditional solid-state detectors for slow ions is that the penetration depth is often much smaller than the dead layer, meaning that the slow ions would not even reach the depletion region in many cases. The Bethe-Bloch model for stopping power also begins to break down as the

ions speed become comparable to or lower than the velocity of electrons in the Bohr model [27]. The slow velocity of the ions also means that the nuclear stopping will dominate over the electronic stopping, which is in opposition to the examples discussed previously [29].

How to detect slow highly charged ions (HCIs) is an interesting subset of the challenge of slow ion detection. This research area is particularly interesting because there is very little published work relating to the interaction of slow HCIs with surfaces and electronic devices. Not only is the electronic stopping no longer the dominant stopping mechanism, but there are also several charge exchange processes that occur as the HCI interacts with the target material that need to be considered. Further details regarding the physics of slow HCIs and how they interact with materials is presented in the next chapter.

Whether it be slow HCIs or slow singly charged ions, the main focus of this work is not to design a suitable detector structure, but rather the goal is to better understand and characterize the effects that result from the interaction of these slow ions with electronic materials and devices. This understanding will form the basis for the future design and creation of suitable slow ion detectors.

CHAPTER 3

SLOW HIGHLY CHARGED IONS AND THE ELECTRON BEAM ION TRAP

3.1 INTRODUCTION

Slow highly charged ions (HCIs) have been incorporated into our experiments primarily due to the fact that it is a relatively unexplored type of radiation. Our goal is to provide a deeper fundamental understanding of how slow HCIs interact with electronic materials and devices with the end goal of advancing slow HCI sensing technology. There are two application areas where we envision this sensing technology will be most relevant; however, the fundamental understanding can be instrumental to a variety of application areas.

Because the universe consists primarily of highly ionized matter [11], space applications is one area where HCI sensing is of the utmost importance. Perhaps the most practical example is accurately monitoring the HCI component of the solar wind in order to avoid costly issues with telecommunications satellites in low earth orbit [30-35]. More generally, HCI sensors could be used for exploratory diagnostics as we expand our knowledge of the universe. Nuclear fusion generators are another application area where HCI sensing is relevant [11, 18, 36, 37]. Obviously having a reliable way to monitor the conditions inside a nuclear reactor is critical to safe operation.

The purpose of this chapter is to provide background information on HCIs so that the relevance of the results in the following chapter can be more easily understood. Section 3.2 describes basic HCI physics as well as some of the common models used to

characterize how slow HCIs interact with surfaces. The electron beam ion trap (EBIT), which is the device used to create our slow HCIs, is discussed in Section 3.3. Section 3.4 presents some results of HCI surface interaction from the literature, and describes several possible application areas for HCIs that are being pursued.

3.2 HCI PHYSICS

The primary feature that distinguishes HCIs from singly charged ions is the much larger potential energy due to charge states $Q \gg 1$. There is no hard definition for a Q value that must be reached in order for an ion to be considered highly charged, but conventionally the ion should at least have a charge state of 3^+ or 4^+ to be considered highly charged. By definition slow HCIs have velocity less than the Bohr velocity ($v_{\text{bohr}} = 2.19 \times 10^6$ m/s), which is the velocity of a ground state electron in the Bohr model. Because the nuclear motion of the system is much slower than the electron speed the nuclear stopping will dominate over electronic stopping when the slow HCIs interact with surfaces [38]. The potential energy of an HCI is equal to the sum of the binding energies of the electrons that are removed to create the HCI. The potential energy associated with slow HCIs is comparable to or even greater than the kinetic energy; therefore, it is the potential energy deposition that typically dominates for slow HCI-surface interactions. This is opposed to singly charged ions where energy deposition is almost entirely due to the ion's kinetic energy. This difference between potential energy dominating for slow HCIs and kinetic energy dominating for singly charged ions means that the two types of

radiation will interact with target surfaces in fundamentally different ways. A visual representation of this difference is shown in Figure 3.1 [39].

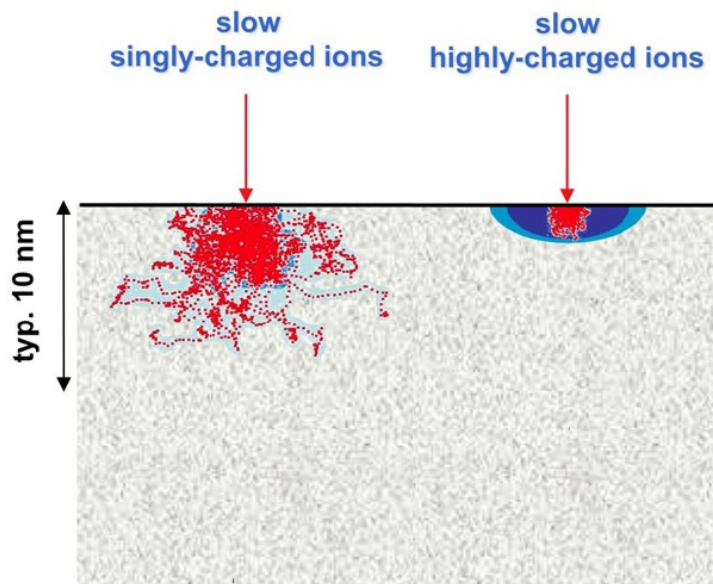


Figure 3.1: Difference in energy deposition methods for ions impacting a solid target. Red lines indicate recoil trajectories and blue areas are due to electron induced electronic excitation. Adapted from [39].

Although slow HCI radiation is not nearly as well understood as singly charged ion radiation, there are still several models which can adequately describe the interaction process between slow HCIs and surfaces. The classical over-the-barrier model was first observed and described in the 1990s [40, 41]. As the HCI approaches the surface it creates an image charge in the target which accelerates the HCIs towards the surface and sets a lower limit for the impact velocity. When the HCI is at some critical distance from the surface, R_C , the neutralization process will begin when electrons from the target go over the barrier between the potential wells of the target material and the HCI. The neutralization process can begin several dozen atomic diameters away from the surface [11]. The critical distance in atomic units is given by [40, 42]:

$$R_C \approx \frac{\sqrt{2Q}}{\phi} \quad (3.1)$$

where Q is the charge state and ϕ is the material work function. The first electrons that are captured by the HCI from the surface do not go to the ground state configuration, but rather they are captured in high lying Rydberg orbitals. This forms the so called “hollow atom” structure as shown in Figure 3.2. Because this “hollow atom” structure is clearly unstable, there are several interactions which occur after the initial start of neutralization: electrons can be emitted into the vacuum, electrons from the HCI can be recaptured by the surface, electrons in the HCI can undergo standard radiative decay by which x-rays are emitted, and Auger de-excitation with multiple electrons can occur. As the HCI comes into close contact with the surface, the outer layer of electrons is peeled off and a smaller hollow atom is created inside the target [38, 43]. The entire interaction process takes place in only a matter of femtoseconds within a nanometer sized region in the

topmost layer of the target [11, 38, 14, 44, 45]. Because a vast majority of the HCI's potential energy [38] is deposited in such a small region, there is an immense amount of power density being transferred to the surface which reaches as high as 10^{14} W/cm² [44, 45]. Such a large power density causes hundreds of secondary electrons and sputtered particles to be detected for each HCI impact [46]. This large yield of secondary electrons and sputtered particles can be explained by the Coulomb explosion model for insulating and semiconducting materials [38, 39]. The basic premise of this model is that the target material is not able to replenish the electrons that are lost to the HCI before the ionized target atoms begin to repel one another. Once the force becomes great enough, there is an "explosion" which sends a shock wave through the target material and results in atoms being sputtered from the surface. The large yield of sputtered particles leads to each HCI creating a nano-sized structure on the surface with essentially 100% probability [18]. Different types of surface structures such as craters, hillocks, and calderas, have been observed in separate studies with different beam parameters and target materials [29, 39, 47-49].

It is clear that the unique properties of slow HCIs lead to a completely different mechanism of interaction with target materials as compared with singly charged ion radiation. A better understanding of exactly how slow HCIs interact with electronic materials and devices is a crucial step in developing sensing technology that is able to accurately measure naturally occurring slow HCI radiation.

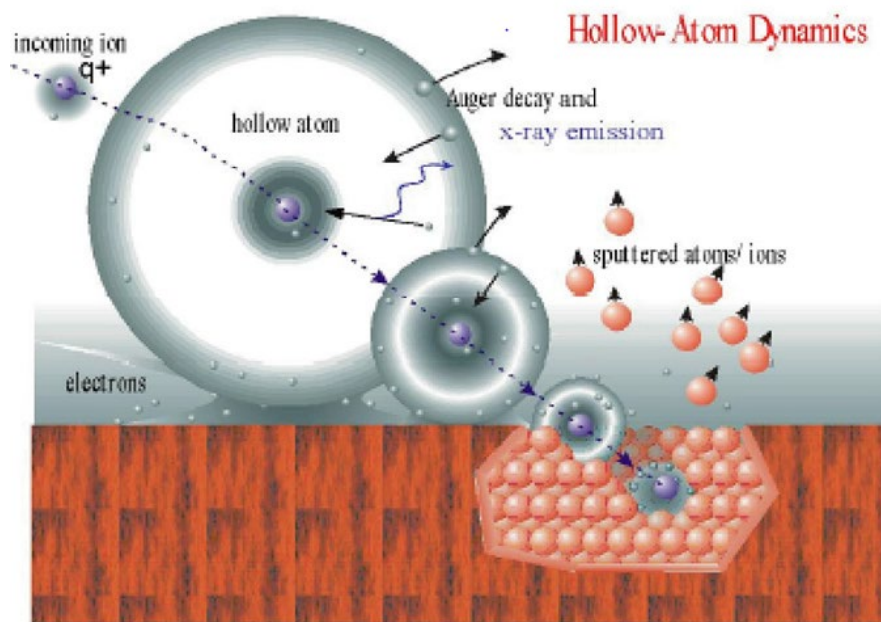


Figure 3.2: Hollow atom formation and neutralization during interaction between a slow HCl and the target surface. Taken from [29].

3.3 EBIT OPERATING PRINCIPLES

The first EBIT was constructed in 1986 at the University of California Lawrence Livermore National Laboratory [50], and since then several EBITs have been constructed in various locations around the world including Tokyo, Dresden, and of course Clemson. Initially EBITs were very costly to operate due to the cryogenic cooling that was required to operate the superconducting magnets; however, new technology was developed that only requires water cooling. This significantly decreased operating costs of EBITs thereby making them more accessible [46]. In Figure 3.3 we show that the EBIT is relatively compact, making it an attractive alternative to large linear accelerator facilities. Compared to linear accelerators and electron cyclotron resonance (ECR) sources, EBITs are also unique in that they are able to produce HCIs with relatively low kinetic energy (at or below keV range).

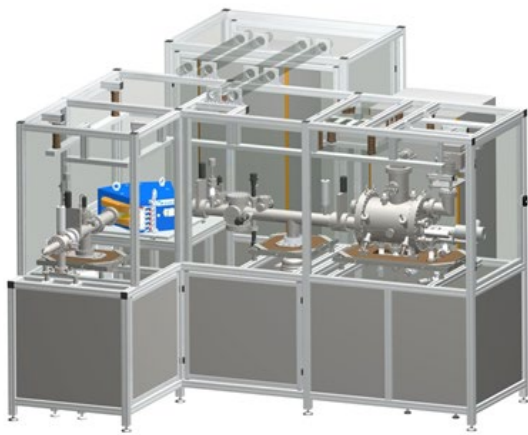


Figure 3.3: Schematic model of the EBIT alongside a photograph of the actual EBIT setup in Kinard Hall at Clemson University (photo credit: Dr. Jim Harriss).

In Figure 3.4 we illustrate several crucial components of the EBIT, and this will serve as a useful reference for understanding the basic principles of operation [15, 46, 51]. A high energy electron beam is aimed through the chamber containing atoms of the desired species, and the atoms become ionized to successively higher charge states via impact ionization with the electrons. This process obviously relates to the ‘*EB*’ in EBIT. After the contents of the chamber are ionized there are two challenges that must be addressed. First, care must be taken to minimize the probability of ions capturing electrons from the electron beam and ions exchanging charge with residual background species in the chamber. High electron beam energy and high vacuum are necessary in order to mitigate these two undesirable effects which serve to lower the ion charge state [36]. The second challenge that needs to be addressed is how to spatially trap the ions until they can be extracted (the ‘*IT*’ in EBIT). The ions are trapped radially by the same electron beam that ionized them. Superconducting magnets further increase the electron beam density which increases the effectiveness of the electron beam to radially trap the ions. Three drift tube segments, with polarities as shown in Figure 3.4, serve to trap the ions axially by creating a potential well centered on the middle drift tube. Ions can be extracted by operating the EBIT in one of two different modes: leaky mode, or pulse mode [52]. In both modes the ions are extracted by lowering the potential on the drift tube farthest from the electron gun. In leaky mode the potential is fixed at a level somewhere between the potentials of the other two drift tubes so that there is a continuous stream of HCIs. In pulse mode the potential is lowered periodically (typical pulse frequencies vary from a few milliseconds to several seconds) to produce bursts of

HCI. On the far end of the chamber the electrons are collected, and the extracted ions are passed through several optical systems which configure the ion beam. The desired charge state is then selected by an analyzing magnet. The ions from the drift tube enter the analyzing magnet perpendicular to the magnetic field which creates a force on the ions such that they travel along a path with radius of curvature given by,

$$r_c = \frac{mv}{QB} \quad (3.2)$$

where m is the ion mass, v is the ion velocity, Q is the ion charge state, and B is the strength of the magnetic field. All ions have approximately the same velocity, therefore the magnetic field strength can be tuned until ions with the desired mass to charge ratio are passed through the 90 degree turn. Ions with undesired mass to charge ratios will either turn too sharply or not sharply enough and impact the chamber walls. Because the ion beam consists of species with different masses and different charge states, it is important to consider degenerate charge states where different ion species with different charge states will have the same mass to charge ratio (e.g. C^{6+} and O^{8+}). Magnetic field settings that pass degenerate charge states should be avoided. Finally, there is a deceleration lens in front of the target chamber which reduces the kinetic energy of the ion beam prior to impacting whatever sample has been placed in its path [53]. The deceleration lens is important because it allows us to more nearly match the energy of our ion beam to the energy of ions seen in the solar wind and in nuclear reactors.

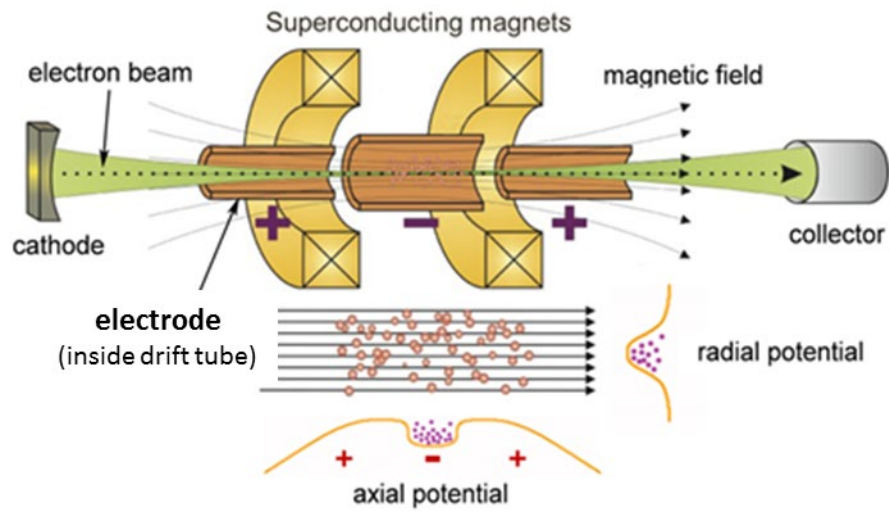


Figure 3.4: Representation of the key EBIT components which create and trap the HCIs.

3.4 HCI SURFACE INTERACTIONS

There is very little published work concerning HCI irradiation of electronic devices in the literature, but there are numerous studies that investigate the effects of slow HCI irradiation on various materials. Several semiconducting materials have been tested over the years including more common semiconductors such as Si [47, 54-59] and GaAs [60], as well as wide band gap materials SiC [61] and GaN [62, 63]. The standard insulating material in electronics, SiO₂, has also been exposed to HCIs [64]. Other dielectric materials which are more suitable for high-k dielectric devices, SrTiO₃ [65] and TiO₂ [66], have also been studied. Another material that is relevant to electronics processing which has been investigated is the common resist material poly(methyl methacrylate) (PMMA) [48]. These studies indicate that a good start has been made in characterizing HCI interactions with materials, but there is still a significant amount of work to be done, particularly in regards to slow HCI interactions with electronic devices. Further investigation into this area is important because understanding the specifics of slow HCI interactions with electronic devices is fundamental to creating slow HCI sensors, avoiding detrimental radiation effects, and realizing the full potential for nano-processing.

When slow HCIs are directed onto most target materials the result is nanometer scale defect sites, typically either craters or hillocks, which can be detected via atomic force microscopy (AFM) and scanning tunneling microscopy (STM). In Figure 3.5 we show two examples of different nano-structures that have been observed after slow HCI irradiation. Figure 3.5 (a) illustrates hillocks created on a CaF₂ target irradiated with

Xe^{33+} at 64 keV of kinetic energy, and Figure 3.5 (b) shows crater formation in a BaF_2 target irradiated with Xe^{28+} at 126 keV kinetic energy [39]. The green line in the left part of Figure 3.5 (b) indicates the line path used to produce the depth chart shown on the right of Figure 3.5(b). In Figure 3.5 the surface structures were detected by AFM operating in contact mode, but for Figure 3.5(b) the sample underwent chemical etching after HCI irradiation in order to expose the nano-pits. For both the CaF_2 and BaF_2 targets the number of nano-structures was found to correspond to the number of ions incident on the target surface, indicating that each HCI is responsible for creating a nano-structure. It has also been observed that hillocks and craters are not formed when the potential energy of the HCI is below some threshold value which is dependent on the target material. Above this threshold value the volume of the nano-structures is reported to increase with increasing HCI potential energy, while remaining relatively independent of HCI kinetic energy. This precision on such a small scale has caused several groups to promote the use of slow HCIs for single ion implantation (SII) for broader applications such as quantum computing [11].

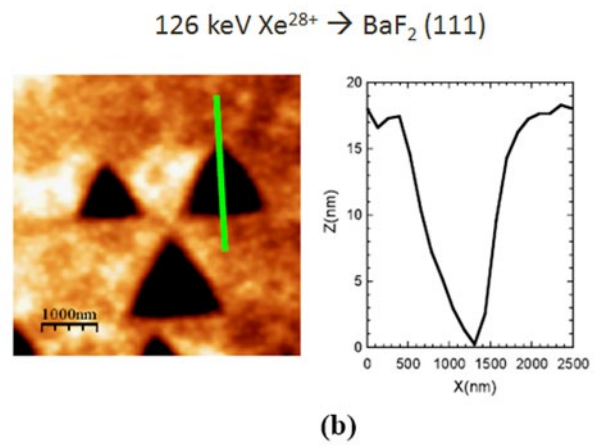
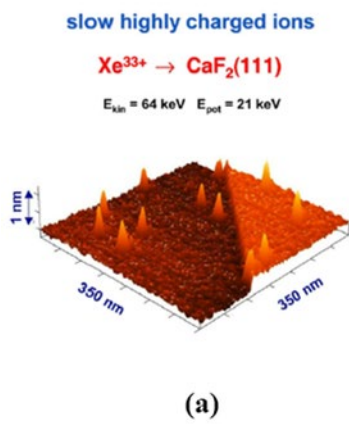


Figure 3.5: Example of hillock (a) and crater (b) formation on surfaces from individual HCI impacts. Adapted from [39].

Several studies have also investigated the ability of slow HCIs to remove various adsorbents from silicon surfaces by using time-of-flight (TOF) detection systems [54-57, 67-69, 70, 71]. By varying the incident angle of the slow HCIs on the target, it was determined that the adsorbent (H, H₂O, alkyl monolayers, etc.) was primarily removed by the potential energy of the slow HCI, whereas the sputtered substrate atoms were removed by the kinetic energy of the slow HCI. In most scenarios slow HCIs would be preferable for removing undesirable adsorbents because unlike singly charged ions they do not cause nearly as much damage to the underlying substrate. This is particularly true if the HCIs are incident at a grazing angle such that the kinetic energy of the ion does not have as much of an effect as it would at normal incidence. This behavior means that HCIs could be very useful in surface cleaning applications. A similar application which has also been proposed is a slow HCI based tool that performs precise secondary-ion mass spectroscopy (SIMS) measurements to determine material composition [38].

Slow HCIs have also successfully been used for ion beam assisted deposition (IBAD) of oxide layers [29, 72]. Slow HCI irradiation of H-passivated silicon in very high vacuum results in the sputtering of hydrogen with limited to no damage to the underlying bulk silicon. The resulting dangling bonds will remain open until oxygen gas is introduced into the chamber, at which point a thin oxide layer is formed on the surface. With this process there is significant control over the spatial distribution of the oxide because each slow HCI only affects a nanometer scale region. For low HCI doses the result would be isolated nano-dots of SiO₂, but sufficiently high HCI doses would allow for the removal of all of the surface hydrogen which would in turn enable the formation

of a thin oxide layer across the sample. In Figure 3.6 we show the very thin (9 Å) SiO₂ layer that was deposited on Si with the help of HClIs. Based on their characterization, the film showed high density, good adherence and improved optical and mechanical properties.

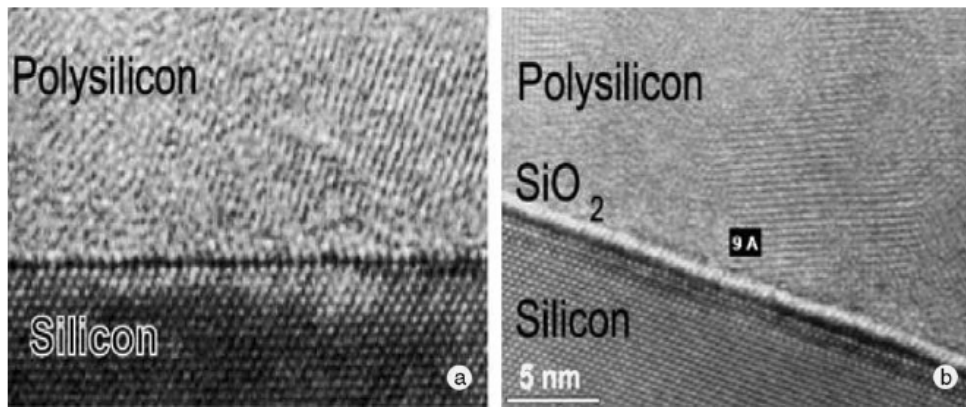


Figure 3.6: Transmission electron microscope (TEM) image of a very thin and uniform SiO₂ layer deposited on Si with HCl assistance in an IBAD process. Adapted from [72].

Slow HCIs have the potential to perform many of the steps in traditional semiconductor processing and electronic device fabrication [11, 18]. As has been shown, slow HCIs are able to efficiently clean semiconductor surfaces, and introduce nanometer sized structures with minimal or no damage to the underlying bulk. This is due to the fact that the energy transfer from the HCIs to the target material is predominantly due to the potential energy of the HCI. As electronic devices structures continue to scale down towards atomic sizes, slow HCIs could prove to be useful in implementing single ion implantation and depositing high quality thin films. HCIs have also been investigated as a potential candidate for creating the radiation used in extreme-ultraviolet (EUV) lithography [18], a subset of photolithography that is being pursued for next generation electronics. Based on all of these considerations it should come as no surprise that slow HCIs have been proposed as an integral part of nanofabrication tools by several groups [14-17]. Clearly, there are several interesting avenues of research to pursue with slow HCIs apart from the goal of developing sensing technology.

In the following chapter we discuss the possibility of utilizing MOS capacitors as the basis for sensing slow HCI radiation. The aim is to characterize the effects that various HCI beams have on MOS structures in order to gain an understanding of the physical mechanisms that can be used to detect the presence of slow HCIs.

CHAPTER 4

EFFECTS OF SLOW HCI IRRADIATION ON MOS CAPACITORS

4.1 INTRODUCTION

Metal oxide semiconductor (MOS) capacitors have been investigated as potential sensing devices for highly charged ions (HCIs) for several reasons. Perhaps the most important motivation for using MOS devices as sensors is that they are intrinsically sensitive to radiation since charge imbalances caused by the introduction of trapped charge in the oxide, interface traps, and bulk oxide traps lead to changes in device characteristics [73]. A second important factor is that MOS technology permeates nearly all aspects of modern electronics which would make MOS based HCI sensors relatively easy to integrate with most existing systems. The simplicity of the MOS structure and the relative ease of fabrication are also beneficial considering that these experiments are aimed at understanding the fundamental interactions between HCIs and electronic devices. The ultimate goal of this work is to use the observed changes in the electrical characterization of the MOS capacitors to quantify the damage done by a particular type of HCI irradiation. Once it is better understood how the MOS capacitors are affected by the HCI irradiation then work can begin to create HCI sensors. The remainder of Section 4.1 provides the theoretical background related to MOS capacitors, including the non-ideal effects arising from charge trapped in the system. Section 4.2 provides the details our experimental work. Section 4.3 contains a qualitative analysis of the changes observed in our samples, and discusses possible mechanisms that lead to these changes.

Section 4.4 describes our Gaussian analysis technique, and Section 4.5 presents the results of applying this analysis technique to our data. A brief summary and conclusion is given in Section 4.6.

4.1.1 MOS Structure and Operation

As can be seen in Figure 4.1 the structure of the MOS capacitor is relatively simple. The capacitor consists of a semiconductor substrate with an oxide layer and metal contact on top which is often referred to as the gate. There is also an Ohmic metal contact on the back side of the semiconductor substrate to allow for external electrical connections. Depending on the type of dopant used the semiconductor substrate with either be p-type or n-type. The following discussion relates only to p-type semiconductors which have been doped with acceptor impurities such as Boron; however, there are obviously analogous explanations for n-type semiconductor capacitors. Only the ideal MOS capacitor structure will be considered initially, but the effects of various oxide charges and interface states will be considered once the basics have been established.

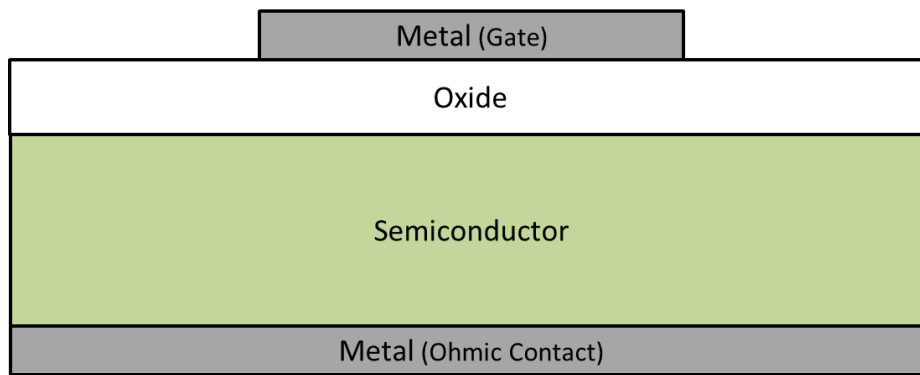


Figure 4.1: Structure of metal oxide semiconductor (MOS) capacitor (layer sizes not to scale).

Band diagrams such as those shown in Figure 4.2 are very helpful in understanding the operation of MOS capacitors. From left to right the band diagrams show information regarding the distribution and probability of occupancy of electrons for the metal, the oxide, and the semiconductor. E_{Fm} is the Fermi level of the metal and indicates the energy level at which there is a 50% probability of finding an electron in the metal. E_C and E_V are the energies at the bottom of the conduction band and the top of the valence band respectively, and the distance between the two energy levels is the semiconductor bandgap, E_G , which is full of forbidden electron states. E_i is the intrinsic level and is approximately in the middle of the semiconductor bandgap. E_F is the Fermi level in the semiconductor and has the same meaning as that for the Fermi level in the metal. Without doping $E_F = E_i$ in the semiconductor. For the band diagrams shown in Figure 4.2 E_F is closer to E_V in the semiconductor bulk (far right) indicating that there are less electrons in the conduction band than in the un-doped case, or conversely that there are more holes in the valence band. Both statements indicate the material is a p-type semiconductor. The bulk potential of the semiconductor, $q\Phi_B$, is the difference between the intrinsic level and the Fermi level in the bulk of the semiconductor (i.e. not at the oxide/semiconductor interface). The bulk potential can be calculated from the intrinsic carrier concentration of the semiconductor, n_i , and the concentration of the acceptor dopants, N_A , as shown in equation (4.1):

$$q\phi_B = kT \ln \left(\frac{N_A}{n_i} \right) \quad (4.1)$$

Where k is the Boltzmann constant, T is the temperature in Kelvin, and q is the elementary charge. As the bias on the topside metal contact changes the bands of the

semiconductor will bend either up or down at the oxide/semiconductor interface depending on the polarity of the applied bias. The amount of band bending in the semiconductor bandgap at the oxide/semiconductor interface relative to the semiconductor bulk is represented by $q\Phi_s$.

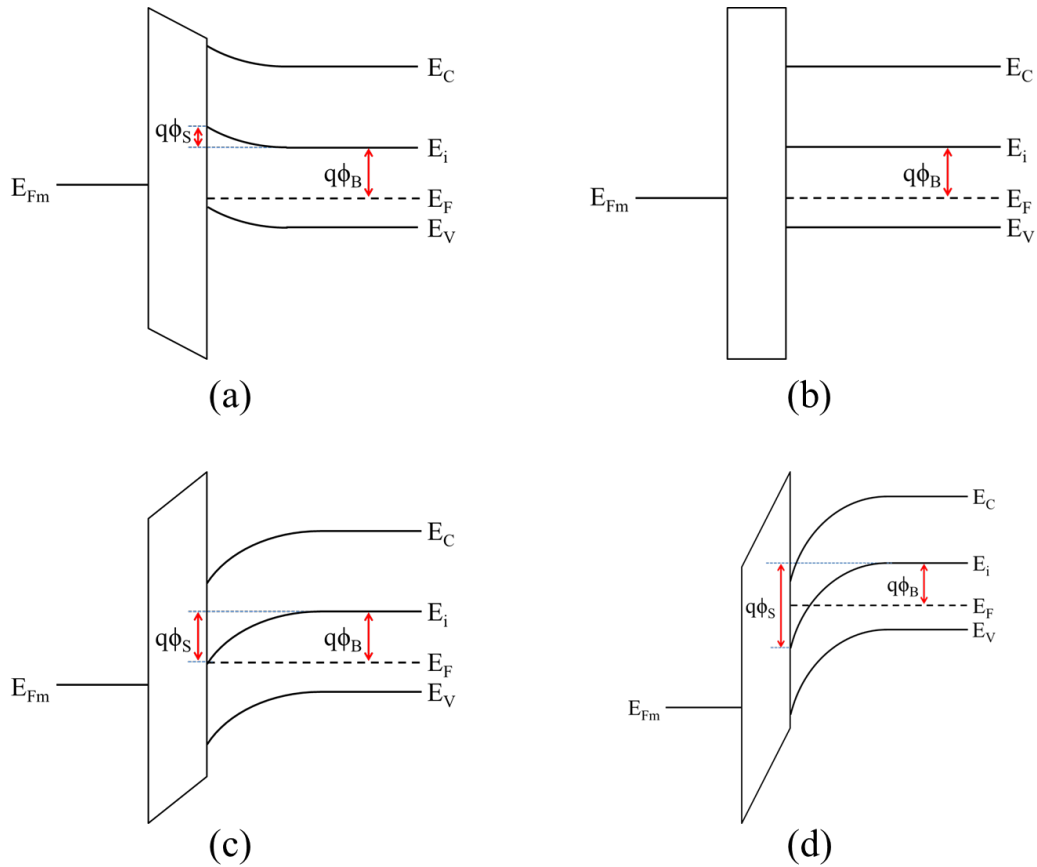


Figure 4.2: Band diagram of the MOS system illustrating the four basic modes: (a) accumulation, (b) flatband, (c) depletion, specifically the midgap point where the semiconductor is intrinsic at the oxide/semiconductor interface [$|q\phi_S|=|q\phi_B|$], and (d) the onset of strong inversion [$|q\phi_S|=2|q\phi_B|$]. $q\phi_S$ is the total band bending and $q\phi_B$ is the Fermi level in the semiconductor bulk.

There are four modes of operation related to the MOS capacitor which are of interest: accumulation, flatband, depletion, and inversion.

Accumulation occurs when a sufficiently large negative voltage is applied to the topside metal contact such that an extremely thin layer of holes are accumulated at the oxide/semiconductor interface. This accumulation layer of holes compensates for the charge applied to the gate contact and causes the bands of the semiconductor to bend upward at the oxide/semiconductor interface as shown in Figure 4.2 (a). The semiconductor at the oxide/semiconductor interface is effectively more p-type than the bulk semiconductor region. The resulting capacitance of the system in this case is simply the capacitance of the oxide. The capacitance per unit area is given in equation (4.2):

$$C'_{acc} = C'_{ox} = \frac{\epsilon_0 \epsilon_{ox}}{t_{ox}} \quad (4.2)$$

where ϵ_0 is the permittivity of free space, ϵ_{ox} is the relative permittivity of the oxide, and t_{ox} is the oxide thickness.

As the bias applied to the gate becomes more positive the system will eventually reach the flatband condition where the Fermi levels of the metal and semiconductor are aligned and there is no bending in the semiconductor bands as illustrated in Figure 4.2 (b). The voltage required to obtain this condition is known as the flatband voltage, V_{FB} . In an ideal MOS capacitor with a charge free oxide the flatband voltage is simply the difference of the metal work function, Φ_M , and the semiconductor work function, Φ_S as shown in equation (4.3) below.

$$V_{FB,ideal} = \Phi_M - \Phi_S = \Phi_{MS} \quad (4.3)$$

As the applied gate bias continues to become more positive, the mobile charge carriers (holes) will be repelled from the oxide/semiconductor interface leaving behind the ionized acceptor dopant atoms which are fixed in the semiconductor lattice. This mode of operation is known as depletion because the area at the oxide/semiconductor interface is depleted of mobile charge carriers. Figure 4.2 (c) shows the band diagram of a capacitor operating at a special point in the depletion regime where the corresponding gate voltage is known as the midgap voltage, V_{MG} . At the midgap voltage point the semiconductor is intrinsic at the oxide/semiconductor interface $[|q\Phi_S| = |q\Phi_B|]$. Assuming uniform doping concentration and full ionization of acceptor impurities in the depletion region (depletion approximation) the width of the depletion region, w_d , as a function of surface potential can be calculated as shown in the following equation:

$$w_d = \sqrt{\frac{2\epsilon_0\epsilon_s\phi_s}{qN_A}} \quad (4.4)$$

where ϵ_s is the relative permittivity of the semiconductor and all other variables have the same definitions as previously mentioned. While operating in the depletion mode the depleted region of the semiconductor acts as a parallel plate capacitor with a dielectric thickness equal to the depletion width, w_d . Therefore, the total capacitance of the system in the depletion mode, C_{tot} , is given by the series combination of the oxide and semiconductor capacitances as shown in equation (4.5):

$$C_{tot} = \frac{C_{ox} * C_S}{C_{ox} + C_S} \quad (4.5)$$

where C_S is the capacitance of the semiconductor depletion width.

As the bias applied to the gate continues to become more positive the depletion width continues to increase until the device moves into the next operation mode, inversion. Once the device is firmly in the inversion mode the depletion width is essentially fixed at a maximum value which can be determined by substituting $|q\Phi_S| = 2|q\Phi_B|$ into equation (4.4). Inversion mode occurs as the gate bias becomes positive enough so that minority carrier electrons are attracted to the oxide/semiconductor interface from the bulk of the semiconductor. Figure 4.2 (d) shows the band diagram of the MOS system at the onset of strong inversion where the corresponding voltage is known as the inversion voltage, V_{INV} . This voltage is also referred to as the threshold voltage, V_T , particularly when dealing with MOS field effect transistors. As soon as the concentration of electrons at the interface is higher than the concentration of holes at the interface the device is said to be in weak inversion ($|q\Phi_B| < |q\Phi_S| < 2|q\Phi_B|$), and once the concentration of electrons at the interface is higher than the concentration of holes in the bulk the device is said to be in strong inversion ($|q\Phi_S| > 2|q\Phi_B|$). The capacitance measured while the device is in the inversion mode of operation is dependent on the frequency of the measurement as will be discussed in the next subsection.

Expressions for the V_{INV} and V_{MG} voltages for the ideal case of no charge in the oxide can be derived as follows. In general the voltage charging the MOS system is equal to a combination of the voltage dropped across the oxide and the voltage dropped across the semiconductor. As shown in equation (4.6) the effective voltage charging the MOS system is the difference of the applied gate voltage and the flatband voltage.

$$V_G - V_{FB} = V_{ox} + V_S \quad (4.6)$$

In equation (4.6) V_{ox} is the voltage across the oxide and V_S is the voltage across the semiconductor, which is equal to the band bending at the oxide/semiconductor interface (i.e. $V_S = \Phi_S$). If we assume that the electric field in the oxide, $\overline{E_{ox}}$, is constant then it can be expressed as follows:

$$\overline{E_{ox}} = \frac{V_{ox}}{t_{ox}} = \frac{1}{t_{ox}} [(V_G - V_{FB}) - \Phi_S] \quad (4.7)$$

where equation (4.6) has been used to substitute for V_{ox} in equation (4.7). Because the displacement, D , at the oxide/semiconductor interface is constant the relationship shown in equation (4.8) below holds true:

$$\epsilon_0 \epsilon_S \overline{E_S} = \epsilon_0 \epsilon_{ox} \overline{E_{ox}} \quad (4.8)$$

where $\overline{E_S}$ is the electric field in the semiconductor. Solving equation (4.8) for $\overline{E_{ox}}$ and substituting into equation (4.7) results in the following:

$$\epsilon_0 \epsilon_S \overline{E_S} = \frac{\epsilon_0 \epsilon_{ox}}{t_{ox}} [(V_G - V_{FB}) - \Phi_S] = C'_{ox} [(V_G - V_{FB}) - \Phi_S] \quad (4.9)$$

where equation (4.2) has been used to simplify the leading expression to the oxide capacitance per unit area.

Assuming that the electric field is uniform inside the semiconductor depletion region and that the semiconductor outside of the depletion region is charge neutral, Gauss's law can be used to relate the electric field and permittivity of the semiconductor to the charges contained within the depletion region as shown in equation (4.10).

$$\epsilon_0 \epsilon_S \overline{E_S} = -Q'_S = -(Q'_n + Q'_d) \quad (4.10)$$

In equation (4.10) Q'_S is the total charge in the semiconductor depletion region per unit area, which consists of the inversion charge density per unit area, Q'_n , and the depletion

charge density per unit area, Q'_d . Equating equations (4.9) and (4.10) and solving for the inversion charge density per unit area results in the following expression:

$$Q'_n = -C'_{ox}[(V_G - V_{FB}) - \Phi_s] - Q'_d = -C'_{ox}[(V_G - V_{FB}) - \Phi_s] + \sqrt{2q\epsilon_0\epsilon_S N_A \Phi_s} \quad (4.11)$$

where the depletion approximation and equation (4.4) have been used to express the depletion charge density in its constituent terms. Equation (4.11) can now be used to derive expressions for the ideal midgap and inversion voltages.

First we will derive an expression for V_{MG} which corresponds to the onset of weak inversion. At the onset of weak inversion the inversion layer has not yet begun to form; therefore, the inversion charge density, Q'_n , must be equal to zero. At the onset of weak inversion we also know that the band bending at the oxide/semiconductor interface is equal to the magnitude of the bulk potential in the semiconductor (i.e. $\Phi_s = |\Phi_B|$). Inputting this information into equation (4.11) and solving for the gate voltage results in an expression for V_{MG} as shown in equation (4.12).

$$V_{MG} = V_{FB} + |\Phi_B| + \frac{1}{C'_{OX}} \sqrt{2q\epsilon_0\epsilon_S N_A |\Phi_B|} \quad (4.12)$$

Now we will consider the case of V_{INV} (also known as threshold voltage) which corresponds to the onset of strong inversion. The onset of strong inversion occurs when the band bending at the oxide/semiconductor interface is equal to twice the magnitude of the bulk potential of the semiconductor (i.e. $\Phi_s = 2|\Phi_B|$). At the onset of strong inversion there is some nonzero inversion charge that has already collected at the oxide/semiconductor interface, but because it is a relatively small amount of charge compared the total inversion charge in strong inversion we will approximate that $Q'_n = 0$ once again. Although not entirely accurate this will still give a good first order

approximation of the ideal V_{INV} . Substituting this information into equation (4.11) results in the expression for V_{INV} as shown in equation (4.13).

$$V_{INV} = V_{FB} + 2|\Phi_B| + \frac{1}{C'_{OX}} \sqrt{4q\epsilon_0\epsilon_S N_A |\Phi_B|} \quad (4.13)$$

Both equations (4.12) and (4.13) contain three terms which represent the various components of the applied gate voltage that are required to reach the point of interest (i.e. the onset of either weak or strong inversion). The first term represents the flatband voltage that must be overcome, the second term represents the amount of band bending at the oxide/semiconductor interface that is required, and the third term represents the voltage that is dropped across the oxide.

4.1.2 Capacitance-Voltage Curves

By sweeping the voltage of the gate through an appropriate range, the capacitance of the MOS device can be observed for all operation modes in a single curve known as a capacitance-voltage (C-V) curve. A standard set of C-V curves for a p-type MOS capacitor is shown in Figure 4.3. The most negative voltages cause the device to be in accumulation mode where the device capacitance is equal to the oxide capacitance. As the voltage increases the value of the capacitance begins to decrease as the device moves into the depletion mode. This is due to the addition of the capacitance of the depletion width in the semiconductor in series with the oxide capacitance. The capacitance continues to decrease until the depletion width reaches its maximum value. As the device transitions into the inversion mode one of two different traces will be observed depending on the frequency of the AC signal that is superimposed on the DC voltages that are being

swept. The lower trace corresponds to the higher frequency curve (e.g. 1 MHz). In this case the electrons needed to create the inversion layer cannot be generated quickly enough by thermal generation in the semiconductor bulk to respond to the AC signal. Consequently, no inversion layer is formed and the capacitance is still dictated by the depletion region with maximum depletion width in series with the oxide capacitance. The upper trace corresponds to the low frequency or quasi static curve. In this case the minority carrier electrons have enough time to create an inversion layer at the oxide/semiconductor interface. The inversion layer behaves very similarly to the accumulation layer and the total capacitance of the system returns to the value of the oxide capacitance, C_{ox} .

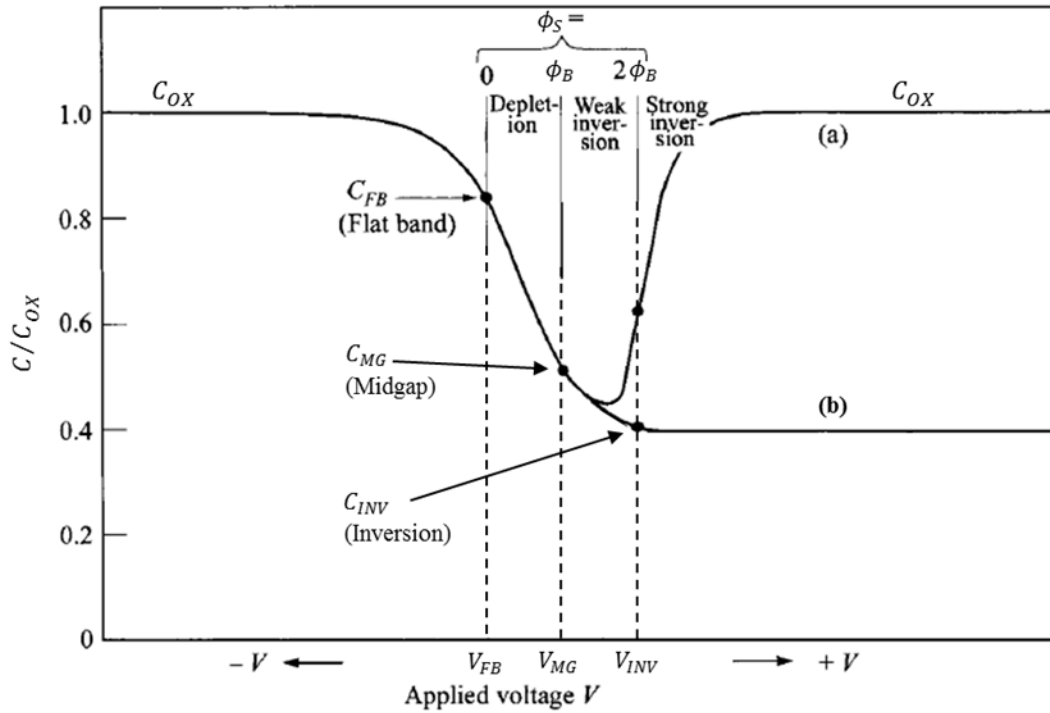


Figure 4.3: Capacitance voltage (C-V) curve for a p-type MOS capacitor displaying frequency dependence. Curve (a) illustrates low frequency/quasi static curve and curve (b) illustrates the high frequency curve. Adapted from [74].

4.1.3 Oxide Charge and Interface Traps

The discussion in the previous subsections is for the case of an ideal MOS capacitor, but of course real devices will have imperfections that affect how the device operates. Figure 4.4 shows the various types of charge imbalances in the MOS system (Si/SiO₂ system illustrated). These defects can arise from contamination during or after processing, difference in crystal structure of the oxide and the semiconductor, and stress on the device from high currents or radiation damage [74]. Of the four types of charge imbalances shown in Figure 4.4, the two that are relevant to our work are the oxide trapped charge and interface trapped charge. Both types of defects have a notable and distinct effect on the C-V curve of a device as will be detailed in the following paragraphs.

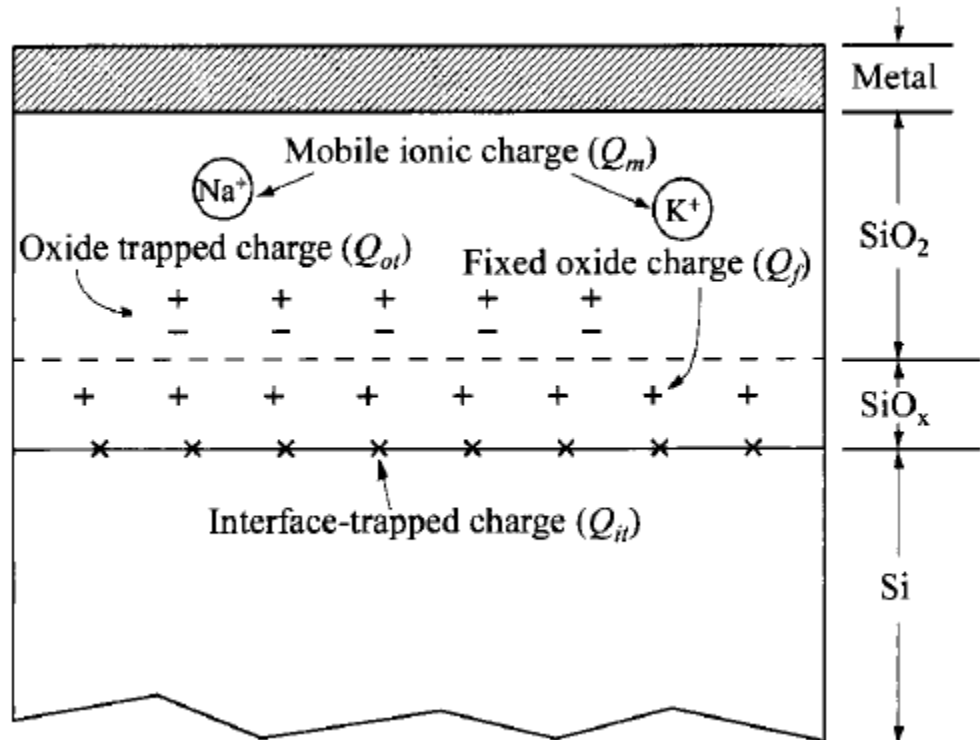


Figure 4.4: From [74]. Various types of charge imbalances that occur in MOS capacitors.

Oxide trapped charge causes the C-V curve to experience a pure translational shift. Because oxide trapped charge is generally positive the shift in the C-V curve for a p-type MOS capacitor would be towards more negative voltages (towards the left). This can be clearly understood by considering that any bias applied to the gate now has to overcome the charge in the oxide. As can be seen in equation (4.14) the amount of shift is dependent on the amount of charge in the oxide as well as the position of the charge in the oxide. In equation (4.14) the $\rho(x)$ term is a general function representing the charge distribution per unit volume in the oxide, and the distance x ranges from 0 at the metal/oxide interface to t_{ox} at the oxide/semiconductor interface. The closer the trapped charge is to the oxide/semiconductor interface the more pronounced the effect it has on the shift of the C-V curve. Because oxide charge shifts the entire C-V curve, the change in voltage from equation (4.14) will affect V_{FB} , V_{MG} , and V_{INV} equally.

$$\Delta V = \frac{1}{C_{ox}t_{ox}} \int_0^{t_{ox}} x\rho(x)dx \quad (4.14)$$

Unlike the oxide trapped charge, the interface trap charge is bias dependent. This is due to the fact that there is a distribution of interface trap levels with respect to energy in the bandgap of the semiconductor at the oxide/semiconductor interface, $D_{it}(E)$. Also of interest is the neutral level, $q\Phi_0$, of the interface states which can be set equal to the intrinsic level, E_i , in the bandgap as a good first approximation [74]. Above the neutral level the interface states are acceptor type (neutral when empty and negatively charged when occupied), and below the neutral level the interface states are donor type (neutral when occupied and positively charged when empty). As the gate bias varies the semiconductor's Fermi level is effectively moving through the bandgap at the

oxide/semiconductor interface, and as the Fermi level changes its relative position, interface states change their occupancy. This means that some of the charge on the gate is compensated for by populating or depopulating interface states, but in the ideal case the gate charge is entirely compensated for by changes in the depletion width. The result is that the depletion width, and therefore the total capacitance of the system, does not change as quickly with respect to gate voltage as in the ideal case. This has the effect of stretching out the C-V curve. The location and intensity of stretchout in the C-V curve depends on the location and density of the interface states with respect to energy in the semiconductor bandgap; therefore, unlike changes from trapped oxide charge, the distortions from interface states do not uniformly affect the C-V curve.

4.2 EXPERIMENTAL PROCEDURE

4.2.1 Device Fabrication

Oxidized silicon wafers were purchased from Si-Tech with a SiO₂ top layer of 50 nm ±5%. The silicon substrate was p-type ($\rho=5-10 \Omega\text{-cm}$) with <100> orientation. SiO₂ was removed from the back of the wafer by a backside etch procedure in which the bare 100 mm wafers were placed face down on supports and a few drops of 49% HF acid were placed on the back of the wafers. After the acid had removed the oxide, revealing a hydrophobic Si surface, the wafers were flipped vertical and flushed with flowing DI water to prevent the acid from reaching the wafers' front sides. The wafers were then rinsed in three successive DI water baths. After being blown dry with nitrogen, the wafers were immediately placed in a thermal evaporator where backside aluminum Ohmic

contacts of $\sim 1\mu\text{m}$ thickness were deposited. Following evaporation the wafers were sintered in a quartz furnace at 450°C with a nitrogen purge for 35 minutes. The wafers were cooled to room temperature, and then the silicon wafers were cleaved into square samples of approximately $12\text{ mm} \times 12\text{ mm}$. The samples were stored in rough vacuum until irradiation. After irradiation an array of aluminum contacts was deposited on top of the SiO_2 via thermal evaporation through a shadow mask. The circular topside contacts were approximately $0.5\ \mu\text{m}$ thick and 1 mm in diameter with a center-to-center spacing of 2.5 mm . Ideally, the fabrication of the topside contacts resulted in a 5×5 array of MOS capacitors as shown in Figure 4.5; however, due to slight misalignments during thermal evaporation some samples had fewer than 25 capacitors. In this experiment there were nine samples that were irradiated with HCl beams of various charge states and fluences as described below, and one pristine sample that served as the control.

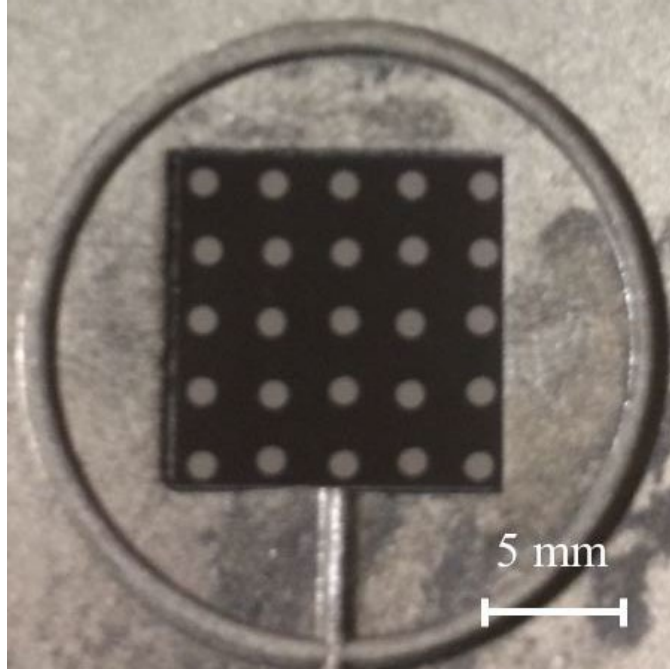


Figure 4.5: Si/SiO₂ sample containing 25 MOS capacitors arranged in a 5x5 array.

4.2.2 HCI Irradiation

The highly charged ion irradiation was performed with the Clemson University Electron Beam Ion Trap (CUEBIT). The CUEBIT setup and basic operation can be found in [75], and are described in Chapter 3 of this dissertation. Some previous results with electronic devices irradiated by the CUEBIT can be found in [76-78]. The 12 mm x 12 mm Si/SiO₂ samples were mounted on a stainless steel platen and loaded into the CUEBIT target chamber. The base pressure of the target chamber was $\sim 1 \times 10^{-8}$ Torr, and the pressure in the beamline was in the low 10^{-9} Torr range. No external bias was applied to the samples while they were being irradiated, but the backsides of the samples were grounded. In total there were nine samples irradiated with Ar^{Q+} beams at normal incidence. Specifically, three samples were irradiated for each of the following charge states: Q = 4, 8, and 11, which have potential energies of 138 eV, 567 eV, and 2,004 eV, respectively. Beams of the desired charge state were directed onto the sample by means of an analyzing magnet between the source and the target chamber. The kinetic energy of all ion beams incident on the samples was approximately 1 keV [53]. This was achieved with a custom deceleration lens in front of the target chamber. Beam currents were measured at various times throughout each irradiation using a Faraday cup in the same plane as that of the sample. Based on the measured beam currents, the nominal ion fluences were calculated to be in the range of $\sim 3 \times 10^{13}$ to $\sim 1 \times 10^{14}$ ions/cm². All Ar^{Q+} beams produced by the EBIT were observed to be Gaussian in nature as determined by a beam viewer (HRBIS-4000 from Beam Imaging Solutions) and Faraday cup

measurements. A typical Ar beam profile is shown in Figure 4.6 for the case of $Q = 8$.

The FWHM of the HCI beams was ~ 3 mm.

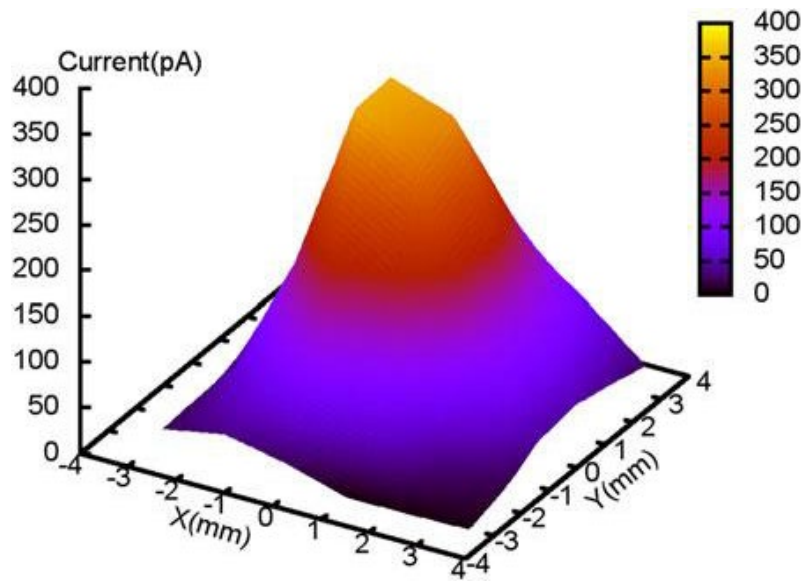


Figure 4.6: Typical beam profile for Ar^{Q+} irradiation (Q=8 is shown).

4.2.3 Device Characterization

In order to characterize the effects of the HCI irradiations on our devices, high frequency capacitance-voltage (HFCV) curves were measured for each capacitor (up to 25 per sample) using an HP 4280A 1 MHz C-V meter. All C-V measurements were performed in a probe station which shielded the sample from light, vibration, and electromagnetic interference. The sample was held in place with a vacuum chuck, and micromanipulator controlled probe tips were used to make electrical contact to the device. Only post irradiation measurements were possible due to the topside contacts being deposited after the irradiation. HFCV measurements were also performed on several pristine capacitors that never entered the target chamber and which served as a control or proxy for pre-irradiation measurements. The C-V data for the pristine devices showed good uniformity across the sample, indicating that any changes observed in other samples arises purely from effects of the HCI irradiation.

4.3 HCI RADIATION EFFECTS ON C-V CHARACTERISTICS – QUALITATIVE

4.3.1 Shift and Stretchout

In order to analyze the effects of the HCI irradiation on the MOS capacitors, we extracted information related to three parameters for each C-V curve: the flatband voltage (V_{FB}), the midgap voltage (V_{MG}), and the inversion voltage (V_{INV}). The flatband voltage corresponds to the point at which the energy bands in the MOS system have no curvature, the midgap voltage corresponds to the point where the silicon surface is intrinsic, and the

inversion voltage corresponds to the onset of strong inversion at the silicon surface. To obtain these key indicators the flatband, midgap, and inversion capacitances (C_{FB} , C_{MG} , and C_{INV}) were first calculated by using equation (4.5) with various depletion widths [74, 79, 80]. For the case of flatband capacitance the depletion width is set equal to the Debye length, L_D , which is given in equation (4.15) where all variables are the same as previously defined. Equation (4.4) is used to calculate the depletion width for both midgap and inversion capacitances. For the case of C_{MG} the band bending is set equal to the magnitude of the bulk potential ($|q\Phi_S| = |q\Phi_B|$), and for the case of C_{INV} the band bending is set equal to twice the magnitude of the bulk potential ($|q\Phi_S| = 2|q\Phi_B|$).

$$L_D = \sqrt{\frac{\epsilon_0 \epsilon_s kT}{q^2 N_A}} \quad (4.15)$$

The measured C-V data and the calculated capacitance values are then used to determine the corresponding voltages V_{FB} , V_{MG} , and V_{INV} . These voltages can track two important changes in the C-V curve: shifts and stretchout. Shifts refer to translational movement of the entire C-V curve along the applied voltage axis, and stretchout refers to changes in the difference between any two of the voltages. The significance of these voltages can be better understood with the help of Figure 4.2, which illustrates the band diagrams of the MOS system under various bias conditions. As the bias on the topside contact is made increasingly more positive relative to the semiconductor, the bands of the semiconductor bend down from flatband by an increasing amount. For the band bending between the flatband condition, Figure 4.2 (b), and the onset of strong inversion, Figure 4.2 (d), it can be seen that the semiconductor Fermi level (E_F) at the Si/SiO₂ interface is effectively moving through a significant portion of the semiconductor

bandgap. This movement of the Fermi level can be used to qualitatively investigate interface traps and their density as a function of energy, $D_{it}(E)$, in the Si bandgap.

Now we will consider what can be determined from analyzing these three key voltages for the C-V curves shown in Figure 4.7, which were measured on two of our samples [77]. The red solid curve is from a capacitor on the pristine sample and serves as a control. The blue dashed curve is from a capacitor on a sample that was irradiated with Ar^{8+} and serves as a good representative for devices that experienced significant irradiation (i.e. devices that were spatially aligned with the peak of the beam's Gaussian distribution). Upon initial inspection the only difference between the two curves in Figure 4.7 appears to be that the curve for the irradiated device has experienced a large shift towards more negative voltages. Making the reasonable assumption that defect centers at the Si/SiO₂ interface are acceptor type above the middle of the bandgap and donor type below the middle of the bandgap, it can be inferred that changes in the midgap voltage do not originate from defects centers at the interface. With no influence from interface traps at the midgap point, the increase of $|V_{MG}|$ in our data indicates the presence of some type of positive charge trapped in the oxide [74]. Upon closer inspection of the curves in Figure 4.7, it is evident that the V_{INV} is approximately the same for both the pristine device and the irradiated device. This indicates that a significant amount of stretchout between midgap and inversion is occurring for the irradiated devices in addition to the translational shift. The combination of stretchout and shift was observed for the capacitors that were significantly affected by the HCI irradiation, but it should be noted

that some of the capacitors towards the edge of the sample behaved similarly to the pristine devices due to the sample size being larger than the FWHM of the HCI beam.

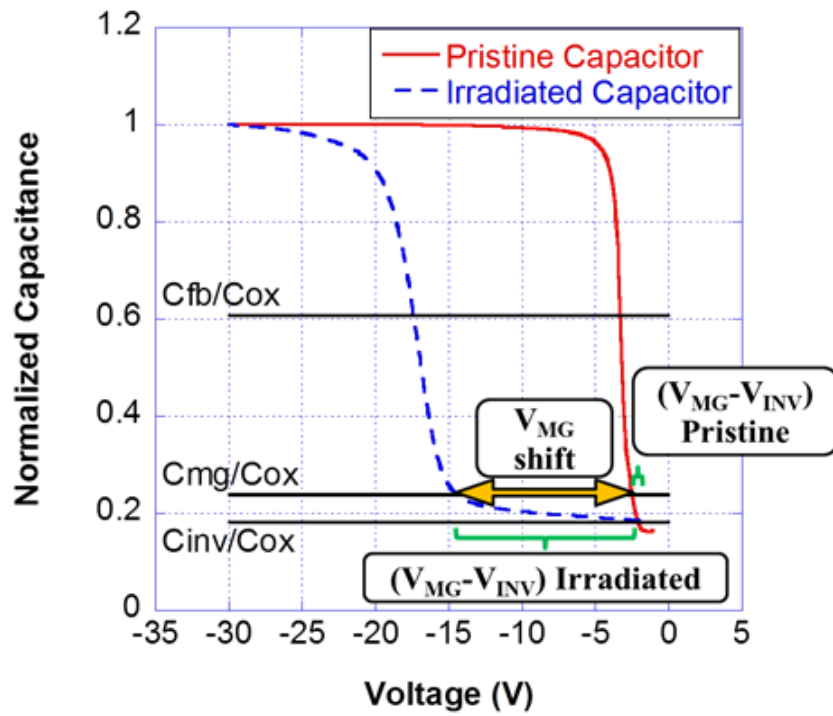


Figure 4.7: C-V curves for two different capacitors on separate samples. One sample was irradiated and the other one is pristine. Sample was irradiated with Ar^{8+} to a fluence of 4.20×10^{13} ions/cm². The midgap shift and stretchout between midgap and inversion points are also shown.

The stretchout in the C-V curves indicates the presence of interface traps at the Si/SiO₂ interface of the irradiated capacitors [74, 79]. The small rate of increase for the measured capacitance between the inversion and midgap points indicates that the interface traps are somewhat localized around one energy in the silicon bandgap, and therefore are likely predominantly due to one type of defect. This can be understood by considering the extreme case of infinite D_{it} at a specific energy level in the Si bandgap. As more charge is applied to the metal gate of the MOS device, the interface traps will adjust their occupancy in order to balance the charge applied on the metal. Because there are an infinite number of interface traps at that energy level, the effective position of the Fermi level at the interface does not need to change in order to balance the charge on the metal. No change in the Fermi level position at the interface means no change in the depletion width in the Si, and consequently no change in the capacitance. For the case of a large (but finite) D_{it} , the effective Fermi level position at the interface will change more slowly with changes in bias past the energy level where interface traps are the most dense. The slow change in position of the Fermi level at the interface in the bandgap corresponds to a small rate of change for the depletion width as well as the overall capacitance. As illustrated in Figure 4.2 (c) and (d), the Fermi level at the interface is in the upper half of the band gap for voltages between V_{MG} and V_{INV} . Since almost all of the stretchout in the C-V curves occurs between the inversion and midgap points, we know that the largest density of interface traps are in the upper half of the band gap. Knowing that the bulk potential of the Si substrate is approximately $q\phi_B=0.31$ eV (based on the average resistivity), we can more precisely say that the distribution of interface states

exist somewhere between the middle of the band gap, E_i , and an energy level 0.31 eV above E_i .

4.3.2 Process for Defect Creation

It is likely that defects at the interface of the irradiated devices were created by a two stage process involving the interaction of holes with defect centers in the oxide, hydrogen, and P_b centers at the interface as described in the literature [81-87]. Holes in the oxide can be created by the HCIs in a couple of different ways. As an HCI approaches, but before it actually impacts the sample, it begins capturing electrons from the surface. As electrons are removed from the surface, an abundance of holes will begin accumulating in the SiO_2 below the HCI in a nanometer-scale region. When the HCI impacts the sample several electron-hole pairs will be created as with singly charged ion irradiation [11, 29, 39, 88]. Due to the large disparity of mobilities for electrons and holes in SiO_2 , $20 \text{ cm}^2/\text{V}\cdot\text{s}$ and $4 \times 10^{-9} \text{ cm}^2/\text{V}\cdot\text{s}$, respectively [89], there will be a large portion of electrons that move away from the HCI impact site before recombination can occur. Since there is no applied bias during irradiation, the dispersion of holes throughout the oxide will result primarily from diffusion. Simulations using the stopping and range of ions in matter (SRIM) program indicate that the neutralized argon atoms will come to rest only a few nanometers into the SiO_2 layer and will have a negligible effect on the behavior of the MOS devices [90]. It is the created holes and their subsequent diffusion towards the interface that result in device damage in the bulk and at the interface.

The first stage of the two stage process for interface trap creation involves the capture of a hole at a defect site in the oxide. The dominant oxide hole trap in SiO₂ is due to an oxygen vacancy, which becomes a positively charged E' center after capturing a hole [81, 87]. The E' centers which are near the interface are then able to interact with H-passivated Si dangling bonds at the Si/SiO₂ interface. This is the second stage of the process. Lenahan and Conley have claimed that hydrogen will be exchanged between E' centers in the oxide and Si dangling bonds at the interface via the following equation [82]:



where λ indicates the relative abundance of diatomic hydrogen and is used to balance the equation. As hydrogen is exchanged between the oxide traps and the interface traps there is no net change in charge for either defect site. The end results of this process are positively charged defects in the oxide, which are responsible for the shift seen in V_{MG} , and Si dangling bond defects at the Si/SiO₂ interface, which are responsible for the stretchout. The energy range where our D_{it} is concentrated agrees well with the energy level for the P_{b0} silicon dangling bond defect in <100> silicon as reported in [91]. It should be mentioned that several groups have also argued that H^+ ions created from hole trapping in the oxide will react with defect sites at the interface, resulting in molecular hydrogen and a dangling Si bond [84-86].

4.4 DATA ANALYSIS

4.4.1 Capacitor Array vs. Single Capacitor

In an ideal experiment each sample would have had a single capacitor with a diameter equal to that of the FWHM of the HCI beam. These ideal samples would have been aligned such that the HCI beam and capacitor fully overlapped as shown in Figure 4.8 (a). Unfortunately there were two limiting issues with alignment in our experimental setup that did not allow us to pursue this ideal scenario. The first is that there is no precise way to align the samples in the EBIT target chamber. The second factor negatively influencing alignment was the need to remove the sample from the EBIT and perform a thermal evaporation for the topside contacts in a separate piece of equipment (Edwards Thermal Evaporator). It is possible that the first issue alone could have been overcome with some simple restructuring of the sample mount and possibly some tweaking of the target chamber; however, the second issue would have made all of that effort for nothing. In the future we hope to be able to operate an e-beam evaporator attached to the EBIT target chamber which would likely alleviate our alignment issues and allow us to obtain more accurate data.

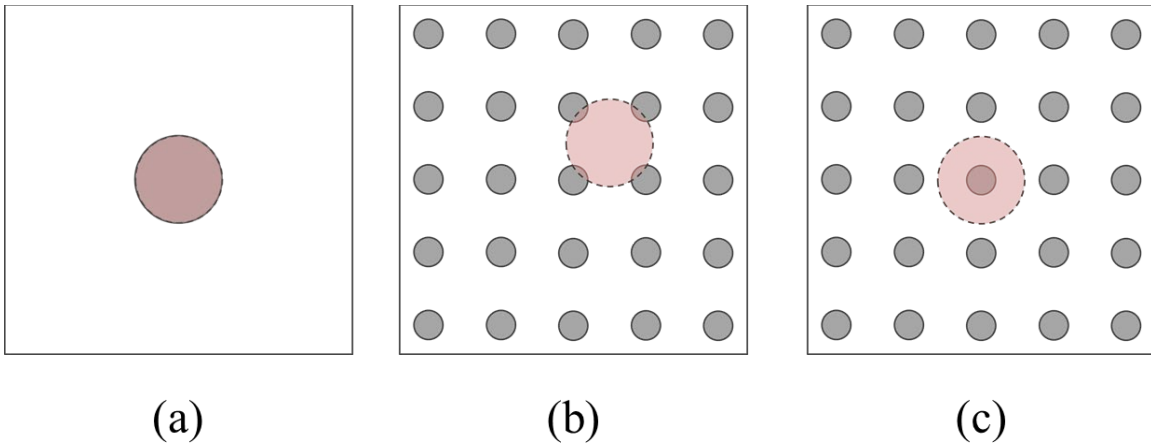


Figure 4.8: HCI beam alignment with different sample structures (drawn to scale). Dashed circles filled with transparent pink color represents FWHM of HCI beam (3 mm diameter). Solid gray circles represent capacitors. (a) FWHM of HCI beam fully overlaps with single 3 mm diameter capacitor, (b) FWHM of HCI beam partially incident on four capacitors in array structure (1 mm diameter capacitors with 2.5 mm center-to-center spacing), and (c) FWHM of HCI beam fully incident on one capacitor in array structure.

Instead of irradiating a single capacitor per sample, we have created an array of smaller capacitors on each sample as shown previously in Figure 4.5. Due to the alignment issues described above we had to take great care when analyzing the data. Consider a couple of extreme cases as displayed in Figure 4.8 (b) and (c) which could be encountered when irradiating such an array structure. In Figure 4.8 (b) the FWHM of the beam is partially incident on several devices, but does not fully encompass any one device. Conversely in Figure 4.8 (c) the FWHM of the beam completely envelops only one capacitor. It is important to emphasize that we are illustrating the area related to the FWHM of the HCI beam, and although the most severe changes will be observed inside this area, there will still be some changes to devices that are immediately outside of the beam's FWHM area. In order to accommodate these two extreme cases and everything in between we developed a special method of averaging the values across the sample which is detailed in the following paragraphs. Even though our averaging technique does not necessarily produce data that is as accurate as it would be in the ideal situation shown in Figure 4.8 (a), it does produce a precise and repeatable method to compensate for unavoidable misalignments. This consistency between samples is of the utmost importance as we investigate the charge state dependent changes in our electrical characterization.

4.4.2 Gaussian Analysis

After each irradiation, we extracted the key parameters (V_{FB} , V_{MG} , V_{INV} , and their differences) for each capacitor on a sample. For example, Figure 4.9 shows $|V_{MG} - V_{INV}|$

values for a 5x5 array of capacitors that was irradiated with Ar⁸⁺. A linear interpolation is performed on the data of interest in MATLAB, and then a 2D Gaussian fit is applied to the resulting matrix of values using MATLAB's *cftool* application. Figure 4.9 shows such a 2D Gaussian fit overlaying the extracted data from the electrical characterization. The clear spatial dependence of the voltage data in Figure 4.9 shows a strong correlation to the Gaussian shape of the incident HCI beam, and confirms the validity of our analysis technique. In order to accommodate the two extreme cases of alignment displayed in Figure 4.8 (b) and (c), the data was averaged using the following equation:

$$|V_{MG} - V_{INV}|_{Average} = \frac{\iint_A (Gaussian\ Fit) dA}{\iint_A dA} \quad (4.17)$$

where the integrations are performed across the area of the sample, A . Therefore, the data from each sample can be reduced to a single representative average value.

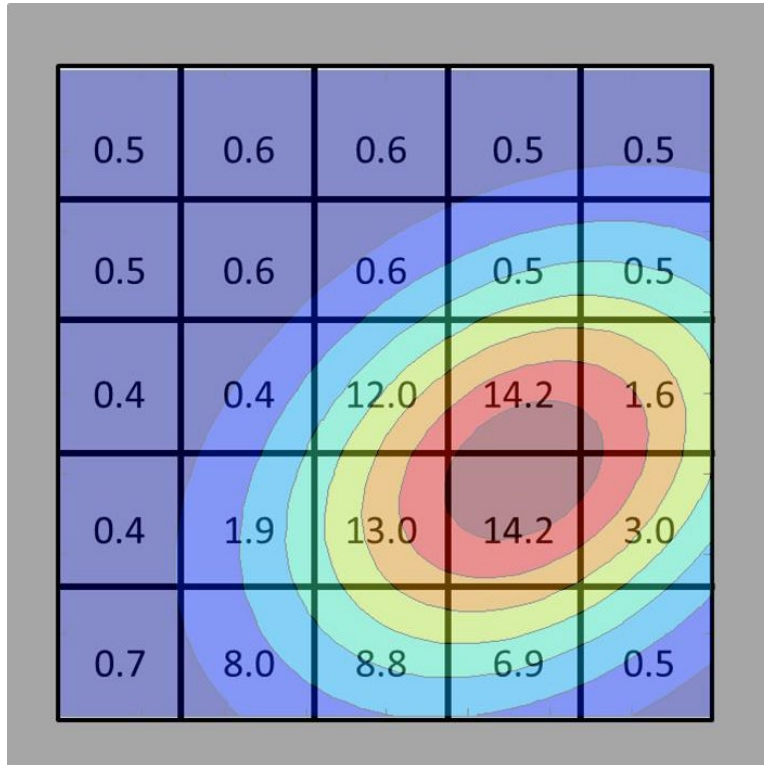


Figure 4.9: Numerical representation of the stretchout between midgap and inversion in Volts for the 5x5 capacitor array shown in Fig. 4.1 (i.e. the $|V_{MG} - V_{INV}|$ values for the 25 capacitors) with the 2D Gaussian fit overlaid ($R^2 = 0.9407$). The stretchout values of the Gaussian fit range from approximately 0.5 V (dark blue) to a little above 14 V (dark red).

4.4.3 Fluence Correction

Our analysis technique also adjusts the nominal fluence calculated during the irradiation to a more appropriate value which is displayed in the figures contained in this chapter. This fluence adjustment is achieved by integrating the Gaussian fit over the area of the sample, dividing it by the integration of the Gaussian fit over an area equal to that of the Faraday cup (FC) used to measure the beam current, and then multiplying the resulting quotient by the nominal fluence. This process is shown in equation (4.18) below:

$$Fluence_{Adj} = Fluence_{Nom} \left(\frac{\iint_{Sample} (Gaussian\ Fit) dA}{\iint_{FC} (Gaussian\ Fit) dA} \right) \quad (4.18)$$

The main source of error in the nominal fluence that is corrected by this calculation arises from the difference in the sample size (12 mm x 12 mm) and the Faraday cup that is used to measure the beam current (2.54 cm diameter; approximated as 22.5 mm x 22.5 mm). Equation (4.18) is also able to correct fluence errors arising from slight misalignment of the sample during irradiation. This is done by centering the area of integration for the integral in the denominator of equation (4.18) on the peak value of the Gaussian fit as opposed to the center of the sample. Although the Gaussian fits used for this calculation are based on the voltage data, it has been shown to correlate strongly to the Gaussian nature of the HCI beam as shown in Figure 4.6.

4.5 CHARGE STATE DEPENDENCE OF C-V CURVE CHANGES – QUANTITATIVE

4.5.1 $|V_{MG} - V_{INV}|$ Stretchout

Figure 4.10 shows the results of the analysis of the midgap to inversion stretchout data for all nine samples that were irradiated. The average difference between midgap and inversion points for the pristine sample was 0.21 V. The results in Figure 4.10 indicate that the fluences used in these experiments were such that the effect on the MOS devices are approaching saturation, and for the case of the Ar^{11+} data the effect is diminished at the highest fluence. One possible reason for this is a competing annealing process that becomes more dominant as irradiation times increase. This type of effect has been observed in Schottky diodes exposed to swift heavy ions [92-95]. The higher charge state beams produced in the EBIT have lower beam currents; therefore, devices irradiated at higher charge states require a longer irradiation time to reach a given fluence compared to devices irradiated with lower charge states. So, it is possible that the longer irradiation time for the highest fluence point for the Ar^{11+} data set shows a reduced effect due to an increased amount of room temperature annealing.

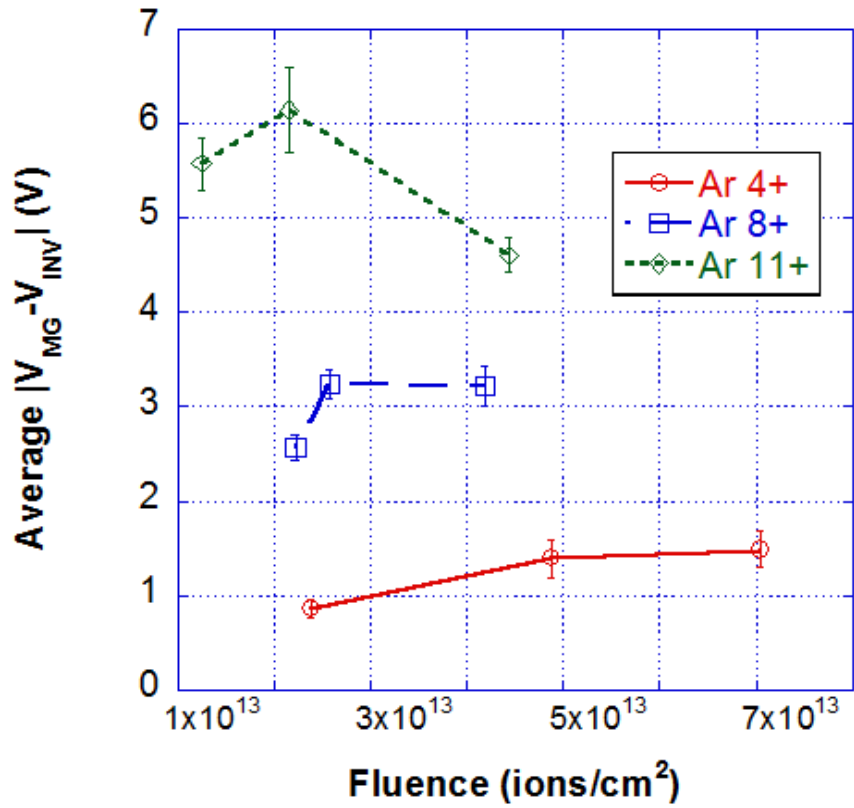


Figure 4.10: Average $|V_{MG} - V_{INV}|$ values for each of the nine irradiated samples. Sample averages were obtained by using the 2D Gaussian fit of the voltage data. The fluences in this plot have been adjusted from the nominal fluence using equation (4.18) from Section 4.4.3.

Because our fluences appear to be in the saturation regime, we were unable to gain any useful information by investigating the rate of change in $|V_{MG} - V_{INV}|$ with respect to fluence as we have done previously with V_{FB} data [76]. As an alternative, we have calculated the average effect observed for a given charge state across all fluences. Because we are interested in the change in the stretchout, $\Delta|V_{MG} - V_{INV}|$, the value of $|V_{MG} - V_{INV}|$ recorded for the capacitors on the pristine sample was subtracted from the average $|V_{MG} - V_{INV}|$ for a given charge state. In essence, we are using the pristine sample as a proxy for pre irradiation measurements since top contacts were deposited after irradiation. The result of this calculation is $\Delta|V_{MG} - V_{INV}|$ as a function of charge state as shown in Figure 4.11. A power law fit to the data shows that the stretchout between midgap and inversion voltages varies as approximately $Q^{1.7}$.

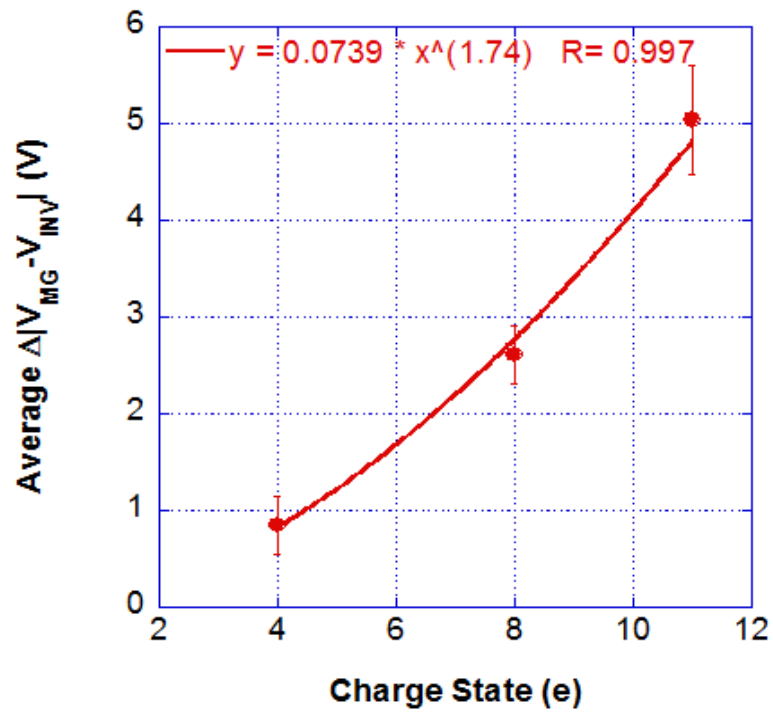


Figure 4.11: Average stretchout between midgap and inversion for all samples of a given charge state minus the corresponding stretchout seen in the pristine sample. Also shown is a power law fit showing that stretchout between midgap and inversion varies as $Q^{-1.7}$.

4.5.2 V_{MG} Shift

The results of applying our analysis technique to the V_{MG} data is shown in Figure 4.12 for all nine samples that were irradiated. The average magnitude of the midgap voltage for the pristine sample was 1.24 V. Just as with the $|V_{MG} - V_{INV}|$ data for the Ar^{11+} , it is clear that the effects actually begin to lessen for the highest fluence levels for all charge states. As mentioned earlier, this is possibly due to an annealing effect which becomes more prominent as irradiation times are increased. Because the ion fluences are not in a linear regime, the data points for each charge state were averaged such that each charge state is represented by a single average V_{MG} value. The average value of V_{MG} for the pristine capacitors was then subtracted from these averages in order to track the ΔV_{MG} as a function of charge state. The results of this analysis are shown in Figure 4.13. Applying a power law fit to this data indicates that the shift in V_{MG} varies as approximately $Q^{-1.8}$.

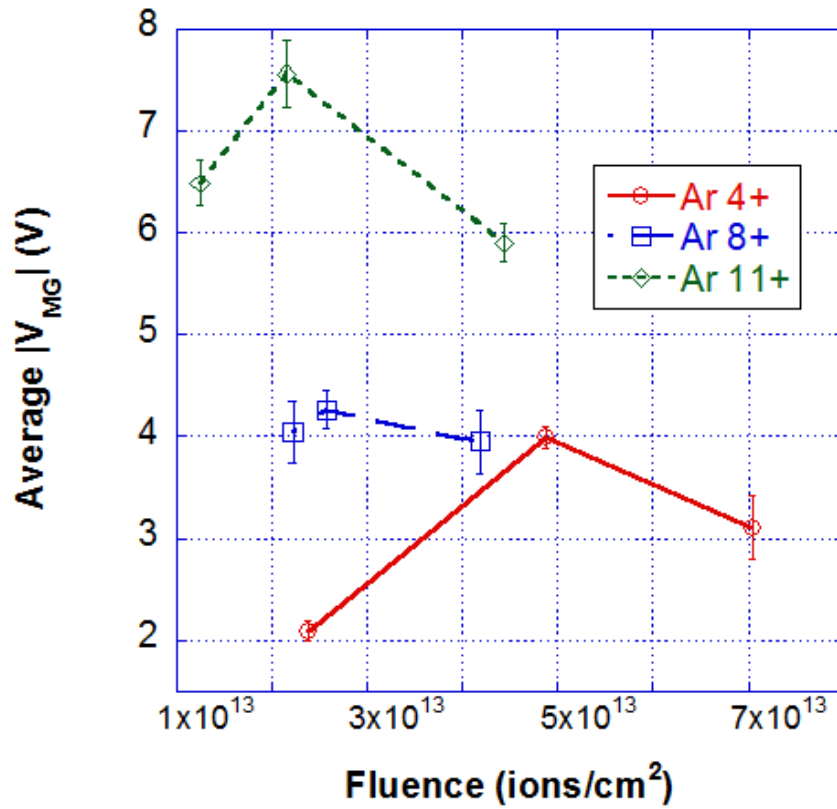


Figure 4.12: Average V_{MG} values for each of the nine irradiated samples. Sample averages were obtained by using the 2D Gaussian fit of the voltage data. The fluences in this plot have been adjusted from the nominal fluence using equation (4.18) from Section 4.4.3.

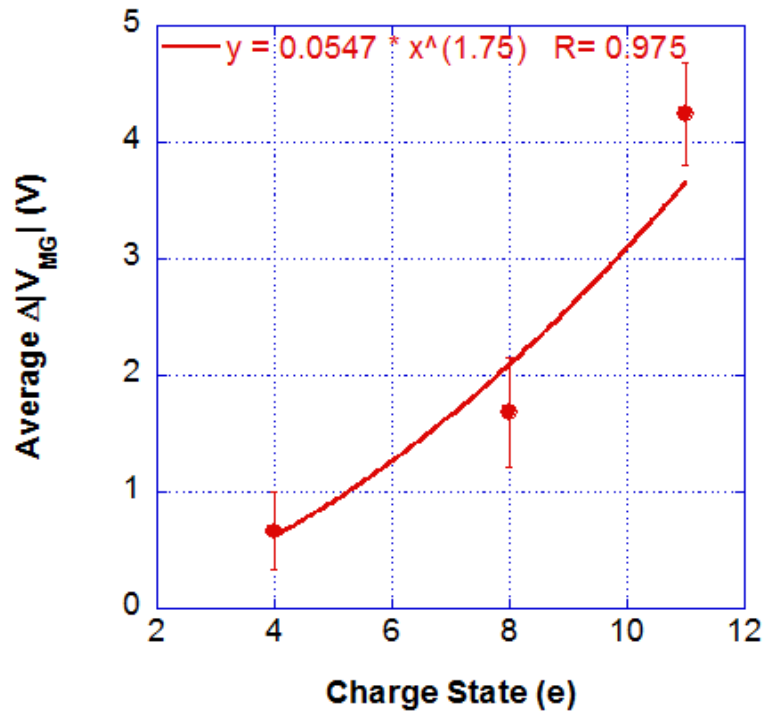


Figure 4.13: Average midgap voltage for all samples of a given charge state minus the average midgap voltage seen in the pristine sample. Also shown is a power law fit showing that shifts of midgap voltage vary as $Q^{-1.8}$.

4.5.3 Summary of Charge State Dependent Effects

These results indicate that the creation of both oxide and interface traps have approximately the same Q dependency. This Q dependency is also similar to the power law that we observed for V_{FB} shifts in thicker oxides after HCI irradiation ($\sim Q^{2.2}$) [76]. It is also important to note that the energy loss of HCIs in thin carbon membranes has been reported to display quadratic dependence on charge state [96]. The commonality between the Q -dependent changes in our C-V curves and the Q -dependent energy loss should not be dismissed as coincidence, but rather this similarity could be interpreted as indicating that there is some intrinsic relationship between the internal mechanisms of energy loss for HCIs in solids and the resultant damage that we observe in our electrical characterization measurements. Numerical modeling, similar to what has been performed for ionizing radiation incident on MOS capacitors [97], could provide additional insight into the charge state dependent effects produced in electronic devices and materials; however, care would need to be taken to account for the unique properties of slow HCIs (i.e., low kinetic energy and relatively high potential energy).

4.6 SUMMARY AND CONCLUSIONS

The basic model and operation of MOS capacitors has been described. MOS band diagrams were used to help explain the various operating modes of the capacitors, and the ideal C-V curve helped illustrate the voltage dependent behavior of the capacitance. Expressions for midgap voltage and inversion voltage were derived for the ideal case of a

charge free oxide and interface. The effects of oxide trapped charge and interface trapped charge on capacitor behavior were also considered.

We have irradiated Si/SiO₂ samples with slow HCIs in an electron beam ion trap facility at Clemson University in order to gain a better understanding of how this relatively unexplored type of radiation affects electronic devices. The samples consisted of an array of top metal contacts evaporated post radiation to form MOS capacitors, and HFCV curves showed a translation of V_{MG} and an increase in the stretchout between inversion and midgap voltages compared to pristine capacitors. These changes indicate the creation of oxide trapped charges and interface traps, respectively. It was determined that the oxide trapped charges were most likely due to E' centers, and the interface traps were most likely due to P_b defects. Using a data analysis technique based on a 2D Gaussian fit of the voltage data, we found a charge state dependence of $Q^{-1.7}$ for the stretchout of the C-V curves between midgap and inversion, and a charge state dependence of $Q^{-1.8}$ for the shift in V_{MG} . This work provides a good foundation for future applications related MOS based HCI sensors in fusion reactors and outer space operations by providing a better understanding of how MOS devices are affected by HCI irradiation. Future work is planned for MOS irradiations with thin metal contacts (~20nm) deposited prior to HCI irradiation, and will focus on varying the fluence, kinetic energy, and incidence angle of different ion species. Hopefully the results will provide a deeper understanding of HCI effects on electronic materials and devices.

CHAPTER 5

EFFECTS OF SLOW Na^+ IRRADIATION ON SCHOTTKY DIODES

5.1 INTRODUCTION

Schottky diodes have been investigated as potential radiation sensors for low kinetic energy ions (≤ 2 keV). Schottky diodes were chosen primarily because of their simple device structure, ease of fabrication, and their ubiquity in modern electronic devices. These factors mean that Schottky diode sensors could easily be integrated into existing systems with minimal variation from previous designs. Initially we intended to investigate Schottky diodes as potential sensing devices for slow highly charged ions (HCIs) with low kinetic energy; however, the electron beam ion trap (EBIT) facility which is used to create the HCIs has been out of operation for a couple of years due to unforeseen setbacks. As an alternative, we have chosen to investigate Schottky diodes for sensing Na^+ ions with low kinetic energy. This decision was made for a couple important reasons: (1) Although the singly charged ions obviously do not have the same potential energy as HCIs, the results from experimenting with Na^+ can be used as a baseline when comparing to later HCI experiments since it will help in isolating the effects of the kinetic energy. (2) Nienhaus et al. have performed several interesting experiments using Schottky diodes as detectors for chemiluminescent reactions at the metal surface. The chemical reaction at the metal surface creates hot carriers that are subsequently injected into the semiconductor creating a “chemicurrent” [20-23]. This work has inspired us to investigate the possibility of using Schottky diodes to detect hot carriers generated in the

metal layer of the diode by the kinetic energy of the incident ion beam. In order to be detected with traditional solid state detectors the ions must be able penetrate into the depletion region of the device, where they generate electron hole pairs that can be collected and measured as a current. Because low kinetic energy ions are not able to penetrate into the depletion region, detection of the “kine-current” would be useful for the detection of low kinetic energy ions. These experiments will also yield valuable insights into how slow ions interact with semiconductor devices, and what, if any, lasting changes result from the interaction. The remainder of Section 5.1 provides the theoretical background related to Schottky diode operation and the extraction of key parameters. The details of the experimental procedure are given in Section 5.2. In Sections 5.3 and 5.4, we present results related to detection of a kine-current and the radiation tolerance of the diodes, respectively. Section 5.5 contains a brief summary and conclusion.

5.1.1 Schottky Diode Structure and Operation

There are several different design variations for Schottky diodes, but all Schottky diodes are ultimately just a metal semiconductor contact. The most simplistic Schottky diode structure consists of a semiconductor substrate with a rectifying/Schottky metal contact on one side and a non-rectifying/Ohmic metal contact on the opposite side as shown in Figure 5.1. Because Schottky diodes are typically manufactured with n-type semiconductors, that is what will be presented here; however, it is also possible to fabricate Schottky diodes using p-type semiconductors. Initially, only the ideal structure

and operation will be discussed, but in Section 5.1.2 some of the non-ideal, second order considerations of diode modeling will be presented.

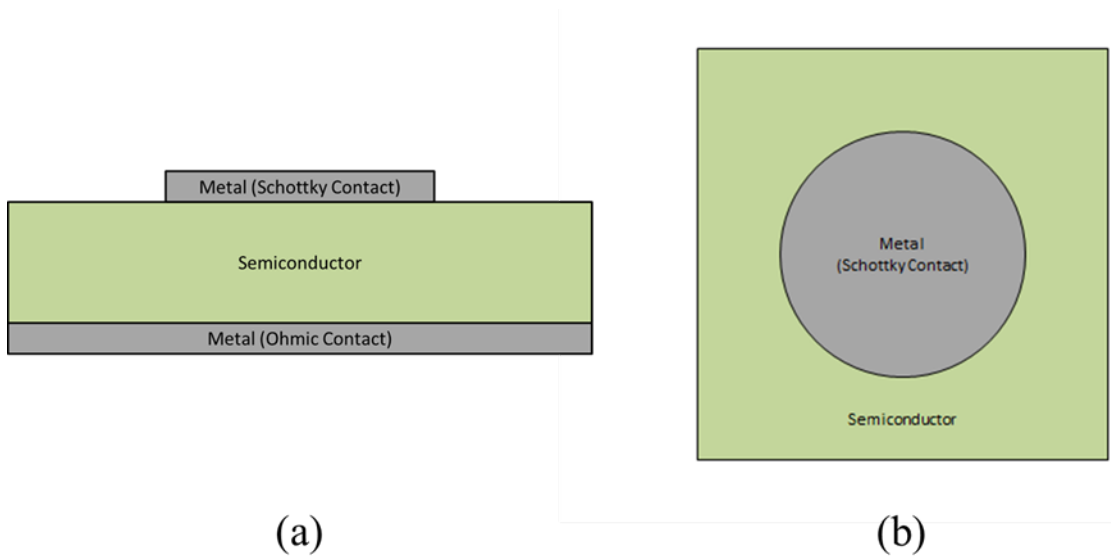


Figure 5.1: Simple Schottky diode structure: (a) cross sectional view and (b) aerial view. (layer sizes not shown to scale).

In order to better understand the formation and operation of Schottky diodes, the band diagrams shown in Figure 5.2 should be considered. In Figure 5.2 (a) the energy levels for the metal and semiconductor are shown separately before they are brought into close contact with one another. In the band diagram of Figure 5.2, E_C is the lower edge of the conduction band, E_V is the upper edge of the valence band, and E_F is the Fermi level in the semiconductor; the energy level at which there is a 50% probability of finding an electron. The difference between E_C and E_V is the semiconductor bandgap, E_G , which is full of forbidden electronic states. The energy difference between the vacuum level and the conduction band edge of the semiconductor is known as the electron affinity of the semiconductor, and is denoted by $q\chi$. The energy difference between the conduction band edge and the semiconductor Fermi level in the semiconductor bulk is given by $q\phi_n$, and the Metal Work function, $q\phi_m$, is given by the energy difference between the vacuum level and the metal Fermi level. Because the semiconductor Fermi level is closer to the conduction band edge than the valence band edge, the semiconductor shown in Figure 5.2 is n-type. In addition, there are more electrons at higher energies in the semiconductor than the metal because the semiconductor Fermi level is larger than the metal Fermi level. Consequently, as the metal and semiconductor are brought together, the higher energy electrons in the semiconductor will tend to diffuse to the metal until the Fermi levels align and the device reaches thermal equilibrium. As the electrons move from the semiconductor to the metal, the surface of the semiconductor becomes devoid of mobile charge carriers, creating a positively charged depletion region of ionized donors, and therefore becomes less n-type at the interface. The equilibrium condition is shown in

Figure 5.2 (b), where the energy bands of the semiconductor are bent at the interface such that the Fermi level at the semiconductor interface is further from E_C than it is in the semiconductor bulk (less n-type at the interface). For the equilibrium condition, any electrons moving from the metal to the semiconductor see a barrier height of $q\phi_{B0}$. In the ideal case the barrier height is given by the Schottky-Mott limit:

$$q\phi_{B0} = q\phi_m - q\chi \quad (5.1)$$

From equation (5.1) it can be seen that the barrier height is not a function of the applied bias, but rather it is only dependent on the material properties of the metal and the semiconductor. In equilibrium, electrons moving from the semiconductor to the metal see a built-in potential of $q\psi_{bi}$ which is given by:

$$q\psi_{bi} = q\phi_{B0} - q\phi_n = q\phi_{B0} - kT \ln \left(\frac{N_C}{N_d} \right) \quad (5.2)$$

where k is the Boltzmann constant, T is the temperature in Kelvin, q is the elementary charge, N_C is the effective density of states at the conduction band edge of the semiconductor, and N_d is the dopant concentration in the semiconductor. The built-in potential can be decreased by applying a positive bias to the Schottky contact (forward bias operation) or increased by applying a negative bias to the gate (reverse bias operation). In the forward bias mode the electric field resulting from the applied bias opposes the built-in potential and enables the flow of electrons from the semiconductor to the metal. In the reverse bias mode the electric field resulting from the applied bias enhances the built in potential which makes it more difficult for electrons to move from

the semiconductor to the metal. In both modes the Schottky barrier height remains constant and serves to minimize the portion of the leakage current arising from electrons moving from the metal to the semiconductor.

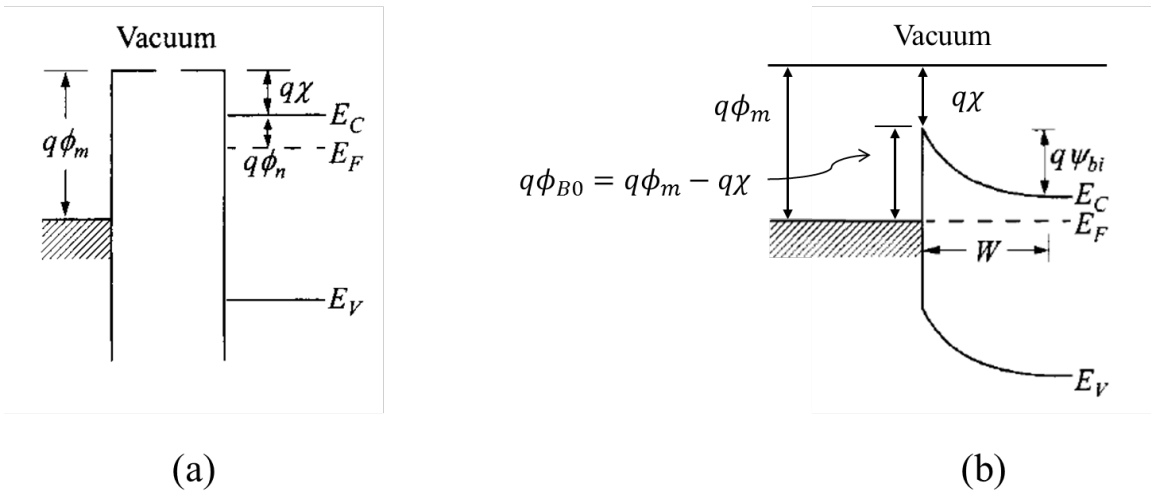


Figure 5.2: Band diagrams of (a) metal and semiconductor separated and (b) after coming together to form a Schottky diode. Adapted from [74].

For moderately doped diodes operating around room temperature the dominant conduction mechanism will be thermionic emission of electrons over the reduced built-in potential from the semiconductor to the metal (forward bias) and thermionic emission of electrons over the Schottky barrier from the metal to the semiconductor (reverse bias). A first order approximation of the current density in a Schottky diode based on the thermionic emission model is known as the Richardson-Dushman equation and is given by:

$$J = A^* T^2 \exp\left(\frac{-q\phi_{B0}}{kT}\right) \left[\exp\left(\frac{qV}{kT}\right) - 1 \right] = J_S \left[\exp\left(\frac{qV}{kT}\right) - 1 \right] \quad (5.3)$$

where A^* is the Richardson constant, V is the bias applied to the diode, J_S is the reverse saturation current density, and all other variables have the same meaning as given previously. It is assumed that the Schottky barrier height is much larger than kT , such that not many electrons in the metal will have sufficient energy to surmount the barrier and move in to the semiconductor; however, the “ -1 ” term in equation (5.3) indicates that there are some energetic electrons that are able to overcome the barrier and create a small reverse current.

The electrons that migrate from the semiconductor to the metal during the initial contact formation create a uniform charge sheet at the metal surface which has a charge equal in magnitude but opposite in sign to the charge of the ionized dopants in the semiconductor depletion region. In essence, the Schottky diode can be treated like a one-sided p-n junction. Using the depletion approximation and assuming uniform doping in the semiconductor the depletion width can be written as:

$$W_D = \sqrt{\frac{2\epsilon_0\epsilon_s(\psi_{bi}-V)}{qN_d}} \quad (5.4)$$

where ϵ_0 is the permittivity of free space, ϵ_s is the relative permittivity of the semiconductor, and all other variables have the same meaning as given previously. The capacitance per unit area of the depletion region can be calculated by modeling the diode as a parallel plate capacitor with a plate spacing equal to the depletion width:

$$C'_D = \frac{\epsilon_0\epsilon_s}{W_D} = \frac{q\epsilon_0\epsilon_s N_d}{\sqrt{2(\psi_{bi}-V)}} \quad (5.5)$$

In Section 5.1.3 it will be shown how the current-voltage characteristics [equation (5.3)] and the capacitance-voltage characteristics [equation (5.5)] of the Schottky diode can be utilized to extract key Schottky diode parameters.

5.1.2 Second Order Considerations

There are actually several other conduction mechanisms that are occurring in a Schottky diode in addition to thermionic emission, and these mechanisms are illustrated in Figure 5.3. As mentioned previously, thermionic emission will dominate for moderately doped semiconductors around room temperature, but as the doping level increases (on the order of 10^{18} cm⁻³ or greater) and/or as the temperature decreases the tunneling current will begin to dominate. As can be seen from equation (5.4) the depletion width in the semiconductor will decrease as the dopant concentration is increased, and a thinner depletion width means a shorter path for electrons to tunnel through, which increases the tunneling probability. This principle is used to create non-

rectifying Ohmic contacts. The tunneling current can actually be decomposed into two constituent parts as well: (1) field emission; which is a pure tunneling current near the Fermi level where the electrons tunnel through the entire width of the barrier and (2) thermionic-field emission; where energetic electrons with insufficient energy to surmount the barrier tunnel through a thinner region of the barrier (mechanism (2) in Figure 5.3). In addition to the current mechanisms shown in Figure 5.3, there is also an edge leakage current which exists around the edge of the contact. Edge leakage can be reduced by implementing more complicated Schottky diode structures such as a guard ring.

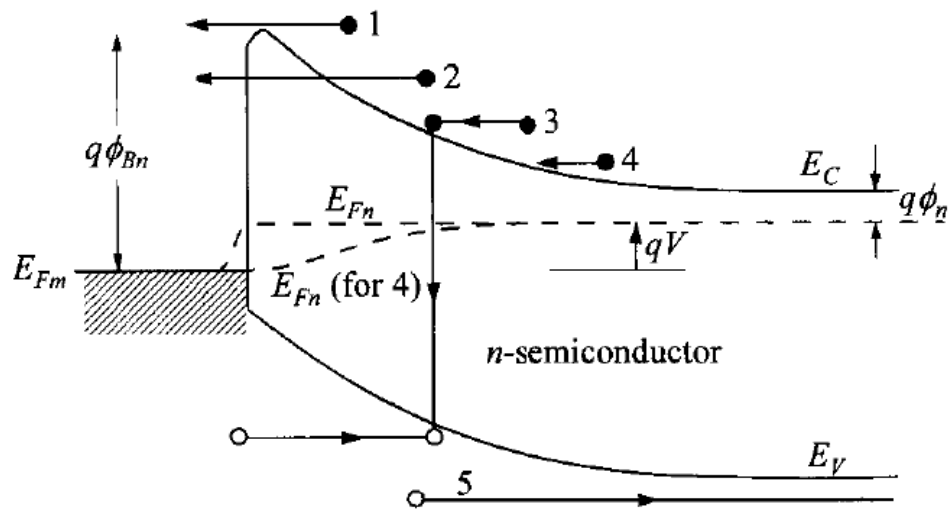


Figure 5.3: Various conduction mechanisms in a Schottky diode: (1) thermionic emission, (2) tunneling, (3) recombination in the depletion region, (4) diffusion of electrons, and (5) diffusion of holes (recombination in the bulk). From [74].

In the ideal case it was assumed that the metal and semiconductor were in direct contact with one another, but in practice there will typically be a thin (on the order of Angstroms) interfacial oxide layer between the Schottky contact and the semiconductor substrate. The interfacial layer is generally thin enough that it is transparent to electrons (i.e. the electrons tunnel through it), but the thin layer can have a potential across it. More importantly, the interfacial oxide introduces interface traps at the oxide/semiconductor interface which allow electrons to exist in the forbidden energy gap of the semiconductor. The interface traps can act as recombination centers for electrons and holes, thereby introducing another conduction mechanism to those illustrated in Figure 5.3 and discussed previously. For a large density of interface traps the Fermi level becomes pinned at a set position in the semiconductor bandgap at the interface because any change in charge on the metal can be compensated for by populating or depopulating interface traps; there is no need for the depletion width to change, and consequently the Fermi level at the interface does not move. For the theoretical case of an infinite number of interface traps it can be shown that the barrier height is independent of the metal work function [74]:

$$q\phi_{B0} = E_g - q\phi_0 \quad (5.6)$$

where E_g is the bandgap of the semiconductor and $q\phi_0$ is the neutral level, which demarcates between acceptor and donor type interface states and is typically one-third of the bandgap above the valance band edge [74]. Above the neutral level the interface states are acceptor type (neutral when empty and negatively charged when occupied), and below the neutral level the interface states are donor type (neutral when occupied and

positively charged when empty). Equation (5.6) is referred to as the Bardeen limit. In practice the barrier height is highly dependent on the surface cleaning and preparation of the semiconductor and will be somewhere between the Schottky-Mott limit and the Bardeen limit.

In order to account for the generalized effect of the various conduction current mechanisms, equation (5.3) can be slightly modified, and is written as:

$$J = A^*T^2 \exp\left(\frac{-q\phi_{B0}}{kT}\right) \left[\exp\left(\frac{qV}{\eta kT}\right) - 1 \right] = J_S \left[\exp\left(\frac{qV}{\eta kT}\right) - 1 \right] \quad (5.7)$$

where η is the ideality factor. In the ideal case of pure thermionic emission and no interface states the ideality factor is unity (Schottky-Mott limit), but if the effects introduced by interface states dominate then $\eta = 2$ (Bardeen limit). As second and third order effects begin to become non-negligible it is possible for the ideality factor to increase above the value of 2 associated with the Bardeen limit. Good diodes typically have values of ideality factor between one and two, but it is possible for the value of η to increase up to 5 or higher for poor quality diodes.

The last non-ideal effect to be considered is Schottky-barrier lowering. As an electron is moving from the semiconductor to the metal it will create a positive image charge in the metal that will exert an image force on the electron which pulls it towards the metal. This effectively lowers the barrier as shown in Figure 5.4. The adjusted barrier height after taking into account the Schottky-barrier lowering is given by:

$$q\phi_B = q\phi_{B0} - q\Delta\phi \quad (5.8)$$

where $q\phi_{B0}$ is the ideal barrier height and $q\Delta\phi$ is the amount of barrier lowering induced by the image force, which is given as:

$$q\Delta\phi = \sqrt[4]{\frac{q^3 N_d (\psi_{bi} - V)}{8\pi^2 \epsilon_0^3 \epsilon_s^3}} \quad (5.9)$$

where in equation (5.9) all variables have the same meanings as described previously. From inspection of equation (5.9) and Figure 5.4 it can be seen that the amount of barrier lowering is dependent on the bias applied to the diode. In order to obtain a more accurate current-voltage relationship equation (5.8) can be substituted into equation (5.7) which results in:

$$J = A^* T^2 \exp\left(\frac{-q(\phi_{B0} - \Delta\phi)}{kT}\right) \left[\exp\left(\frac{qV}{\eta kT}\right) - 1 \right] = J_s \left[\exp\left(\frac{qV}{\eta kT}\right) - 1 \right] \quad (5.10)$$

However, because the barrier lowering in most diodes is typically quite small, the effects can be neglected without much loss of accuracy.

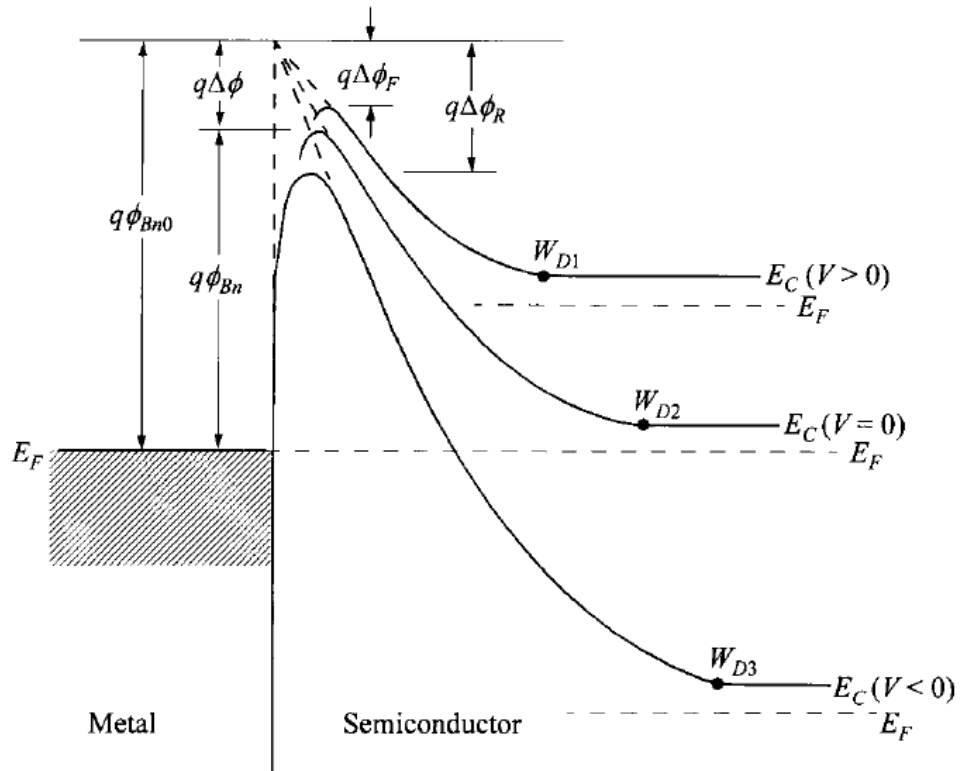


Figure 5.4: Schottky-barrier lowering due to the image force between an electron in the semiconductor and a positive image charge in the metal. Also shown is the qualitative change in barrier lowering for forward and reverse biases. From [74].

5.1.3 Parameter Extraction

Schottky Barrier height, ideality factor, and dopant concentration in the depletion region are all useful metrics for determining the quality of a Schottky diode, and in addition to providing details about initial diode quality, these parameters can also serve as useful markers for changes introduced to the devices during and after exposure to radiation. As detailed below, the I-V data can be used to extract the barrier height and ideality factor, while the C-V data can be used to extract the barrier height and the dopant concentration. Typically, the barrier height extracted from the C-V data will give a slight overestimation of the value, whereas barrier height extracted from the I-V data will give a slight underestimation of the value. This is primarily because the I-V measurements cause some lowering of the Schottky barrier as discussed in Section 5.1.2, whereas the C-V measurements use the flatband condition where there is no Schottky barrier lowering [79]. Therefore, it is common for researchers to take the average of the barrier heights extracted with I-V and C-V measurements in order to get a more accurate estimation of the Schottky barrier height.

As can be seen in equation (5.7) there is an exponential relationship between the diode current density and the applied bias. Therefore, plotting the current density as a function of voltage on a semi-log scale should result in a linear region.

$$\log(J) = \log\left(J_S \left[\exp\left(\frac{qV}{\eta kT}\right)\right]\right) = \left(\frac{q}{\eta kT}\right)V + \log(J_S) \quad (5.11)$$

In equation (5.11) the “-1” term has been omitted, because for standard forward biases $V \gg \frac{kT}{q}$, and the exponential term dominates. Observation of equation (5.11) reveals that it is in standard point-slope form. This indicates that the slope of the semi-log

plot in the linear region can be used to calculate the ideality factor since q , k , and T are all constants. Extrapolating the linear region of the semi-log plot back to the y-axis results in the determination of the reverse saturation current density, J_S , from which the barrier height can be calculated.

Equation (5.5), which gives the capacitance of the depletion region, can also be adjusted so that it is in point-slope form:

$$\left(\frac{1}{C_d}\right)^2 = \left(\frac{2}{q\epsilon_0\epsilon_S N_d}\right)V_R + \left(\frac{2\psi_{bi}}{q\epsilon_0\epsilon_S N_d}\right) \quad (5.12)$$

where V_R is the value of the reverse voltage applied to the diode and all other parameters have the same meanings given previously. Inspection of the characteristic equation of (5.12) reveals that the measurement of diode capacitance versus voltage can be plotted as

$\left(\frac{1}{C_d}\right)^2$ versus V_R to yield a straight line. The slope of this line can be used to determine the dopant concentration, which can in turn be used to calculate the resistivity. The built-in potential, ψ_{bi} , can be found by extrapolating the linear region of the curve to either the x-axis or the y-axis. A precise expression for the barrier height, therefore, can be written as:

$$\phi_{B0} = \psi_{bi} + \phi_n + \frac{kT}{q} - \Delta\phi \quad (5.13)$$

where the $\frac{kT}{q}$ term is a correction factor for the high energy electron tail and the $\Delta\phi$ corresponds to the Schottky-barrier lowering effect. The high energy electron tail, or Debye tail, is a result of the depletion approximation not being entirely accurate. In reality there are some mobile charge carriers just inside the edge of the depletion region, and there is an electric field that extends slightly outside of the depletion region.

5.2 EXPERIMENTAL PROCEDURE

5.2.1 Device Fabrication

Two phosphorous doped silicon wafers with <111> orientation, 2 inch diameter, and resistivity between 3.4 and 4.6 Ω -cm were used in this experiment. The wafers were individually cleaned following a standard RCA procedure. First the wafers were submerged in an ammonium hydroxide/hydrogen peroxide solution for five minutes to remove organic particulates. The wafers were then submerged in two successive deionized (DI) water baths before being submerged in a 2% hydrofluoric (HF) acid solution for three minutes to remove any oxide on the silicon surface. This was also followed by two successive DI water baths. The entire process was repeated a second time and followed by one additional DI water bath before the wafers were blown dry with nitrogen. The wafers were immediately placed in a thermal evaporator and thick ($\sim 1 \mu\text{m}$) backside aluminum Ohmic contacts were deposited. The backside contact deposition was not followed by a thermal annealing step because doing so resulted in the degradation of the quality of the Ohmic contacts for these wafers. The wafers were loaded into the thermal evaporator once more, and several frontside silver Schottky contacts were deposited through a shadow mask. The contacts were circular with a diameter of approximately 6 mm. On one wafer the Schottky contacts were thick ($\sim 360 \text{ nm}$), and on the second wafer the Schottky contacts were thin ($\sim 26 \text{ nm}$). The thicknesses were measured with a Dektak profilometer. The wafers were then stored in standard wafer carriers, and individual Schottky diodes were cleaved from the wafers as needed. After cleaving, the size of a sample containing a single diode was approximately 1 cm x 1 cm.

5.2.2 Na⁺ Irradiation

The Na⁺ ion irradiation of the Schottky diodes was performed with the singly charged beamline at Clemson University [98]. The Schottky diodes were mounted on a stainless steel platen using conductive Ag paint as shown in Figure 5.5 prior to being loaded into the ion beam target chamber. The platen had metal posts which were isolated from the platen base by insulating layers. These posts allowed for in-situ measurements of the diodes. Details of the mounting procedure can be found in appendix D.9. The base pressure in the ion beam system during irradiations was on the order of 10^{-7} Torr. No external bias was applied to the samples during irradiation except when in-situ I-V sweeps were being performed as described below in Section 5.2.3. In total, eight samples were irradiated with the Na⁺ ion beam. For each of the following energy levels there were two Schottky diode samples irradiated, one with a thick Schottky contact and one with a thin Schottky contact: 0.5 keV, 1.0 keV, 1.5 keV, and 2.0 keV. The ion beams were initially tuned in a Faraday cup in the same plane as the sample. Once the ion beam current was maximized, the Schottky diode was translated into the beamline and irradiated for a cumulative time of 90 minutes. Every 30 minutes the beam current was verified by measuring the instantaneous current seen on the Schottky diode. The exact characteristics of the ion beam could not be determined, but it is estimated that the beam is Gaussian in nature with a full width at half maximum (FWHM) of approximately 1.5 cm, such that the beam is wholly incident on the Schottky contact.

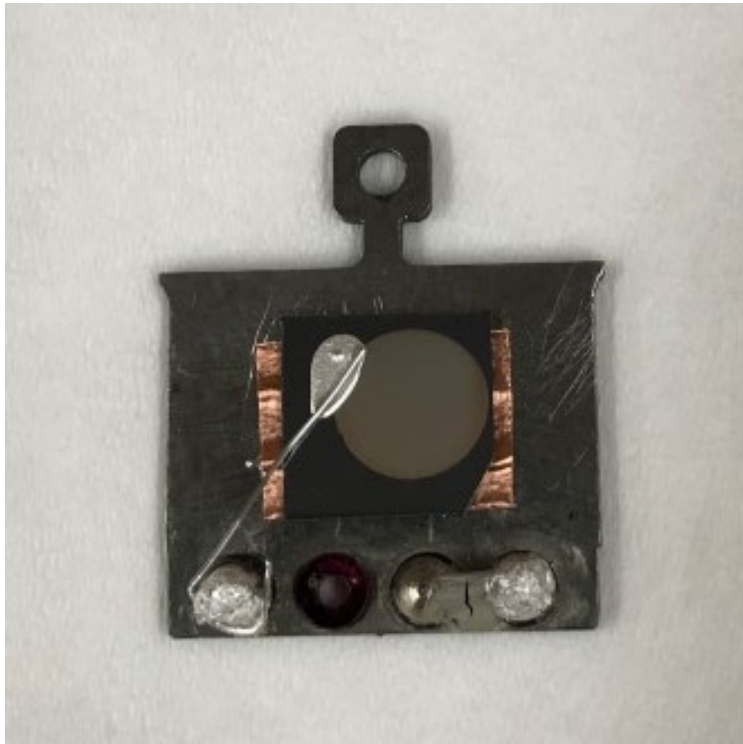


Figure 5.5: Schottky diode mounted on stainless steel platen using Ag paint.

5.2.3 Device Characterization

Prior to being mounted on the stainless steel platen, I-V measurements using a Keithley 4200 semiconductor characterization system and C-V measurements using an Agilent E4980A LCR meter were performed on each of the Schottky diodes. For these pre-irradiation measurements the diodes were placed in a probe station which shielded the sample from light, vibration, and electromagnetic interference. The sample was held in place with a vacuum chuck, and micromanipulator controlled probe tips were used to make electrical contact to the devices. After the diodes were mounted on the platen and loaded into the singly charged beamline, a Keithley 2400 source meter was used to perform in-situ I-V sweeps on the diodes at various times during the irradiation procedure. A Keithley 617 electrometer was used to monitor the instantaneous currents on the Faraday cup and the Schottky diode. After the irradiations were complete, the diodes were removed from the stainless steel platen and post-irradiation I-V and C-V measurements were performed in the same manner as the pre-irradiation measurements.

Pre-irradiation in-situ I-V sweeps were performed prior to turning the ion beam on. After turning the ion beam on and maximizing the current in the Faraday cup, the Schottky diode was translated into the ion beamline and an instantaneous current reading was recorded with the Keithley 617 for the purpose of calculating ion fluence. I-V sweeps were immediately performed with the beam incident on the Schottky diode, and then the ion beam was turned off and more I-V sweeps were performed. This first set of beam on-beam off measurements was performed in order to investigate the kine-current, i.e. any instantaneous effect created in the I-V characteristics by the ion beam. The

Schottky diode was then irradiated by the ion beam in 10 minute intervals, with the ion beam being turned off after each interval so that I-V sweeps could be performed in order to track the radiation damage. The instantaneous beam current, as measured by the Keithley 617 on the diode, was monitored every 30 minutes in order to ensure stability of the ion beam. A detailed process flow for in-situ measurements performed on each diode during irradiation is displayed in Figure 5.6.

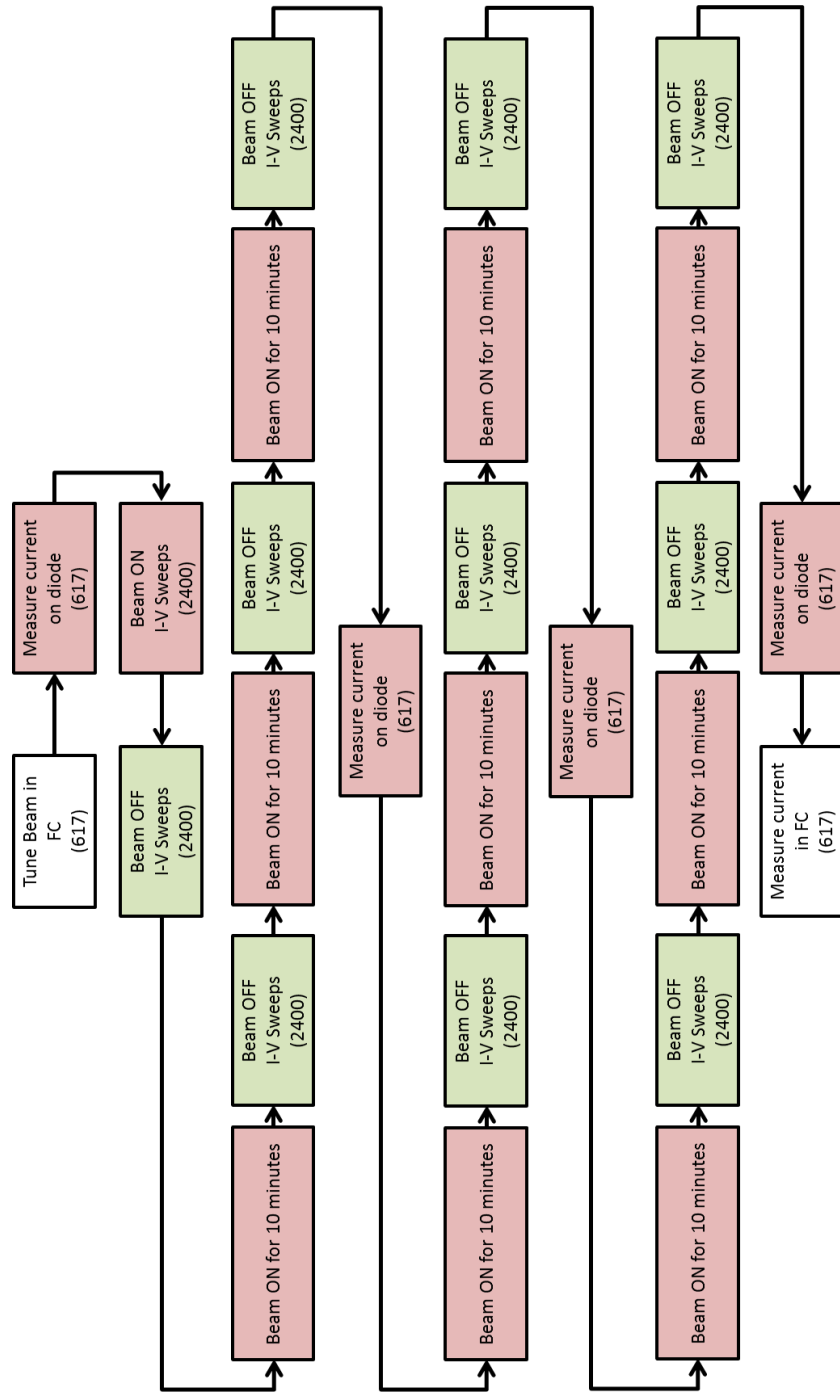


Figure 5.6: Process flow for irradiation of Schottky diodes. Red boxes indicate times when the ion beam is incident on the diode and green boxes indicate times when the ion beam is off. (617) and (2400) indicate measurements are taken with the Keithley 617 and Keithley 2400, respectively. FC = Faraday Cup.

5.3 KINE-CURRENT

The primary goal of this diode work was the detection of a kine-current arising from the hot electrons surmounting the Schottky barrier after being excited by the incident Na^+ ions. As previously stated, the measurements related to kine-current detection were performed at the very beginning of the radiation routine so that radiation damage would be at an absolute minimum. Typically, diode radiation detectors are operated in the reverse biased region. As mentioned in Chapter 2, this is done in order to maximize the size of the depletion region which serves as the active area for radiation detection; however, with slow ions that cannot penetrate into the semiconductor, the size of the depletion region is irrelevant. For this reason we decided to perform high resolution I-V sweeps (0.01 V step) while the diode is under irradiation in order to investigate possible effects in all modes of diode operation. First, I-V sweeps were performed while the Na^+ beam was incident on the diode, and then the Na^+ beam was turned off and more I-V sweeps were performed. By comparing the I-V sweeps with the beam on and the beam off, it is possible to isolate any instantaneous effects arising from the Na^+ beam.

In order to confidently relate any changes observed in the I-V data to a kine-current, it is crucial to understand the approximate range of the ions and excited electrons in the sample. The range and straggle of the Na^+ ions for the various beam energies were determined using the SRIM simulation software [90] and the results are recorded in Table 5.1. As can be seen in Table 5.1, the ion ranges are on the order of a couple of nanometers for all energies considered in this experiment.

Beam Energy [keV]	Na ⁺ Range [nm]	Na ⁺ Straggle [nm]	Max. Electron Energy [eV]	# Electrons Created per Ion	Electron Range [nm]
0.5	1.7	1.0	1.08	463	20.2
1.0	2.5	1.5	1.55	645	14.1
1.5	3.1	1.9	1.92	781	11.5
2.0	3.7	2.2	2.25	889	9.8

Table 5.1: Ion range, standard deviation (straggle) for ion range [90], maximum electron energy [99], minimum number of electrons created per ion, and a rough approximation of electron range [101] for the Na⁺ beam energies used.

In order to determine the approximate range of the electrons excited by the Na⁺ ions, it is necessary to first calculate the approximate kinetic energy of the electrons. Through consideration of the principles of conservation of momentum and conservation of energy, the maximum kinetic energy of an electron in a target material excited by a slow ion is given by:

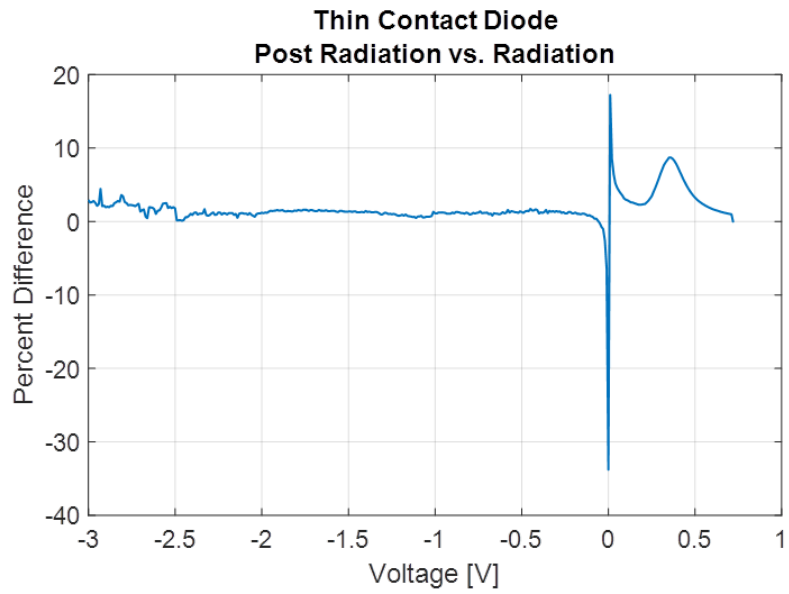
$$E_{max} = 2m_e v_{ion}(v_{ion} + v_F) \quad (5.14)$$

where m_e is the rest mass of an electron, v_{ion} is the velocity of the incident ion, and v_F is the Fermi velocity of the target material [99]. The maximum electron energies shown in Table 5.1 were calculated using the value of 1.4×10^8 cm/s for the Fermi velocity in Ag [100]. Dividing the energy of the incident ion by the maximum energy of the resultant excited electrons gives a minimum number of excited electrons produced per ion as reported in Table 5.1. The maximum electron energies were also used with calculation methods described by Wilson and Dennison [101] to determine an approximation of the electron ranges, which are also shown in Table 5.1. It should be noted that although Wilson and Dennison claim their composite electron range function is valid for energies

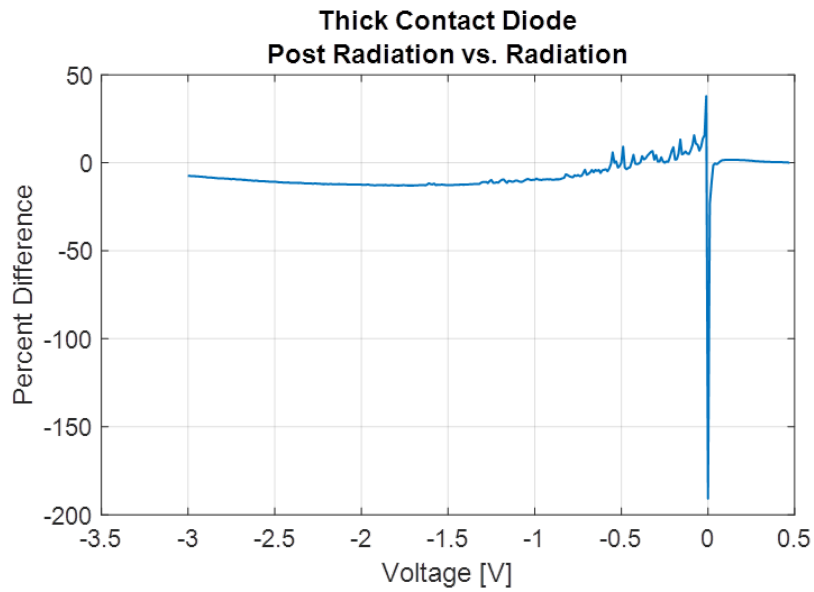
<10eV to >10 MeV, it is possible that the electron energies in our experiments are low enough to cause a greater margin of error. Nienhaus et. al have reported that electrons with energies between 0.5 eV and 2.5 eV typically have mean free paths on the order of 10 nm in Ag and Cu [20]. Considering the work of Nienhaus and calculations based on the model proposed by Wilson & Dennison, a rough approximation of the range of our excited electrons can be expected to be on the order of tens of nanometers in the Ag Schottky contact. This analysis of electron and ion ranges in Ag was the driving factor in using Schottky diodes with two different contact thicknesses. It was expected that some non-negligible portion of the excited electrons created in the thinner contact diodes (~26 nm contact thickness) would reach the semiconductor where they would be recorded as a current. Conversely, essentially all of the electrons excited in the thicker contact diodes (~360 nm contact thickness) were expected to recombine long before being able to reach the metal/semiconductor interface. Therefore, while the diodes are under irradiation by the Na⁺ beam, any change in the signal of the thin contact devices that is not also observed in the thick contact devices can be interpreted as a kine-current.

The percent difference between I-V sweeps taken with the ion beam incident on the diode and with the ion beam off was calculated at each point along the I-V curve in order to investigate the kine-current. Plots of percent difference for devices irradiated with a 1.5 keV Na⁺ beam are shown in Figure 5.7. From Figure 5.7 (a), it can be seen that the most significant percent change in the I-V characteristics occurs around zero volts for the thin Schottky contact diode; however, it can be seen in Figure 5.7 (b) that the same is true for the thick Schottky contact diode. The zero voltage point is most likely the

optimal condition for detecting the kine-current due to the reduced noise in the device, but the fact that similar changes at zero are occurring in both the thick and thin contact devices indicates that these changes do not indicate the presence of a significant kine-current. Closer inspection of the curves in Figure 5.7 reveals that there is a larger percent change for the thick contact device at zero applied bias compared to the thin contact device. Although similar shapes of the percent change curves with peaks around zero were seen for other beam energies, the trend of higher percent change for the thick contact devices was not consistent. Because of this, and the fact that the current levels around zero applied bias are on the order of a few nano-Amps, these changes are most likely due to a limitation in the resolution of the measurement equipment.



(a)



(b)

Figure 5.7: Percent differences between diode I-V sweeps with a 1.5 keV Na^+ beam incident on the diodes and with the Na^+ beam turned off for (a) a thin Schottky contact device and (b) a thick Schottky contact device

There are a couple different factors that might have contributed to our inability to observe a kine-current in the diodes while they were under irradiation. The first factor to consider is that the electrons are being emitted from the surface of the Ag into vacuum instead of moving through the Ag towards the Si substrate. From [102] the threshold velocity of the incident ion required for the emission of electrons from the surface can be calculated as:

$$v_{th} = \frac{1}{2} v_F \left[\left(1 + \frac{\phi_m}{E_F} \right)^{1/2} - 1 \right] \quad (5.15)$$

where E_F is the Fermi energy of the metal contact and all other variables have the same meaning described previously. Using values of 1.4×10^6 m/s, 4.26 eV, and 5.5 eV for the Fermi velocity of Ag, metal work function of Ag, and Fermi energy of Ag, respectively [74, 100, 103], results in a threshold velocity of approximately 2.3×10^5 m/s. For a Na^+ ion beam, this threshold velocity corresponds to a beam energy of approximately 6.5 keV. Because our beam energies were well below this threshold value, it can safely be assumed that none of the signal electrons excited by the incident ions were lost via emission to vacuum.

The second factor that might have led to our inability to measure a kine-current is an insufficient signal to noise ratio. Because the reverse leakage currents of the diodes were relatively high, in the micro-Amp range, this factor seems to be the most likely culprit in the lack of kine-current observation. There are several avenues for reducing the background noise in the diodes for future experiments in order to have a better chance at detecting a kine-current. By performing the experiments at lower temperatures, the reverse leakage current can be reduced by suppression of thermally generated charged

carriers. More advanced device structures, such as guard rings, can also be implemented to reduce the leakage current. Reducing the diode area could possibly lead to reduced leakage current density by virtue of having a lower probability of defects in the Si substrate being in the active area of the device [1]. These defects in the Si enable leakage current through conduction mechanisms other than thermionic emission. Implementing any combination of the aforementioned changes in future experiments should serve to decrease the reverse leakage current of the diodes and ultimately increase the signal to noise ratio. With the processing tools in our lab we could create Schottky diodes with smaller area contacts; however, fabricating diodes with more advanced structures would not currently be feasible.

5.4 RADIATION TOLERANCE

Another goal of our Schottky diode experiments was to investigate the tolerance of Schottky diodes to irradiation with slow heavy ions. Knowing what type of device degradation occurs in the diodes, and after what level of radiation exposure, is important when developing radiation sensing technology. In order to investigate the radiation tolerance of our Schottky diodes, they were exposed to Na^+ beams with the aforementioned energies for approximately 90 minutes. I-V sweeps were performed in 10 minute intervals, and key parameters were extracted to track changes in the diode characteristics. As shown in Table 5.2, the total dose of Na^+ ions used in these experiments was on the order of 10^{16} ions/cm². These ion doses were large enough to observe changes in the diode characteristics; however, simulations using the SRIM

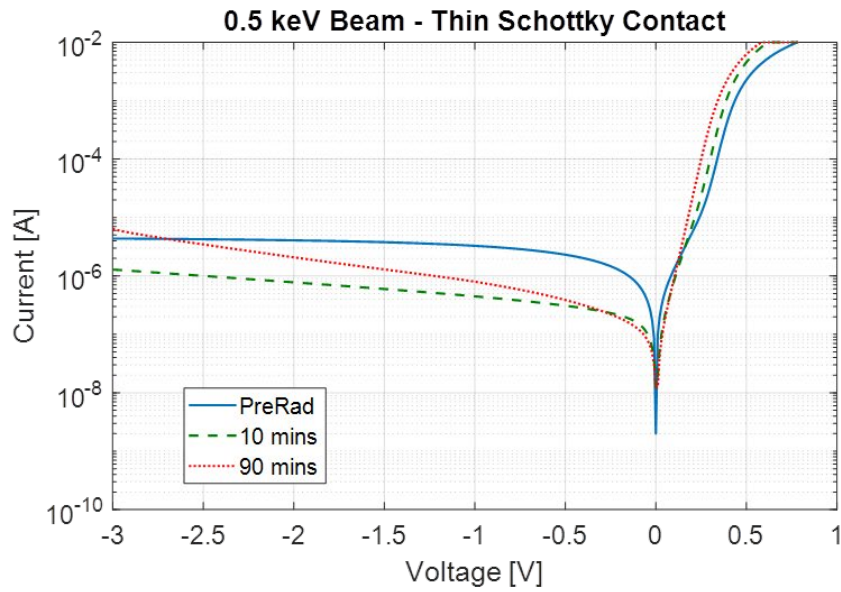
software [90] indicate that the sputtering of Ag atoms is minimal such that there is no significant change to the Schottky contact thickness. This is further confirmed by visual inspection of the diodes after irradiation.

	0.5 keV		1.0 keV		1.5 keV		2.0 keV	
	Thick	Thin	Thick	Thin	Thick	Thin	Thick	Thin
Dose [ions]	4.05E+15	3.88E+15	2.36E+15	2.53E+15	3.71E+15	3.88E+15	5.23E+15	3.88E+15
Dose [ions/cm ²]	1.43E+16	1.37E+16	8.36E+15	8.95E+15	1.31E+16	1.37E+16	1.85E+16	1.37E+16

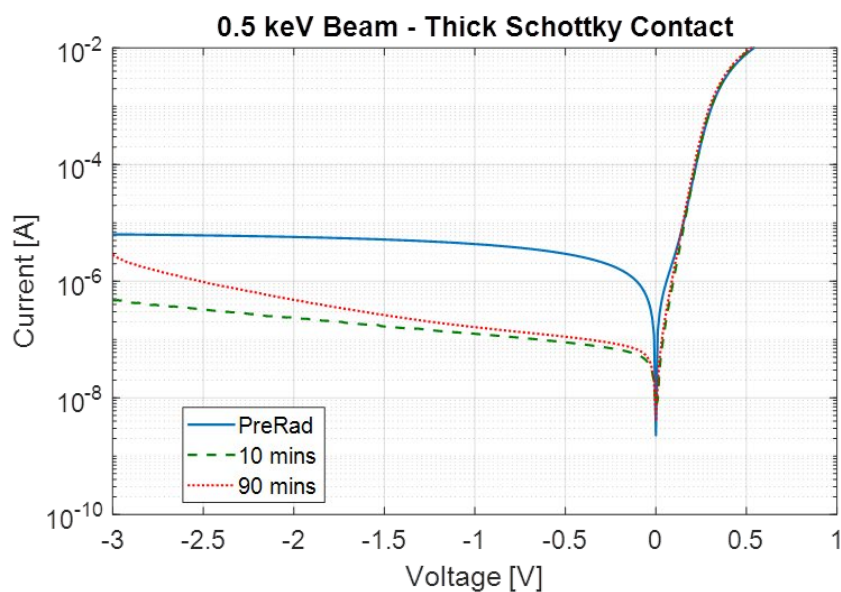
Table 5.2: Total ion doses for all diodes with both thick (~360 nm) and thin (~26 nm) Schottky contacts.

A sample of the effects observed during irradiation of the Schottky diodes is shown in Figures 5.8 and 5.9. In Figure 5.8 we show the in-situ I-V curves for both a thin and a thick contact diode prior to irradiation, after 10 minutes of exposure to a 0.5 keV Na⁺ beam, and after 90 minutes of exposure to a 0.5 keV Na⁺ beam. In Figure 5.9 we show the in-situ I-V curves for both a thin and a thick contact diode prior to irradiation, after 10 minutes of exposure to a 2.0 keV Na⁺ beam, and after 90 minutes of exposure to a 2.0 keV Na⁺ beam. In both figures the most noticeable change to the I-V curves is the reverse leakage current. For all samples, with both thick and thin Schottky contacts, exposed to beam energies less than 2.0 keV, the peak reverse leakage current (at -3 V) showed an initial decrease followed by a near monotonic increase as radiation time increased. At the end of the radiation routine, the peak values of the reverse current were about the same, or slightly larger than, the initial pre irradiation values. This trend is illustrated in Figure 5.8 for both thick and thin Schottky contact devices irradiated at

0.5 keV. However, both samples irradiated with 2.0 keV ion beams showed monotonic increases in reverse leakage currents throughout the radiation routine as shown in Figure 5.9. The initial decrease in leakage current for samples irradiated with energies less than 2.0 keV can most likely be attributed to the creation of trapping centers that reduce the free carrier concentration in the semiconductor, but as the density of interface traps increases the net effect is an increase in defect assisted tunneling between the metal and semiconductor [5, 26, 92, 104].

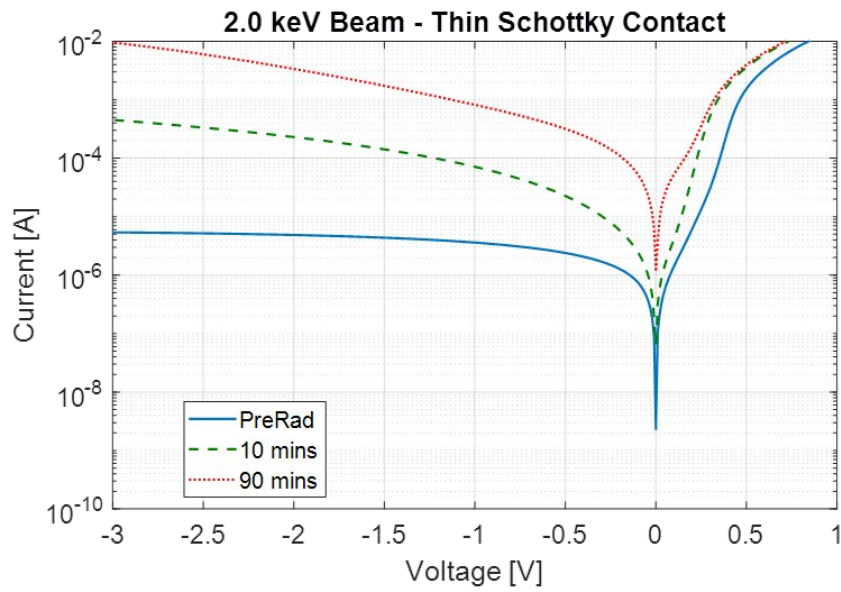


(a)

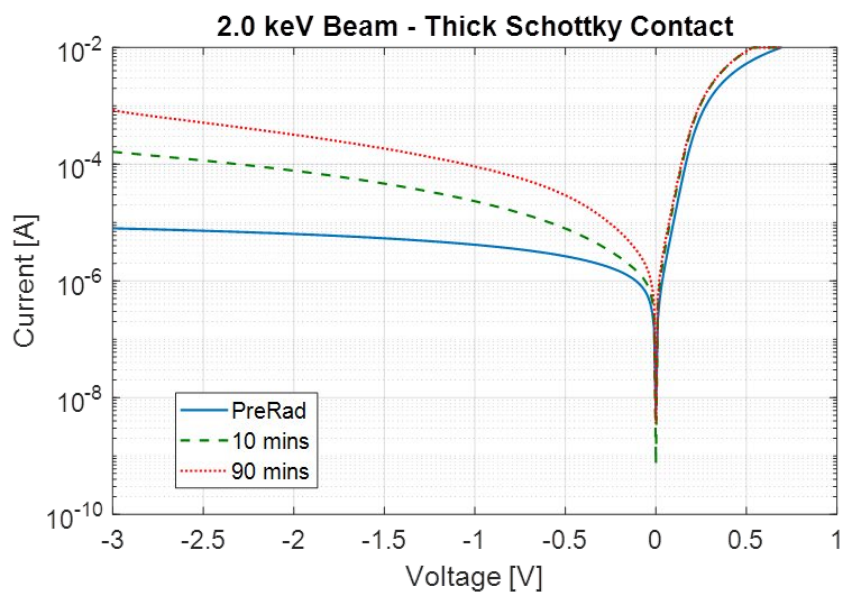


(b)

Figure 5.8: In-situ I-V curves taken prior to 0.5 keV irradiation, after 10 minutes of irradiation, and after 90 minutes of irradiation for (a) a thin Schottky contact device and (b) a thick Schottky contact device.



(a)



(b)

Figure 5.9: In-situ I-V curves taken prior to 2.0 keV irradiation, after 10 minutes of irradiation, and after 90 minutes of irradiation for (a) a thin Schottky contact device and (b) a thick Schottky contact device.

Although not nearly as easy to see in Figure 5.8 and Figure 5.9, there were also noticeable changes to ideality factor and barrier height for all of the diodes. These changes are summarized in Table 5.3, which gives initial values, final values, and percent change for ideality factor and barrier height of all samples. The two samples irradiated at 2.0 keV show an increase in ideality factor and a decrease in barrier height, which is typical for radiation effects reported in the literature [4, 105-108]. However, all other samples irradiated with energies less than 2.0 keV show an overall increase in barrier height and an overall decrease in ideality factor. These trends for the diodes irradiated with energies less than 2.0 keV indicate that the diode properties are improving with irradiation. It is possible that there is some type of annealing effect caused by the irradiation [2, 4]; however, the increase of the peak reverse leakage current seems to somewhat contradict the idea that the diode quality is improving. From Table 5.3, it can also be seen that percent changes were more severe for the thin contact devices than the thick contact devices. This is true for all cases except for the change in barrier height at 0.5 keV irradiation, where the magnitude of change is approximately equal for both the thick and thin Schottky contact diodes. The more severe changes in the thin contact diodes are expected due to the fact that more secondary electrons are able to reach the metal semiconductor interface. It can also be observed from Table 5.3 that the initial value of ideality factor varies between the diodes. Although not ideal, this is not a serious issue since we are primarily focused on changes in the diode parameters.

	0.5 keV		1.0 keV		1.5 keV		2.0 keV	
	Thick	Thin	Thick	Thin	Thick	Thin	Thick	Thin
η_{Pre}	1.68	2.61	1.24	3.61	1.26	4.00	1.19	2.60
η_{Post}	1.01	1.24	1.10	1.10	1.05	1.80	1.28	3.34
% Change η	-39.82%	-52.45%	-11.75%	-69.51%	-16.39%	-55.07%	8.01%	28.57%
$\phi_{B,Pre}$ [eV]	0.78	0.77	0.78	0.76	0.79	0.74	0.77	0.77
$\phi_{B,Post}$ [eV]	0.83	0.83	0.79	0.84	0.79	0.78	0.74	0.67
% Change ϕ_B	6.66%	6.59%	1.28%	9.96%	0.64%	4.57%	-3.79%	-13.21%

Table 5.3: Initial values, final values, and associated percent change for ideality factor and barrier height extracted from in-situ I-V curves for both thick (~360 nm) and thin (~26 nm) Schottky contact diodes.

Considering the Schottky-Mott and Bardeen limits can be useful for trying to reconcile the seemingly contradictory trends in barrier height, ideality factor, and peak reverse leakage current that are observed in the diodes irradiated with beam energies less than 2.0 keV. Using equations (5.1) and (5.6) along with material property values from [74], the Schottky-Mott and Bardeen limits for our thick and thin contact Ag-Si Schottky diodes are calculated as 0.21 eV and 0.82 eV, respectively. From the initial values of barrier height in Table 5.3, it can be seen that the barrier height for the diodes started out between the two limits, but closer to the Bardeen limit. As the devices are irradiated, it is likely that more interface traps are introduced at the metal/semiconductor interface such that the barrier height is trending towards the Bardeen limit due to an increase in the effects of Fermi-level pinning. The introduction of interface traps also agrees with the observed increase in peak reverse leakage currents due to the increase in defect assisted tunneling and defect assisted recombination/generation. The observed decrease in ideality factor seems to be at odds with this proposed rise of conduction mechanisms other than

thermionic emission; however, it is important to keep in mind that the ideality factor also serves as a measure of spatial homogeneity of the Schottky barrier height [8, 79, 109]. Larger ideality factors indicate a higher degree of spatial inhomogeneity of Schottky barrier height, and lower ideality factors indicate better spatial homogeneity. Therefore, it is reasonable to assume that by introducing interface states across the device, the ion irradiation is making the barrier height more spatially homogenous, which in turn leads to a decrease in the ideality factor. The post radiation measurements that were done ex-situ showed the same general trends in all but a couple of instances.

C-V measurements on the Schottky diodes were also performed to provide another independent means of parameter extraction, which is typically presented in the literature on diodes. The trends in Schottky barrier height extracted from the C-V data agreed well with the trends from the in-situ I-V data, but the barrier heights extracted from the C-V data were slightly smaller. The data extracted from the C-V curves also indicated there was a negligible change in dopant concentration, which is to be expected since the ions are not penetrating into the depletion region where they can cause dopant deactivation. Overall, the data from the in-situ measurements gives a better representation of the changes occurring in the diodes than the ex-situ measurements for two reasons. First, the times between the end of irradiation and ex-situ characterization were varied between devices due to scheduling issues and procedural restraints related to cool down time of the ion source in the beam line. In the presence of room temperature annealing [110, 111], having different times between the end of irradiation and post radiation characterization can lead to varying degrees of recovery of the initial changes. Second,

the post radiation, ex-situ measurements were performed after removing the sample from the stainless steel platen. Removing the sample exposes the diode to mechanical stresses that can possibly change device properties.

5.5 SUMMARY AND CONCLUSIONS

In this chapter, the general model and operation of a basic Schottky diode was described. The barrier formation was discussed and the Richardson-Dushman equation for current in the diode arising from thermionic emission was presented. Several second order considerations including Fermi-level pinning and Schottky barrier lowering were also described. Methods for extracting key parameters from I-V and C-V data were also presented.

We have irradiated Schottky diodes with Na^+ beams with energies of 0.5 keV, 1.0 keV, 1.5 keV, and 2.0 keV in order to investigate hot electron current detection and diode radiation tolerance. Diodes of two different thicknesses (~ 26 nm and ~ 360 nm) were irradiated at each energy level, for the purpose of verifying a hot electron signal based on the expected range in the Ag Schottky contact. Unfortunately, no kine-current arising from the hot electrons was detected, but future experiments carried out at lower temperatures and with different device structures might lead to improved results. For energies less than 2.0 keV, diodes with both thick and thin contacts showed an improvement in barrier height and ideality factor while only showing slight degradation in reverse leakage current. This was attributed to the spatially homogenous creation of interface states in the diode. At 2.0 keV the diodes experience degradation in all key

parameters as expected based on previous results in the literature. This work provides a good foundation for future work with Schottky diodes in the EBIT. In this work the Na^+ ions have negligible potential energy, but for the slow highly charged ions produced in the EBIT the potential energy is on par with or greater than the kinetic energy. Knowing how the Schottky diodes respond to the kinetic energy of the Na^+ beams is critical for being able to isolate the effects of the potential energy of the slow highly charged ions.

CHAPTER 6

FUTURE WORK

6.1 MOS CAPACITORS

Chapter 4 of this dissertation reports on the clear charge state dependence of HCI effects observed for irradiated MOS capacitors. Although we are pleased with this initial result, we feel that it is the first of many steps in a larger experiment that will lead to better understanding of HCI/device interaction and ultimately accurate sensors for slow HCIs. Several of the different possible extensions of the work reported in this dissertation are outlined and briefly discussed below.

Perhaps the most obvious experiment that could be performed next would be an irradiation of MOS capacitors with thin metal contacts deposited prior to the irradiation. Although sensors could in theory be constructed such that the bare oxide is exposed for some amount of time before depositing the capacitor gate metal and then taking a reading, such devices would not be practical. Experiments could begin with a very thin top metal contact (~20 nm) deposited prior to irradiation, but the thickness could be increased in order to see how the effects of the HCI irradiation change as the distance between the initial impact and the active region of the capacitor increases.

Another important next step that should be pursued is to repeat the experiments with varied ion beam parameters. The motivation for investigating the various beam parameters at different settings is described in the bullets below.

- By irradiating MOS capacitors with a wider range of charge states it would be possible to gain a better understanding of the charge state dependence of effects observed in the electrical characterization.
- Varying the HCI fluence by adjusting the irradiation time would also be useful. Experimenting in a sample space where the effects of fluence are in a linear regime would avoid the averaging that we were required to perform in order to obtain meaningful results for the data reported previously. Identifying a linear regime without saturation might also lead to more accurate results regarding charge state dependence. The fluence can also be adjusted so that the experiments represent conditions in the real world where HCIs are present. For example, accelerated testing could be performed to investigate what the MOS capacitors would see after a year of exposure to the solar wind.
- Varying the incidence angle of the HCIs on the samples would be useful for decomposing the net observed effects into their constituent parts; the effects due to the kinetic energy of the HCI and the effects due to the potential energy of the HCI. The effects from kinetic energy transfer should vary more drastically as the incidence angle is changed, with more substrate damage at an angle normal to the target and more surface sputtering at grazing angles. The effects resulting from potential energy transfer should not show nearly as much variation with incidence angle; therefore, any device properties that change significantly as the incidence angle is varied can be attributed to the kinetic energy of the HCI, and any device changes that are more or less constant as incidence angle is varied can be

attributed to the potential energy of the HCI. Figure 6.1 provides an example of how different observations can be attributed to the kinetic and potential energies. Sputter yields for Si^+ ions show a strong dependence on incidence angle, consequently this is related to the transfer of the HCI's kinetic energy. Conversely, the proton sputter yields are relatively independent of the incident angle meaning that the proton sputtering is primarily due to the HCI's potential energy [54].

- The kinetic energy of the HCIs could also be varied in order to provide further insight into the role that kinetic energy plays in the observed changes in the MOS capacitors.
- A final parameter that should be adjusted is the ion species. It is important to understand how the devices are going to respond to different species of HCI, because in real world applications the sensors will be operating in environments that contain several different HCI species. As will be discussed later, there should be some type of selection process for which ions are incident on the sensor, but the system should be able to analyze ions of different species and energies as the mechanism of the selection process allows different parts of the ambient radiation to interact with the sensor.

Postmortem analysis of the MOS capacitors after performing all electrical tests could also prove worthwhile. Using some type of microscopy (AFM, STM, and/or SEM) would enable the devices to be inspected for any physical damage on the outermost

layers. Investigating the sputtering of the top metal contacts could be important considering that metal layers would be very thin (tens of nanometers).

Deep level transient spectroscopy (DLTS) could also be useful for a more detailed investigation of the trap levels that are present in the MOS capacitors after being exposed to the HCl irradiation.

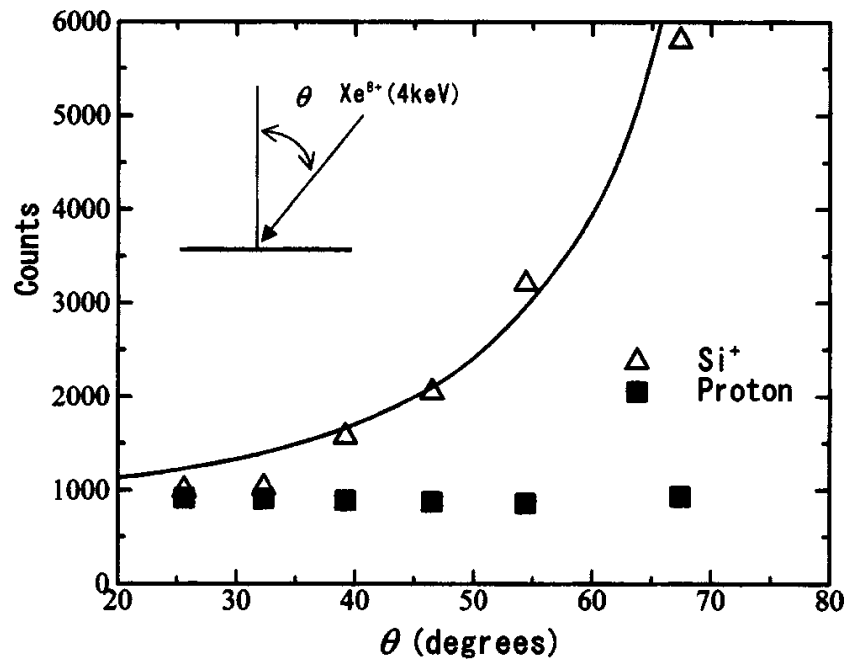


Figure 6.1: Taken from [54]. Sputter yields from a silicon surface irradiated with 4 keV Xe^{8+} at various incidence angles. It can be seen that the Si^+ sputtering was more dependent on the kinetic energy of the HCl, whereas the proton sputtering was dependent on the potential energy and independent of the kinetic energy.

6.2 SCHOTTKY DIODES

As mentioned in Chapter 5, there are several experimental changes that could be made in order to improve the probability of detecting a kine-current in the Schottky diodes exposed to slow, singly charged ion irradiation. The experiments could be carried out at lower temperatures in order to decrease the background noise arising from thermally generated carriers. Schottky contacts with smaller diameters might lead to reduced reverse leakage currents due to a smaller number of defects in the silicon below the Schottky contacts [1]. More advanced diode structures, such as guard rings, might allow further reduction of the reverse leakage currents. Any combination of these approaches should lead to a lower reverse leakage current, and ultimately a higher signal to noise ratio.

Another clear next step for the Schottky diode experiments would be to irradiate devices in the EBIT. Some preliminary experiments with Schottky diodes were performed in the EBIT, but unfortunately the EBIT has been offline for most of the past couple of years due to technical issues. After initial experiments are completed, the parameters of the HCI beam (charge state, fluence, incidence angle, kinetic energy, and ion species) could be varied for the reasons described in the previous section.

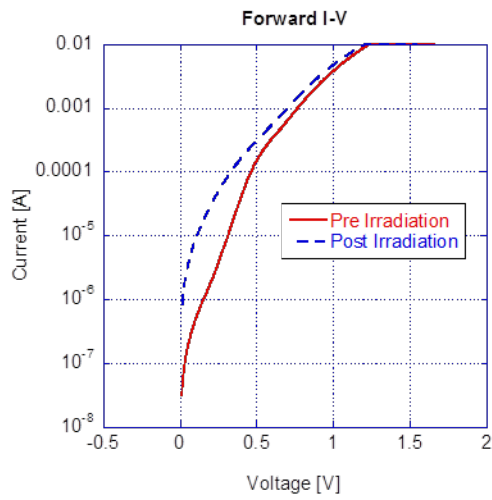
The two diodes irradiated as part of the preliminary EBIT experiment were fabricated on <111> silicon with a phosphorus dopant ($3.4 \text{ } \Omega\text{-cm} < \rho < 4.6 \text{ } \Omega\text{-cm}$). Silver frontside contacts were deposited prior to irradiation and had diameters of 6 mm and approximate thicknesses of 20 nm. Both diodes were irradiated with a 15 keV C^{5+} beam with a fluence of $\sim 10^{13}$ ions/cm². These beam parameters were chosen to approximate

conditions seen in the solar wind [12]. Several sets of I-V measurements were taken prior to irradiation, one set of I-V measurements was taken within two hours of the completion of the irradiation, and several more sets of I-V measurements were taken over the weeks following the irradiation.

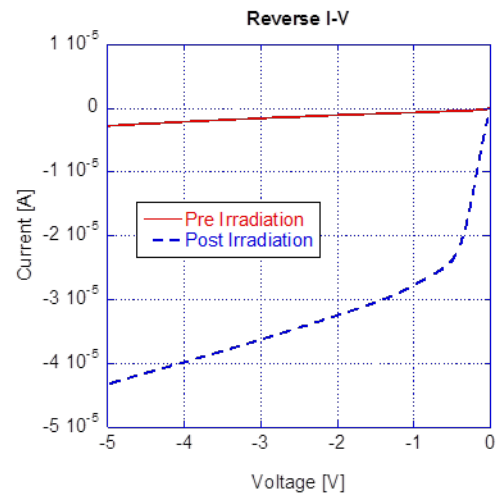
There were notable changes in the characteristics of the two diodes that were irradiated in the EBIT as part of the preliminary experiments; however, the initial quality of one of the diodes was rather questionable ($\eta=3.8$ and reverse leakage on the order of $100 \mu\text{A}$). Accordingly, only the better of the two diodes will be discussed in any detail, but it is worth mentioning that the same general trends were also observed for the poorer quality diode. As can be seen in Figure 6.2 parts (a) and (b), both the forward and reverse current showed an appreciable increase in magnitude after irradiation. Although not shown here, the currents did seem to be trending towards the pre-irradiation values as subsequent I-V measurements were performed over the weeks following the irradiation. The forward I-V curves were used to extract values for the barrier height and the ideality factor of the diode via the procedure described in Chapter 5. Figure 6.2 (c) shows that the barrier height decreased by nearly 16% following HCI irradiation, and then remained somewhat stable at the reduced value. Figure 6.2 (d) shows that the ideality factor increased by approximately 150%, and then remained fairly stable. These results seem to indicate that the HCI irradiation is creating new methods of conduction between the silicon substrate and the Schottky contact. It is likely that defects created at the metal/semiconductor interface are leading to defect-assisted tunneling through the Schottky barrier. It is also possible that the HCIs create defects in the semiconductor

depletion region, subsequently allowing for increased trap-assisted carrier recombination. Both of the two aforementioned processes would lead to an increase in observed current and a change from the dominance of thermionic emission of electrons over the Schottky barrier.

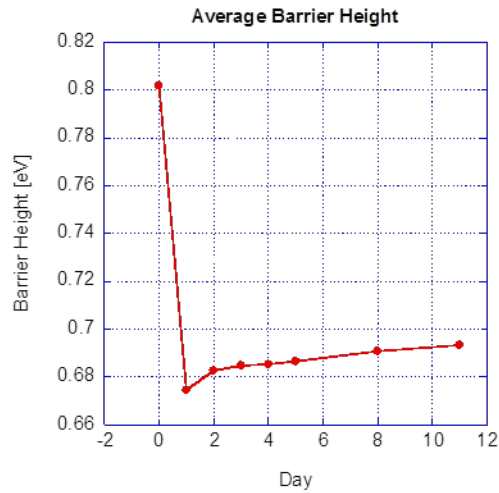
Once the EBIT is back online, more experiments should be performed in to order to better quantify and understand the observed effects. In addition to irradiating single Schottky diodes with 6 mm diameter contacts, it might be worthwhile to attempt several HCI irradiations on samples with an array of smaller Schottky diodes similar to what was used for the MOS experiments described previously in Chapter 4. This could potentially help to improve the initial quality of the diodes [1].



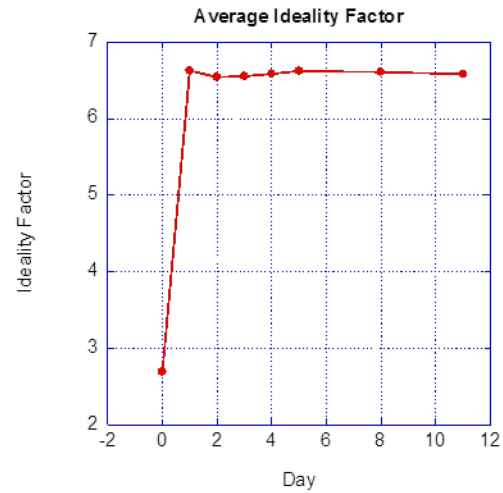
(a)



(b)



(c)



(d)

Figure 6.2: (a) Pre and post irradiation forward I-V curves shown on a semi-log plot. (b) Pre and post irradiation reverse I-V curves. Changes in average barrier height (c) and ideality factor (d) of the Schottky diode. For parts (c) and (d) the **Day** axis can be understood as 0 = preirradiation, 1 = post irradiation; day of irradiation, 2 = day after irradiation, etc.

6.3 PROTOTYPE SLOW HCI SENSOR

The MOS capacitors and Schottky diodes discussed up to this point would only serve as the final stage in a multi-stage radiation sensing device. In order for a slow HCI sensing device to be useful in realistic radiation environments it must be able to isolate the various components that are present, and determine the effects due to each component of the overall radiation. A possible schematic for a slow HCI sensing apparatus is shown below in Figure 6.3, and the purpose of each section of the apparatus will be described below. The goal would be for the sensor to be able to isolate components of a radiation environment based on the ion species, ion kinetic energy, and ion charge state. The basic schematic in Figure 6.3 is able to isolate most components, but there are still some challenges that would need to be overcome as discussed below.

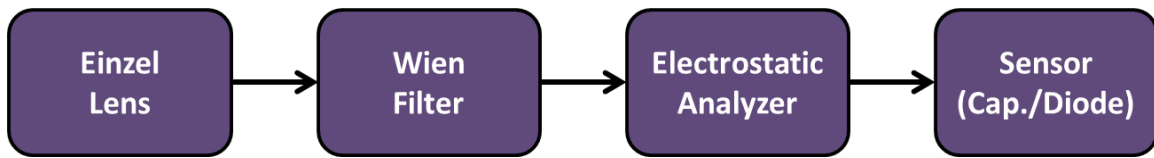


Figure 6.3: Simple schematic for a prototype slow HCI sensing apparatus.

The first stage of the prototype sensor would be an Einzel lens which would collimate the ambient radiation into a beam directed towards the sensor. The second stage would be a Wien filter which would serve as a velocity filter. The Wien filter would consist of an electric field and a magnetic field which are orthogonal to each other and orthogonal to the velocity of the incoming ion beam. The force on the ions due to the electric field is shown in equation (6.1) and the force on the ions due to the magnetic field is shown in equation (6.2).

$$\vec{F}_E = Q\vec{E} \quad (6.1)$$

$$\vec{F}_B = Q\vec{v} \times \vec{B} = Q\vec{v}\vec{B}; \quad \text{since } \vec{v} \text{ and } \vec{B} \text{ are orthogonal} \quad (6.2)$$

where Q is the charge on the ion (i.e. the charge state for an HCl), \vec{E} is the electric field, \vec{B} is the magnetic field, and \vec{v} is the ion velocity. When the force of the electric field acting on an ion is equal to the magnetic field acting on the same ion the two forces essentially cancel out and the ion is able to pass through the Wien filter. Equating the forces from equations (6.1) and (6.2) results in the pass velocity shown in equation (6.3).

$$\vec{v} = \frac{\vec{E}}{\vec{B}} \quad (6.3)$$

As can be seen in equation (6.3) there is no dependence on the ion charge state. The only ion parameter that determines whether or not it passes through the Wien filter is the ion velocity.

The third state of the slow HCl sensing apparatus would be an electrostatic analyzer (ESA). The ESA would consist of an electric field that is applied to the ions that are passed through the Wien filter. The geometry of the ESA would allow ions with a

desired energy to charge ratio $\left(\frac{E}{q}\right)$ to pass through the filter while those ions with different energy to charge ratios would collide with the chamber walls. For nonrelativistic particles the energy of the ions is given by equation (6.4).

$$E = \frac{1}{2}mv^2 \quad (6.4)$$

After passing through the Wien filter all ions would have the same velocity which means that any variation in energy of the ions after the Wien filter are due to differences in mass. So for the particular setup proposed in Figure 6.3 the ESA is filtering based on the mass to charge ratio $\left(\frac{m}{q}\right)$. This type of filter would work fine for a majority of the components in the radiation environment, but an issue arises for degenerate charge states. Degenerate charge states occur when two or more different HCI species have the same charge to mass ratio such as C^{6+} and O^{8+} .

At the moment there is not a completely satisfactory solution to the inability of the apparatus shown in Figure 6.3 to distinguish between different HCIs with the same mass to charge ratios. By tuning the ESA to avoid mass to charge ratios corresponding to degenerate charge states the issue could be avoided, but obviously this comes with the disadvantage of not being able to isolate every component of the radiation environment. It might be possible to allow multiple degenerate charge states through the ESA at once and then deconvolve the effects in the analysis somehow, but more preliminary work performed by varying several of the EBIT beam parameters would be required in order to determine the feasibility of this solution. Another potential solution could be employing an inhomogeneous magnetic field between the ESA and the final sensor to sort

degenerate charge states that have different magnetic moments. This most likely would not work for all cases however.

Another issue that will need to be addressed is the radiation hardness of the final sensing component in the apparatus shown in Figure 6.3. Semiconductor materials that are more radiation hard, such as SiC and GaN, might be instrumental in extending the useful lifetime of the sensor. More sophisticated device structures like guard rings for the Schottky diodes could also be helpful in extending the sensor lifetime. Regardless of the materials and device structure used there will eventually be some degradation to device characteristics, so using some type of annealing to repair the radiation damage between measurements could be key in reducing cost associated with replacing sensors. A rapid thermal annealing processing seems more suitable than a traditional bake given the relatively small size of the sensor and the various extreme environments in which it will operate.

APPENDICES

Appendix A

Publications

Journal Articles

- **D.B. Cutshall**, P. Johnson, J.E. Harriss, C.E. Sosolik, and W.R. Harrell, “Effects of slow Na⁺ Irradiation on Ag-Si Schottky Diodes” *In Preparation*.
- **D.B. Cutshall**, D.D. Kulkarni, J.E. Harriss, D.A. Field, C.E. Sosolik, and W.R. Harrell, “Effects of slow highly charged ion irradiation on metal oxide semiconductor capacitors,” *Journal of Vacuum Science and Technology B*, vol. 36, issue 5, pp. 052901-1:7, July 2018.
- **D.B. Cutshall**, D.D. Kulkarni, A.J. Miller, J.E. Harriss, W.R. Harrell, and C.E. Sosolik, “Tracking ion irradiation effects using buried interface devices,” *Nuclear Instruments and Methods in Physics Research B*, vol. 422, pp. 47-49, May 2018.
- D.D. Kulkarni, D.A. Field, **D.B. Cutshall**, J.E. Harriss, W.R. Harrell, and C.E. Sosolik, “Probing kinetically excited hot electrons using Schottky diodes,” *Journal of Vacuum Science and Technology B*, vol. 35, issue 3, p. 03D103, March 2017.
- D.D. Kulkarni, R.E. Shyam, **D.B. Cutshall**, D.A. Field, J.E. Harriss, W.R. Harrell, and C.E. Sosolik, “Tracking subsurface ion radiation damage with metal-oxide-semiconductor device encapsulation,” *Journal of Materials Research*, vol. 30, no.9, pp. 1413-1421, May 2015.
- M. Savchak, N. Borodinov, R. Burtovyy, M. Anayee, K. Hu, R. Ma, A. Grant, H. Li, **D.B. Cutshall**, Y. Wen, G. Koley, W.R. Harrell, G. Chumanov, V. Tsukruk, and I. Luzinov, “Highly Conductive and Transparent Reduced Graphene Oxide Nanoscale Films via Thermal Conversion of Polymer-Encapsulated Graphene Oxide Sheets,” *ACS Applied Materials & Interfaces*, vol. 10, issue 4, pp. 3975-3985, December 2017.

Conference Papers

- C.E. Sosolik, D.D. Kulkarni, D.A. Field, E.S. Srinadhu, **D.B. Cutshall**, W.R. Harrell, and J.E. Harriss, “Recent results from the ion beam laboratories at Clemson University,” *21st International Workshop on Inelastic Ion-Surface Collisions*, p. 66, October 2015.
- R. Shyam, D.D. Kulkarni, D.A. Field, E.S. Srinadhu, **D.B. Cutshall**, W.R. Harrell, J.E. Harriss, and C.E. Sosolik, “First multicharged ion irradiation results from the CUEBIT facility at Clemson University,” *AIP Proceedings of the XII International Symposium on Electron Beam Ion Sources and Traps*, pp. 129-135, January 2015.
- J.Y. Kim, **D. Cutshall**, T. Hawkins, J. Ballato, and S. Kim, “Long and Highly Flexible Micro-Plasma Jet Device for Endoscopic Treatments,” *APS, 65th Annual Gaseous Electronics Conference*, vol. 57, no. 8, October 2012.

Appendix B

Guides and MATLAB Code for Analysis with MOS Work

B.1 Procedure for Gaussian Analysis

1. Enter the desired data (e.g. V_{FB}) into an Excel spreadsheet in matrix form so as to match the physical distribution of the actual sample. See the file “*Ar1_4.05E12.xlsx*” for an example.
 - a. Note: If there were only one or two bad devices in the matrix Dhruva ‘created’ a value for those bad devices by averaging the values of all adjacent devices.
2. Go to the *HOME* tab in MATLAB and select *Import Data*. Navigate to the appropriate folder, select the desired file and click ‘open’. Along the top ribbon, above *IMPORTED DATA*, select *Matrix*. Click the green check mark above *IMPORT* to import the data to the workspace.
3. Repeat the previous step for all samples that you want to be considered in the analysis.
4. Once all sample data is in the MATLAB Workspace click on *Save Workspace* in the *HOME* tab. Now the workspace can be easily reloaded at a later time as opposed to importing the individual spreadsheets again.
5. Open the file *call_myconvert.m* in MATLAB.
 - a. Select the desired spacing for interpolation (Dhruva typically used 0.1; this means ten points were interpolated between each actual data point both horizontally and vertically).
 - b. For each sample that you are analyzing there should be a line calling the *myconvert* function. Select filenames for the 3 output files (left side of equation), and specify the filename of the input file in the workspace (right side of the equation).
 - c. For more details on the *myconvert.m* file see the comments in the MATLAB code which explain everything.
6. Type *cftool* into the MATLAB command window to open the curve fitting tool
 - a. For *x data*, *y data*, and *z data*, select the first, second, and third outputs from the *myconvert* function respectively.
 - b. In the top center of the *cftool* window there is a drop down menu that defaults to “*Interpolant*”. Change this to “*Custom Equation*” and then in the large text box below paste a copy of the Gaussian equation from the text file “*2dgaussian_function_typed.txt*”.

- c. Click the box that says “*Fit Options...*”, right below where the Gaussian equation was entered. From here you can manually adjust the fit. Dhruva adjusted the lower and upper limits for sigx , sigy , and θ as shown in column N of the first sheet in “*fits_50nm.xlsx*”.
7. Copy the key parameters from the “*Results*” box of the cftool window into an Excel spreadsheet as done in “*fits_50nm.xlsx*”. (Key parameters include A , sigx , sigy , θ , x_0 , and y_0 . You might also want to copy some of the parameters describing the goodness of fit (i.e. R-square, SSE, etc.) in the “*Table of Fits*” window at the bottom of the cftool window.)
 - a. Calculate a , b , and c values from the θ , sigx , and sigy values. (See the second sheet of “*fits_50nm.xlsx*” for conversion equations.
 - b. Create a sheet containing the following variables for each sample: A , x_0 , y_0 , a , b , c , x_{\min} , y_{\min} , x_{\max} , and y_{\max} . Where the min and max for x and y correspond to the min and max for the columns and rows respectively of the original capacitor matrix. Save this sheet as a .txt file for later steps (not entirely sure that transferring this to a text file is necessary... spreadsheet should be fine).
8. Import the data from step 7) b. into MATLAB from either the Excel spreadsheet or the text file. Import using the same procedure from step 2, except select *Column vectors* instead of *Matrix*.
9. Run the code *integration_script.m*, and be sure that the name of your fit parameters that were imported in the previous step match exactly with variables that are the input arguments to the *make_elliptical_gaussian* function that is called within the *integration_script.m*.
 - a. Note: the file *make_elliptical_gaussian.m* should be in the same directory (and possibly open) in order for *integration_script.m* to work properly.
10. Use the output arrays *average_Vfb* (variable name might change if a different parameter is being investigated) and *adjusted_dose* to create a plot of the changes vs. fluence/dose (for HCIs there can be several different data sets for different charge states).

B.2 Code for interpolating data points

call_myconvert_stretchout.m

```
%run this file to call myconvert
%[x,y,z]=myconvert(,spacing)

%Changes the 'resolution' of the interpolated points (DC)
spacing = 0.1

[Ar11_F1x,Ar11_F1y,Ar11_F1z]=myconvert_stretchout(Ar11_F1,spacing)
[Ar11_F2x,Ar11_F2y,Ar11_F2z]=myconvert_stretchout(Ar11_F2,spacing)
[Ar11_F3x,Ar11_F3y,Ar11_F3z]=myconvert_stretchout(Ar11_F3,spacing)

%[Ar1_573E13x,Ar1_573E13y,Ar1_573E13z]=myconvert_stretchout(Ar1_573E13,
spacing)

[Ar4_F1x,Ar4_F1y,Ar4_F1z]=myconvert_stretchout(Ar4_F1,spacing)
[Ar4_F2x,Ar4_F2y,Ar4_F2z]=myconvert_stretchout(Ar4_F2,spacing)
[Ar4_F3x,Ar4_F3y,Ar4_F3z]=myconvert_stretchout(Ar4_F3,spacing)

[Ar8_F1x,Ar8_F1y,Ar8_F1z]=myconvert_stretchout(Ar8_F1,spacing)
[Ar8_F2x,Ar8_F2y,Ar8_F2z]=myconvert_stretchout(Ar8_F2,spacing)
[Ar8_F3x,Ar8_F3y,Ar8_F3z]=myconvert_stretchout(Ar8_F3,spacing)

%[Pristinex,Pristiney,Pristinez]=myconvert_stretchout(Pristine,spacing)
```


myconvert_stretchout.m

```
% This accepts as input a matrix 'a' and 'spacing'
% a is in grid format, use workspace50nm-grids-imported.mat for
example.
% interpolates with interp2 and k
% then returns variables ax, ay, az as the xyz components of the
interpol-
% ated matrix. These xyz columns can then be used for fitting
% also, in this specific case, we will convert entered negative shifts
% to positive shifts

%Comments inside the function are by Daniel Cutshall while trying to
%understand the code. See the comments at the end first for easier
%interpretation.
function [ax,ay,az] = myconvert(a,spacing)
%a=-1.*a      %Makes all of the negative Vfb values positive
[m,n]=size(a) % [rows,columns]
len=m*n      %Is this even used?

i=1
for yi=1:m    %This set of for loops seems to convert the input matrix,
a,
    for xi=1:n %to an array, ag, one row at a time
        ag(i)=a(yi,xi);
        i=i+1;
    end
end

i=1
for yi=0:m-1 %This set of for loops seems to create two arrays to
index the values in the previously
    for xi=0:n-1 %created array, ag, to the original matrix, a.
        x(i)=xi;
        y(i)=yi; %i.e. x(1)=1 and y(1)=0 indicates ag(1) is from column
1 and row 0 of input matrix a
        i=i+1;
    end
end
x=x'; %Transposes x array
y=y'; %Transposes y array

i=1
for yi=0:spacing:m-1
    for xi=0:spacing:n-1
        ax(i)=xi; %ax=[0,spacing,2*spacing,3*spacing,...,n-
1,0,spacing,2*spacing,...,n-1,...]
        ay(i)=yi;
%ay=[0,0,...,spacing,spacing,...,2*spacing,2*spacing,...,m-1]
        i=i+1;
    end
end
end
```

```
ax=ax'; %Transposes ax array
ay=ay'; %Transposes ay array

az=griddata(x,y,ag,ax,ay);
%x and y are arrays of sample point coordinates
%ag is an array of sample values
%ax and ay are arrays of query points
%az is an array of interpolated values
%'griddata' defaults to linear interpolation, but other options are
%available (nearest, natural, cubic, V4).
end
```

B.3 Code for creating Gaussian fit and integrating across the surface

make_elliptical_gaussian.m

```
function foo = make_elliptical_gaussian(A,x0,y0,a,b,c)
    disp('In foo!')
    foo = @elliptical_gaussian;
    function z=elliptical_gaussian(x,y)
        z=A*exp(-(a*(x-x0).^2 + 2*b*(x-x0).*(y-y0) + c*(y-y0).^2))
        %z=x./x;
    end
end
end
```

integration_script_stretchout.m

```
%load workspace 'integration_workspace.mat'

%Note that 'integration_workspace.mat' is created by importing
%'fit_parameters_for_integration_script.txt' (Daniel C)

fullrangexmin=-22.5/(2*2.5); %Border values for an Area corresponding
to the
fullrangexmax=+22.5/(2*2.5); %1" diameter Faraday cup (22.5mm x 22.5mm
square).
fullrangeymin=-22.5/(2*2.5); %Converted to 'Capacitor Coordinate
Points', e.g. for a
fullrangemax=+22.5/(2*2.5); %5x5 matrix the top left capacitor is at
x=0 y=0 and the
                                %bottom right capacitor is at x=4 and y=4.
                                %The 2.5 factor comes from the 2.5mm
                                %center-to-center distance between
capacitors

%Zeroing arrays initially (Daniel C)
integral_vals_on_sample_range=zeros([length(a),1]);
integral_vals_on_full_range=zeros([length(a),1]);
integral_vals_on_full_range_2=zeros([length(a),1]);

%Following lines added by Daniel C (updated manually if samples are
changed)
nominal_dose=[3.34E13,5.97E13,1.13E14,3.07E13,5.83E13,1.11E14,2.89E13,5
.50E13,1.04E14];
charge_state=[4,4,4,8,8,8,11,11,11];
charge_dose=nominal_dose.*charge_state;

for i=1:length(a) %'a' is the length of each imported fit parameter
array (DC)
    foo=make_elliptical_gaussian(A(i),x0(i),y0(i),a(i),b(i),c(i));
%Make elliptical Gaussian for each sample (DC)

    %Integrate the Gaussian curve for each sample over the sample area
    %(arbitrary units). Divide this by the number of samples (i.e.
area)
    %for average Vfb (DC)

integral_vals_on_sample_range(i)=integral2(foo,xmin(i),xmax(i),ymin(i),
ymax(i));

    %This integral is not useful... use shifted version, full_range_2
    %instead

integral_vals_on_full_range(i)=integral2(foo,fullrangexmin,fullrangexma
x,fullrangeymin,fullrangeymax);
```

```

    %Integrating across an area equal to that of the Faraday cup
    (fullrange values
    %above) but centered on the peak of the Gaussian fit function.
    integral_vals_on_full_range_2(i)=integral2(foo,x0(i)-
fullrangexmin,x0(i)+fullrangexmax,y0(i)-fullrangeymin,y0(i)+
fullrangeymax);

    %Lines below here are written by Daniel C.
    Dhruva_average_Vfb(i)=integral_vals_on_sample_range(i)/((xmax(i)-
xmin(i))*(ymax(i)-ymin(i))); %confirmed to be incorrect

Dhruva_adjusted_dose(i)=integral_vals_on_sample_range(i)/integral_vals_
on_full_range_2(i)*nominal_dose(i); %better to use full_range_2

    %Average Vfb calculation
    average_Vfb(i)=integral_vals_on_sample_range(i)/((xmax(i)-
xmin(i)+1)*(ymax(i)-ymin(i)+1));
    %Adjusted dose calculation

adjusted_dose(i)=integral_vals_on_sample_range(i)/integral_vals_on_full
_range_2(i)*nominal_dose(i);
    adjusted_charge_dose(i)=adjusted_dose(i)*charge_state(i);

    %Assumes that sample is centered on Faraday cup of 22.5mm x 22.5
mm;
    %full_range_2 might be a better approximation
    integral_vals_on_fc(i)=integral2(foo,-2.5,6.5,-2.5,6.5);

adjusted_dose_fc(i)=integral_vals_on_sample_range(i)/integral_vals_on_f
c(i)*nominal_dose(i);

end

```

Appendix C

MATLAB Code for Analysis with Schottky Diode Work

C.1 Code for plotting curves in various scenarios

Plotting_IV.m

```
%Daniel Cutshall
%August 2018
%Code to quickly plot I-V data for diodes vs. a reference

%USER INPUT - Filename
%If importing from .xlsx file put headers in the first row of each
column
%so that data isn't omitted.
tableA=readtable('G27NA#16_PreRad_IV.xls');
A=table2array(tableA);

%USER INPUT - Filename of reference data (e.g. discrete diode)
ref='IN4004.xls';
tableB=readtable(ref);
B=table2array(tableB);

%Get dimensions of table for creating data arrays
rowsA=height(tableA);
rowsB=height(tableB);

%Set up zeroed arrays for current, voltage, and |current|
refI=zeros(rowsB,1);
refV=zeros(rowsB,1);
absrefI=zeros(rowsB,1);
I1=zeros(rowsA,1);
V=zeros(rowsA,1);
absI1=zeros(rowsA,1);

%Arrange data into individual arrays.
%Change indices in A matrix to match how the data is arranged in the
%spreadsheet or text file.
for j=1:1:rowsA
    I1(j,1)=A(j,1);
    absI1(j,1)=abs(I1(j,1));
    V(j,1)=A(j,2);
end

%Change indices in B matrix to match how the data is arranged in the
%spreadsheet or text file.
for j=1:1:rowsB
    refI(j,1)=B(j,1);
    absrefI(j,1)=abs(refI(j,1));
    refV(j,1)=B(j,2);
end
```

```

%Output plots. The figure() function allows multiple figures to display
from
%the same script. The "hold on" command plots the curve on the previous
%graph with any existing data.
figure()
plot(V,I1,'Linewidth',1.5)
xlabel('Voltage [V]')
ylabel('Current [A]')
grid on           %Turn on major gridlines
axis([-3 3 -1E-6 12E-3])

hold on
plot(refV,refI,'Linewidth',1.5)
xlabel('Voltage [V]')
ylabel('Current [A]')
grid on           %Turn on major gridlines
axis([-3 3 -1E-6 12E-3])
legend('25nm D16',ref)

figure()
semilogy(V,absI1,'Linewidth',1.5)
xlabel('Voltage [V]')
ylabel('Current [A]')
grid on
axis([-3 3 1E-10 10E-3])

hold on
semilogy(refV,absrefI,'Linewidth',1.5)
xlabel('Voltage [V]')
ylabel('|Current| [A]')
grid on
axis([-3 3 1E-10 10E-3])
legend('25nm D16',ref)

%The following code added after plotting will allow a fixed window size
for
%all plots for easier visual comparison if desired:
%
%axis([xlow xhigh ylow yhigh])
%
%where 'low' and 'high' indicate lower and upper limits of the display
for
%the corresponding axis, respectively.

%To add a legend to either of the plots include the following code
after
%the command that generates the plot:
%
%legend('run1','run2','run3')
%
%where 'run1', 'run2', and 'run3' are the labels of the data sets.

```

```
%Could also use the following to generate the legend from the filenames  
of  
%the inputs:  
%  
%legend(file1,file2,file3)
```


Plotting_IV_1run.m

```
%Daniel Cutshall
%July 2018
%Code to import Schottky diode I-V data from txt file and create plots

%USER INPUT - Filename
tableA=readtable('SiSD15_0.50keV_Max_PostRad2.txt');
A=table2array(tableA);

%Get dimensions of table for creating data arrays
rows=height(tableA);

%Set up zeroed arrays for current, voltage, and |current|
I1=zeros(rows,1);
V=zeros(rows,1);
absI1=zeros(rows,1);

%Arrange data into individual arrays.
%Change indices in A matrix to match how the data is arranged in the
%spreadsheet or text file.
for j=1:1:rows
    I1(j,1)=A(j,2);
    absI1(j,1)=abs(I1(j,1));
    V(j,1)=A(j,1);
end

%Output plots. The figure() funtion allows multiple figures to display
from
%the same script
figure()
plot(V,I1,'Linewidth',1.5)
xlabel('Voltage [V]')
ylabel('Current [A]')
grid on          %Turn on major gridlines

figure()
semilogy(V,absI1,'Linewidth',1.5)
xlabel('Voltage [V]')
ylabel('Current [A]')
grid on
%%%%%%%%%%%%%%%%%%%%%%%%%%%%%%%%%%%%%%%%%%%%%%%%%%%%%%%%%%%%%%%%%%%%%%%%
%%%
%The following code added after plotting will allow a fixed window size
for
%all plots for easier visual comparison if desired:
%
%axis([xlow xhigh ylow yhigh])
%
%where 'low' and 'high' indicate lower and upper limits of the display
for
%the corresponding axis, respectively.
```

```
%%%%%%%%%%%%%%%%%%%%%%%%%%%%%%%%%%%%%%%%%%%%%%%%%%%%%%%%%%%%%%%%%%%%%%%%
%%%
%To add a legend to either of the plots include the following code
after
%the command that generates the plot:
%
%legend('run1','run2','run3')
%
%where 'run1', 'run2', and 'run3' are the labels of the data sets.
%Could also use the following to generate the legend from the filenames
of
%the inputs:
%
%legend(file1,file2,file3)
%%%%%%%%%%%%%%%%%%%%%%%%%%%%%%%%%%%%%%%%%%%%%%%%%%%%%%%%%%%%%%%%%%%%%%%%
%%%
```

Plotting_IV_3runs.m

```
%Daniel Cutshall
%July 2018
%Code to import Schottky diode I-V data from txt files and create plots

%USER INPUT - 1st Filename
tableA=readtable('SiSD15_0.50keV_Max_Rad2.txt');
A=table2array(tableA);

%USER INPUT - 2nd Filename
tableB=readtable('SiSD15_0.50keV_Max_PostRad2.txt');
B=table2array(tableB);

%USER INPUT - 3rd Filename
tableC=readtable('SiSD15_0.50keV_25_Max_Rad1.txt');
C=table2array(tableC);

%Get dimensions of table for creating data arrays
rows=height(tableA);

%Set up zeroed arrays for current, voltage, and |current|
I1=zeros(rows,1);
I2=zeros(rows,1);
I3=zeros(rows,1);
V=zeros(rows,1);
absI1=zeros(rows,1);
absI2=zeros(rows,1);
absI3=zeros(rows,1);

%Arrange data into individual arrays.
%Change indices in A matrix to match how the data is arranged in the
%spreadsheet or text file.
for j=1:1:rows
    I1(j,1)=A(j,2);
    I2(j,1)=B(j,2);
    I3(j,1)=C(j,2);
    absI1(j,1)=abs(I1(j,1));
    absI2(j,1)=abs(I2(j,1));
    absI3(j,1)=abs(I3(j,1));
    V(j,1)=A(j,1);
end

%Output plots. The figure() function allows multiple figures to display
from
%the same script
figure()
plot(V,I1,'Linewidth',1.5)
xlabel('Voltage [V]')
ylabel('Current [A]')
grid on %Turn on major gridlines
hold on %Allows following data to be plotted on the same graph
```

```

plot(V,I2,'Linewidth',1.5)
xlabel('Voltage [V]')
ylabel('Current [A]')
grid on
hold on

plot(V,I3,'Linewidth',1.5)
xlabel('Voltage [V]')
ylabel('Current [A]')
grid on

figure()
semilogy(V,absI1,'Linewidth',1.5)
xlabel('Voltage [V]')
ylabel('Current [A]')
grid on
hold on

semilogy(V,absI2,'Linewidth',1.5)
xlabel('Voltage [V]')
ylabel('Current [A]')
grid on
hold on

semilogy(V,absI3,'Linewidth',1.5)
xlabel('Voltage [V]')
ylabel('Current [A]')
grid on
%%%%%%%%%%%%%%%%%%%%%%%%%%%%%%%%%%%%%%%%%%%%%%%%%%%%%%%%%%%%%%%%%%%%%%%%
%%%
%The following code added after plotting will allow a fixed window size
for
%all plots for easier visual comparison if desired:
%
%axis([xlow xhigh ylow yhigh])
%
%where 'low' and 'high' indicate lower and upper limits of the display
for
%the corresponding axis, respectively.
%%%%%%%%%%%%%%%%%%%%%%%%%%%%%%%%%%%%%%%%%%%%%%%%%%%%%%%%%%%%%%%%%%%%%%%%
%%%
%To add a legend to either of the plots include the following code
after
%the command that generates the plot:
%
%legend('run1','run2','run3')
%
%where 'run1', 'run2', and 'run3' are the labels of the data sets.
%Could also use the following to generate the legend from the filenames
of
%the inputs:
%
```

```
%legend(file1,file2,file3)
%%%%%%%%%%%%%%%%%%%%%%%%%%%%%%%%%%%%%%%%%%%%%%%%%%%%%%%%%%%%%%%%%%%%%%%%
%%%
```

Plotting_PercentDiff.m

```
%Daniel Cutshall
%July 2018
%Code to calculate and plot both difference and percent difference
between
%pre-rad and post-rad Schottky diode I-V curves

%USER INPUT - Filename for 'reference' run
tableA=readtable('G26NA#1_PreRad_IV.xls');
A=table2array(tableA);

%USER INPUT - Filename for second run to be compared to the reference
run
tableB=readtable('G26NA#3_PreRad_IV.xls');
B=table2array(tableB);

%Get dimensions of table for creating data arrays
rows=height(tableA);

%Set up zeroed arrays for currents, voltage,difference, and percent
%difference
I1=zeros(rows,1);
I2=zeros(rows,1);
V=zeros(rows,1);
diff=zeros(rows,1);
percdiff=zeros(rows,1);

%Arrange data into individual arrays and calculate percent difference.
%Change indices in A matrix to match how the data is arranged in the
%spreadsheet or text file.
for j=1:1:rows
    I1(j,1)=A(j,1);
    I2(j,1)=B(j,1);
    V(j,1)=A(j,2);

    diff(j,1)=I2(j,1)-I1(j,1);
    percdiff(j,1)=(diff(j,1)/I1(j,1))*100;
end

%Output plots. The figure() funtion allows multiple figures to display
from
%the same script
figure()
plot(V,diff,'Linewidth',1.5)
xlabel('Voltage [V]')
ylabel('Difference')
grid on

figure()
plot(V,percdiff,'Linewidth',1.5)
xlabel('Voltage [V]')
```

```

ylabel('Percent Difference')
grid on
%%%%%%%%%%%%%%%%%%%%%%%%%%%%%%%%%%%%%%%%%%%%%%%%%%%%%%%%%%%%%%%%%%%%%%%%
%%%
%The following code added after plotting will allow a fixed window size
for
%all plots for easier visual comparison if desired:
%
%axis([xlow xhigh ylow yhigh])
%
%where 'low' and 'high' indicate lower and upper limits of the display
for
%the corresponding axis, respectively.
%%%%%%%%%%%%%%%%%%%%%%%%%%%%%%%%%%%%%%%%%%%%%%%%%%%%%%%%%%%%%%%%%%%%%%%%
%%%
%To add a legend to either of the plots include the following code
after
%the command that generates the plot:
%
%legend('run1','run2','run3')
%
%where 'run1', 'run2', and 'run3' are the labels of the data sets.
%Could also use the following to generate the legend from the filenames
of
%the inputs:
%
%legend(file1,file2,file3)
%%%%%%%%%%%%%%%%%%%%%%%%%%%%%%%%%%%%%%%%%%%%%%%%%%%%%%%%%%%%%%%%%%%%%%%%
%%%

```

C.2 Code for extracting diode parameters from I-V data

IV_Parameter_Extraction.m

```
%Daniel Cutshall
%July 2018
%Code to extract Barrier Height and Ideality Factor from I-V data.

%USER INPUT - Filename
%If importing from .xlsx file put headers in the first row of each
column
%so that data isn't omitted. The first sheet in the workbook is the
only
%thing that will be imported; can alter code to change this if desired.
tableA=readtable('G26NA#1_PreRad_IV.xls');
A=table2array(tableA);

%USER INPUT - Step size [V]
step=0.01;
n=log10(step);

%USER INPUT - Diode diameter [cm]
d=0.6;
Area=pi*(d/2)^2;

%Get dimensions of table for creating data arrays
rows=height(tableA);

%Set up zeroed arrays for current, voltage, and current density
I=zeros(rows,1);
roundedV=zeros(rows,1);
currDens=zeros(rows,1);

%Arrange data into individual arrays
%Change indices in A matrix to match how the data is arranged in the
%spreadsheet or text file.
%Voltage data is rounded because sometimes when measuring I record
measured
%voltage instead of programmed voltage.
for j=1:1:rows
    I(j,1)=A(j,1);
    currDens(j,1)=I(j,1)/Area;
    roundedV(j,1)=round(A(j,2),-n);
end

%Display semilog plot of J-V data to the user for determination of
linear
%region start and end points
semilogy(roundedV,currDens)
grid on
```



```

%Prompt User for starting and ending points of the linear region
prompt='Enter the voltage corresponding to the start of the linear
region in volts.\n';
stLinear=input(prompt);
prompt='Enter the voltage corresponding to the end of the linear region
in volts.\n';
endLinear=input(prompt);

%Create zero arrays for voltage and current density in the linear
region
LinearLength=int64((endLinear-stLinear)/step+1);
linearV=zeros(LinearLength,1);
linearJ=zeros(LinearLength,1);

%Create modified versions of the initial I-V arrays that only include
data
%for the linear region.
j=roundedV(1,1);
i=1;
transfer=1;
while transfer==1
    if j<(stLinear-step/10) %Added '-step/10' to fix what I assume was
just rounding issues with comparing 'j' and 'stLinear'
        j=j+step;
    elseif j>=(stLinear-step/10) && j<=(endLinear+step/10)
        x=int64((j-roundedV(1,1))/step+1);
        linearV(i,1)=roundedV(x,1);
        linearJ(i,1)=currDens(x,1);
        i=i+1;
        j=j+step;
    elseif j>(endLinear+step/10) %Added '+step/10' to fix what I assume
was just rounding issues with comparing 'j' and 'endLinear' in some
cases
        transfer=0;
    end
end

%Create exponential fit on region that is linear in the semi-log plot
and
%display the plot to the user
f=fit(linearV,linearJ,'exp1');
yintercept=f.a;
slope=f.b;
plot(f,linearV,linearJ) %not sure how to plot fit on semi-log right
now other than manually in plot editor.
grid on

%Constants for calculating barrier height and ideality factor
k=1.38*10^-23; %Boltzmann constant [J/K]
T=300; %Temperature [K]
q=1.6*10^-19; %Electronic charge [C]
R=129.6; %Richardson constant [A/(K^2-m^2)]

```

```

%Calculate and report the barrier height and ideality factor
phib=-k*T/q*log(yintercept/(R*T^2));
n=q/(slope*k*T);
fprintf('\n-----\n')
fprintf('The Schottky barrier height is phib=%0.3f',phib)
fprintf('\nThe ideality factor is n=%0.3f\n',n)
fprintf('-----\n');

%A couple final notes to the user
fprintf('\nPlease verify that linearV and linearJ arrays look
appropriate.\n\n')
fprintf('To determine R-squared value and other fit parameters type
"cftool" into the \ncommand window and do an exponential fit on
"linearV" and "linearJ".\n')

```

Note: The following code can be substituted for the code on the previous page in order to create the arrays that only have the linear data. The code here is actually more robust as it does not create errors when compliance is hit in the reverse bias region. (Data that hit compliance in the reverse region caused errors in the original code on the previous page and that is what caused me to make the new code here. It actually turned out to be much simpler too.)

```

%Create modified versions of the initial I-V arrays that only include
data
%for the linear region.
StIdx=find(roundedV==stLinear);
i=1;
for j=stLinear:step:endLinear
    linearV(i,1)=roundedV(StIdx,1);
    linearJ(i,1)=currDens(StIdx,1);
    StIdx=StIdx+1;
    i=i+1;
end

```

C.3 Code for extracting diode parameters from C-V data

CV_Parameter_Extraction.m

```
%Daniel Cutshall
%August 2018
%Code to extract Barrier Height and Ideality Factor from C-V data.

%USER INPUT - filename
%If importing from .xlsx file put headers in the first row of each
column
%so that data isn't omitted. The first sheet in the workbook is the
only
%thing that will be imported; can alter code to change this if desired.
tableA=readtable('G26NA#1_PreRad_CV.xls');
A=table2array(tableA);

%USER INPUT - absolute value of step size [V] (since absolute value of
%voltage is taken below).
step=0.01;
n=log10(step);

%USER INPUT - diode diameter [cm]
d=0.6;
Area=pi*(d/2)^2;

%Get dimensions of table for creating data arrays
rows=height(tableA);

%Set up zeroed arrays for capacitance, reverse voltage, and 1/(C'^2)
cap=zeros(rows,1);
RevV=zeros(rows,1);
InvCapSq=zeros(rows,1);

%Arrange data into individual arrays
%Change indices in A matrix to match how the data is arranged in the
%spreadsheet or text file.
%Voltage data is rounded because sometimes when measuring I record
measured
%voltage instead of programmed voltage.
for j=1:1:rows
    cap(j,1)=A(j,2);
    InvCapSq(j,1)=(1/(cap(j,1)/Area))^2;
    RevV(j,1)=abs(round(A(j,3),-n));
end

%Display plot of reverse voltage vs. 1/(C'^2) data to the user for
%determination of linear region start and end points
plot(RevV,InvCapSq)
grid on
```

```

%Prompt User for starting and ending points of the linear region
prompt='Enter the voltage corresponding to the start of the linear
region in volts.\n';
stLinear=input(prompt);
prompt='Enter the voltage corresponding to the end of the linear region
in volts.\n';
endLinear=input(prompt);

%Create zero arrays for voltage and current density in the linear
region
LinearLength=int64((endLinear-stLinear)/step+1);
linearV=zeros(LinearLength,1);
linearCSq=zeros(LinearLength,1);

%Create modified versions of the initial revV and InvCapSq arrays that
only
%include data for the linear region.
j=RevV(1,1);
i=1;
transfer=1;
while transfer==1
    if j<(stLinear-step/10) %Added '-step/10' to fix what I assume was
just rounding issues with comparing 'j' and 'stLinear'
        j=j+step;
    elseif j>=(stLinear-step/10) && j<=(endLinear+step/10)
        x=int64((j-RevV(1,1))/step+1);
        linearV(i,1)=RevV(x,1);
        linearCSq(i,1)=InvCapSq(x,1);
        i=i+1;
        j=j+step;
    elseif j>(endLinear+step/10) %Added '+step/10' to fix what I assume
was just rounding issues with comparing 'j' and 'endLinear' in some
cases
        transfer=0;
    end
end

%Create exponential fit on region that is linear and display the plot
f=fit(linearV,linearCSq,'poly1');
yintercept=f.p2;
slope=f.p1;
plot(f,linearV,linearCSq)
grid on

%Constants for calculating barrier height and ideality factor
k=1.38*10^-23; %Boltzmann constant [J/K]
T=300; %Temperature [K]
q=1.6*10^-19; %Electronic charge [C]
epsR=11.7; %Relative permittivity of Si
eps=8.85*10^-14; %Vacuum permittivity [F/cm]
mu_e=1350; %Electron mobility in Si
Nc=2.8*10^19; %Effective density of states in Si conduction
band

```

```
%[cm^-3]
```

```
%Calculate and report the barrier height and dopant concentration
```

```
Na=2/(q*epsR*eps*slope);
```

```
Vbi=(q*epsR*eps*Na*yintercept)/2;
```

```
phin=(k*T/q)*log(Nc/Na);
```

```
phib=Vbi+phin+(k*T/q);
```

```
fprintf('\n-----\n')
```

```
fprintf('The Schottky barrier height is phib=%0.3f',phib)
```

```
fprintf('\nThe dopant concentration is n=%0.2e\n',Na)
```

```
fprintf('-----\n');
```

```
%A couple final notes to the user
```

```
fprintf('\nPlease verify that linearV and linearCsq arrays look  
appropriate.\n\n')
```

```
fprintf('To determine R-squared value and other fit parameters type  
"cftool" into the \ncommand window and do an exponential fit on  
"linearV" and "linearJ".\n')
```

C.4 Code for determining the peak reverse current magnitude and the voltage point at which compliance is reached

PeakReverse_Compliance_Mult.m

```
%Daniel Cutshall
%February 2019
%Code to use the I-V data to determine peak reverse leakage current and
%voltage at which compliance is reached for multiple data sets and then
%plot the results.
%NOTE - Code assumes that all files have the same number of entries; if
%this is not true there will be issues with running.

clear
clc

%USER INPUT - Compliance Used for I-V Measurement
compl=10*10^-3;
percent=1;
tol=compl*percent*10^-2; %Min. value that is accepted as compliance

%USER INPUT - Number of input files; used to create arrays to store
data
%for peak reverse current and voltage corresponding to compliance
NumIn=10; %# of input files
PRM=zeros(NumIn,1); %Array for peak reverse current magnitudes
idx=zeros(NumIn,1); %Array for the indices of compliance voltages
VC=zeros(NumIn,1); %Array for the voltages where compliance is
reached
xstep=10; %Step size for x-axis (plotting purposes)
x=0:xstep:xstep*NumIn-xstep; %Array for x-axis values (plotting
purposes)

%USER INPUT - Input Files (add or delete lines depending on number of
input
%files)
tableA=readtable('PreRad_2019-01-31 10_01_49.txt');
A=table2array(tableA);
rows=height(tableA);

tableB=readtable('PostRad2_2019-01-31 11_11_50.txt');
B=table2array(tableB);

tableC=readtable('PostRad3_2019-01-31 11_24_57.txt');
C=table2array(tableC);

tableD=readtable('PostRad4_2019-01-31 11_37_56.txt');
D=table2array(tableD);

tableE=readtable('PostRad5_2019-01-31 11_51_33.txt');
```

```

E=table2array(tableE);

tableF=readtable('PostRad6_2019-01-31_12_04_29.txt');
F=table2array(tableF);

tableG=readtable('PostRad7_2019-01-31_12_17_21.txt');
G=table2array(tableG);

tableH=readtable('PostRad8_2019-01-31_12_31_09.txt');
H=table2array(tableH);

tableY=readtable('PostRad9_2019-01-31_12_44_02.txt');
Y=table2array(tableY);

tableZ=readtable('PostRad10_2019-01-31_12_56_54.txt');
Z=table2array(tableZ);

%Zeroed arrays for current and voltage
I=zeros(rows,NumIn);
V=zeros(rows,NumIn);

%Create matrix for all current and voltage data (add or delete lines
%depending on number of input files)
for j=1:1:rows
    I(j,1)=A(j,2);
    V(j,1)=A(j,1);

    I(j,2)=B(j,2);
    V(j,2)=B(j,1);

    I(j,3)=C(j,2);
    V(j,3)=C(j,1);

    I(j,4)=D(j,2);
    V(j,4)=D(j,1);

    I(j,5)=E(j,2);
    V(j,5)=E(j,1);

    I(j,6)=F(j,2);
    V(j,6)=F(j,1);

    I(j,7)=G(j,2);
    V(j,7)=G(j,1);

    I(j,8)=H(j,2);
    V(j,8)=H(j,1);

    I(j,9)=Y(j,2);
    V(j,9)=Y(j,1);

```

```

        I(j,10)=Z(j,2);
        V(j,10)=Z(j,1);
end

%Find peak reverse current magnitude and compliance for each of the
files
for k=1:NumIn
    PRM(k,1)=abs(min(I(:,k)))*10^6;
    idx(k,1)=find(abs(I(:,k)-compl)<tol,1,'first');
    VC(k,1)=V(idx(k,1),k);
end

%Calculate and display percent change for peak reverse current
magnitude
%and compliance voltage
PC_PRM=(PRM(NumIn,1)-PRM(1,1))/PRM(1,1)*100;
PC_VC=(VC(NumIn,1)-VC(1,1))/VC(1,1)*100;
fprintf('Percent change in peak reverse current magnitude is %0.2f
%%.\n',PC_PRM);
fprintf('Percent change in compliance voltage is %0.2f %%.\n',PC_VC);

%Create scatter plots for the peak reverse current and the compliance
%voltage as a function of irradiation time.
%The figure() funtion allows multiple figures to display from the same
%script.
figure()
scatter(x,PRM,'filled','blue','o');
title('Sample G26NA#1 - Thick - 0.50 keV')
xlabel('Irradiation Time [minutes]')
ylabel('Peak Reverse Current Magnitude [\muA]')
xlim([-10 100])
grid on

figure()
scatter(x,VC,'filled','blue','o');
title('Sample G26NA#1 - Thick - 0.50 keV')
xlabel('Irradiation Time [minutes]')
ylabel('Voltage @ Compliance Point [V]')
xlim([-10 100])

grid on

```


Appendix D

Miscellaneous Procedural Guides and Manuals

D.1 Guide for operating the Edwards thermal evaporator

1. Plug in the power cord
2. Flip the switch on the power strip (Instrument power)
 - a. Gauge #1 → Active Inverted Magnetron (AIM) gauge; 10^{-3} to 10^{-8} torr (9 in diagram: pressure in vacuum chamber)
 - b. Gauge #2 → Pirani gauge; 760 to 10^{-4} torr (9 in diagram: pressure in vacuum chamber)
 - c. Gauge #3 → Pirani gauge; 760 to 10^{-4} torr (8 in diagram: rotary pump line)
3. Turn the rotary pump on by moving the pump knob to the 3 o'clock position
 - a. Note: If pressure on gauge #3 is high and not going down, then slightly open the ballast valve on the rotary pump
4. Once the pressure on gauge #3 is below 3×10^{-2} torr, open the backing valve.
 - a. Note: Make sure the backing valve and rouging valve are **not** open at the same time
5. Turn the diffusion pump on by moving the pump knob to the 6 o'clock position (“diff/rot pump”). **Note the time!**
6. Turn on the water chiller
 - a. Make sure water level is o.k.
 - b. Temperature should settle around 19 °C
7. Insert the shorting plug into the appropriate socket based on what metal is being evaporated. Once inserted, give the shorting plug a twist to ensure a good contact.
8. Gather the required materials before opening the chamber (sample, metal, shadow mask, gloves, etc.). Put gloves on!
 - a. Note: Want the chamber to be open for the shortest amount of time possible
9. Make sure that the high vacuum valve and the roughing valve are **both** closed
10. Open the “air admittance” valve to bring the vacuum chamber to 760 torr
11. Remove the implosion guard (protective plastic cover)
12. **Gently** lean on the bell to get it off
 - a. If it does not move then wait a while and try again
13. Lift the bell jar straight off and place it on its side in the appropriate place on the work bench
14. Remove the metal shields (take note of their position and orientation as you do so)

- a. Note: if there is too much debris in the chamber the vacuum seal might be affected and/or the diffusion pump might be contaminated. Contact Dr. Harriss to clean debris.
15. Make sure the Ta shield between the two filaments is **not** touching either of the powered electrodes
16. To determine the appropriate amount of metal needed, consult the Excel spreadsheet (amount of metal depends on height of sample and thickness of desired deposition)
17. Place the desired amount of metal in the center of the W filament (coil)
 - a. Note: You can temporarily remove the support plate to make this easier. When replacing the support plate, make sure that it is flat and firmly secured.
18. Place the shutter in position #1 (marked on the table)
19. Place a shadow mask and your sample on the support plate
20. Insert a glass slide on the side of the chamber if a viewing window is desired
21. Lower the top cap/dome to minimize the evaporation onto the bell jar
22. Place the metal shields around the chamber in the same position that they were removed from (making small changes to accommodate the viewing window)
23. Line up the bell jar before placing it. Once it is down it cannot be rotated easily (doing this will move the metal shields). Make sure the jar is approximately centered
24. Place the implosion guard over the bell jar such that the two weak spots face the wall
25. Close the “air admittance” valve snugly (but **not** too tight)
26. Check to make sure it has been 28 to 30 minutes since turning on the diffusion pump
 - a. If it has been around 23 to 28 minutes since turning on the diffusion pump then consult step 26 b. below; otherwise proceed to step 27
 - b. Gas builds up in diffusion pump from 23 to 28 mins after starting → need to have backing valve opened at least intermittently during this time frame, **but** you want to “rough” the vacuum chamber (via the roughing valve) ASAP after putting the bell jar on. If you put the bell jar on during this time range then close the vacking valve and open the roughing valve. After 2 or 3 minutes close the roughing valve and open the backing valve for 5 – 10 seconds. Repeat until it has been ~28 mins since turning on the diffusion pump.
27. Close the backing valve
28. Open the roughing valve

29. Wait until gauge #2 is less than 5×10^{-2} torr. Once this pressure is reached proceed to the next step
30. Close the roughing valve and pause for a few seconds
31. Open the backing valve
32. Start to open the high vacuum valve
 - a. Move **slowly** after the first 20°
 - b. **Stop** when you feel a bump **and/or** when you see gauge #3 pressure increase
 - c. Note: Keep the pressure on gauge #3 below 10^{-2} torr. If it gets above this, then close the high vacuum valve. **Do not** expose hot diffusion pump oil to high pressures of oxygen (air).
 - d. Let the pressure stabilize, and then continue to open the high vacuum valve the rest of the way. Once the handle is vertical you can quickly open it the rest of the way.
33. Pump down to a base pressure of 5×10^{-6} torr. Once this pressure is reached proceed to the next step
 - a. Note: This usually takes approximately 45 minutes
34. Verify that the shutter is 'closed' (in position 1 as marked on the table)
35. Make sure variac is initially off with the knob pointing at 0
36. Turn on the power and adjust to 5 for about 5 to 10 seconds
 - a. Note: this step is to warm up the filament
37. Turn power to 10 and let it sit there. The filament will begin to glow; wait for the glow to stabilize before proceeding to the next step (usually takes 10 – 15 seconds). **For Al** proceed to the next step
38. Turn power to 15 (or 17) and wait for the filament to get darker in the center (the point when the metal begins to melt). **Immediately** proceed to the next step!
39. Open the shutter by pulling the lever all the way towards you.
40. After the glow has recovered (usually takes 15 – 30 seconds), turn power to 20 and leave it for 30 seconds to **1 minute**
41. Turn power to 25 for **30 seconds** to 1 minute
42. Turn power to 30 for ~30 seconds
43. Turn power to 40 for ~15 seconds
 - a. Note: This step is to remove the Al from the filament
 - b. Note: as the heat increases, the pressure in the chamber will also increase
44. Turn power to 0 and turn off the variac
 - a. Note: You can close the shutter at this point, but it is not crucial
45. Wait for pressure to return to where it was before turning on the power (5×10^{-6})
 - a. Usually wait about 3 – 5 minutes

46. Close the high vacuum valve
 - a. Do not have to do this slowly
47. Open the “air admittance” valve until pressure in the chamber is 760 torr
48. Remove the implosion guard, bell jar, and metal shields as described in steps 11 – 14
49. Lift the top cap/dome
50. Remove your sample and replace the shadow mask from where you got it
51. Getting the chamber in vacuum for storage
 - a. Replace the metal shields, bell jar, and implosion guard
 - b. Close the “air admittance” valve
 - c. Close the backing valve
 - d. Open the roughing valve
 - e. Wait until the pressure is below 5×10^{-2} torr (gauge #2)
 - f. Close the roughing valve
 - g. Open the backing valve (do this **quickly after** step 51 f.)
 - h. Immediately start opening the high vacuum valve as described in step 32
 - i. Pump down to 5×10^{-5} torr (gauge #1)
52. Quick Shutdown
 - a. Close high vacuum valve (pressure will increase due to outgassing)
 - b. Turn the diffusion pump off (move pump knob to 3 o'clock position)
 - c. Close the backing valve
 - d. Turn the rotary pump off (move pump knob to 12 o'clock position)
 - e. Turn off the water chiller
 - f. Turn off the power strip
 - g. Unplug the cord and place it under the evaporator base

D.2 Guide for performing high frequency C-V measurements with the HP4280A

1. Turn on HP 4280A 1 hour prior to taking measurements by pushing the Line On/Off button so that the lights come on. (Note: the 1 hour prior to taking measurements is a warm up time)
2. Make sure the HP 4280A is appropriately grounded (on the lower left corner of the front panel).
3. Connect a 1 meter test lead (BNC, grey color) between the 'High' input ('Unknown' terminals) on the HP 4280A and 'probe 1' of the probe station via simple coax connectors on the left side of the probe station. (Note: 'probe 1' is an arbitrarily selected probe in the probe station)
4. Connect a 1 meter test lead (BNC, grey color) between the 'Low' input ('Unknown' terminals) on the HP 4280A and 'probe 2' of the probe station via simple coax connectors on the left side of the probe station. (Note: 'probe 2' is an arbitrarily selected probe in the probe station)
5. If making measurements with voltage magnitudes greater than 42 V, do the following:
 - a. Connect the inner conductor of the 'Remote ON/OFF' BNC to ground by using a BNC to alligator clip converter. (Note: ground is to the left of the 'Unknown' terminals. This ground terminal should also be connected to a common system ground...place where all other equipment is grounded, see Step 2) (see p. 3-38 in the manual)
 - b. Switch the 'Int Bias' switch to ' ± 100 V Max'.
6. Select 'Floating' in the 'Connection Mode' box.
7. In 'Function' select the parameter(s) that you want to measure (normally we select 'C').
8. In 'C-G Range' select 'Auto' for preliminary test. You can select 'Manual' to manually choose between the three options listed to the right if the desired range is known.
9. Set 'Meas Speed' to 'Slow'.
10. Set 'Sig Level' to '30' (mV rms).
11. Make sure 'C-High Resoln' is disabled (LED off)
12. Make sure all three 'Math' buttons are disabled (LEDs off)
13. Make sure the 'Store Digit Shift' buttons are disabled (LEDs off for the two buttons with LEDs, not concerned with the button without a LED)
14. Not concerned with the three 'X-Y Recorder' buttons
15. For C-V sweep, select the 'Single' button above 'Sweep Mode'. (Note: This button has two purposes depending on the test being run; i.e. 'Trigger' vs. 'Sweep Mode' functions, see p. 3-7 in the manual).
16. Hit the 'Internal Bias' button until the diagram depicting a single staircase sweep is selected (2).

17. Set the 'Start V' by doing the following:
 - a. Hit the up and down arrow keys in the 'Parameter' box until the light next to 'Start V' is lit.
 - b. Hit the blue key; the key directly below the 'Enter' key (note: keys will now perform the function denoted by the blue ink below the respective keys).
 - c. Use the keypad (blue ink in the 3 columns of buttons under 'Math') to select the values.
 - d. Hit the 'Enter' key to confirm the value (the value should appear in the 'V-t' display screen).
18. Set 'Stop V', 'Step V', 'Hold Time', and 'Step Delay Time' in the same manner described in the previous step (Step 17). Typical values of 'Hold Time' and 'Step Delay Time' are 60 s and 1 s respectively. (Values can be changed to milliseconds by hitting the down arrow in 'Parameter' after selecting the desired value).
19. Internal Error Correction (see p. 3-35 in the manual) (Note: both 'probe 1' and 'probe 2' should NOT be touching anything at this point)
 - a. Make sure 'Enable' key in the 'Correction' box is disabled (LED off)
 - b. Hit the down arrow in the 'Correction' box until '1' (m) is selected (the LED next to '1' is on)
 - c. Press the small black 'Open' button under 'Zero' (to the right of the 'Int Bias')
 - d. Push the 'Enable' key in the 'Correction' box (so that the LED is lit)
 - e. OPTIONAL: Push the 'Repeat' button above 'Sweep Mode' (LED lit) and change the 'Internal Bias' to DC Level (1). The displayed capacitance should be near 0 if the internal error correction was done correctly.
 - f. If Step (19-E) was performed: Select 'Single' above 'Sweep Mode' (LED lit) and change the 'Internal Bias' to single staircase sweep (2).
20. Place the sample to be tested on the chuck and turn the vacuum pump on. Connect the outer conductors of 'probe 1' and 'probe 2' with a small cable as close as possible to the DUT to remove the parasitic capacitance (see Figure 3.10 on p. 3-33 in the manual; also, see Figure 1 below). Place 'probe 1' on the top metal contact of the capacitor to be tested. Place 'probe 2' on the chuck near the capacitor being tested.

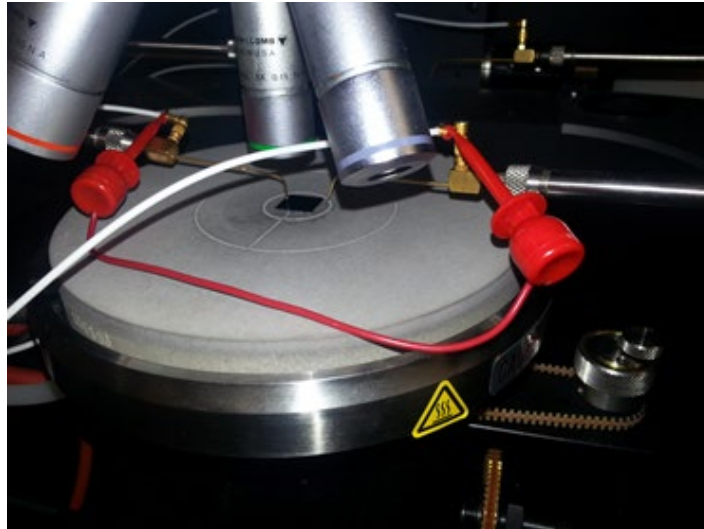


Figure 1: Image showing how to connect the outer conductors of ‘probe 1’ and ‘probe 2’ (color version on computer).

21. Connecting a computer and configuring the settings (note: this is just one of several possible methods):
 - a. Connect a HPIB-USB controller between the HP 4280A and a laptop
 - b. Adjust the HPIB settings on the HP 4280A to address ‘51: Talk Only Comma’ (see Figure 2 for clarification).
 - c. On the HP 4280A, select ‘Repeat’ above ‘Sweep Mode’ and change the ‘Internal Bias’ to DC Level (1)
 - d. Boot laptop into Ubuntu (or some type of LINUX system)
 - e. Open a terminal and type “dmesg | grep -i USB” to identify the USB port where the connector in part (a) is attached. (Note: you are looking for something in the output like: “FTDI USB Serial Device converter now attached to **ttyUSB0**”)
 - f. In the terminal type “sudo minicom -s” for serial port setup
 - g. Scroll down to “Serial port setup” and hit enter
 - h. Hit the ‘A’ key and change the serial device address to what was found in part (e). Hit enter.
 - i. Hit the ‘E’ key to set ‘Bps/Par/Bits’ by doing the following:
 - i. Hit the ‘C’ key to select 9600 as the speed
 - ii. Hit the ‘N’ key to select odd parity
 - iii. Hit the ‘V’ key to select 8 bit data
 - iv. Hit the ‘W’ key to select 1 stop bit. Hit enter and verify that the values edited for options ‘A’ and ‘E’ are correct. If values are correct, hit enter again.
 - j. Scroll down to “Save setup as dfi” and hit enter to save the setup as the default setup if desired.

- k. Scroll down to “Exit” and hit enter. Data should be displayed in the terminal; if data is not displayed, consult Step (21-C). (Note: if you exit minicom entirely, type “sudo minicom” in the terminal to start dumping data to the terminal)
- l. At any point while minicom is running, hit ‘ctrl’ + ‘A’ and then ‘Z’ for the minicom command summary.
- m. On the HP 4280A, select ‘Single’ above ‘Sweep Mode’ and change the ‘Internal Bias’ to single staircase sweep (2). (Note: the data can be cleared from the terminal by hitting ‘ctrl’ + ‘A’ and then ‘C’ if desired)
- n. Hit ‘ctrl’ + ‘A’ and then ‘L’ and type a file name where the data will be captured and then hit enter (Example filename: **C-V_Data.txt**)

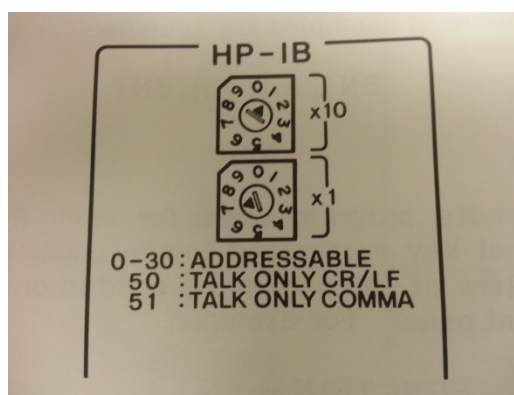


Figure 2: HPIB settings for the HP 4280A (located on the back). The dials should be adjusted to address ‘51: Talk Only Comma’. (Note: The address shown in the image above is 17).

22. Hit the orange ‘Start/Stop’ button to begin the C-V sweep (sweep will stop automatically as long as ‘Single’ is selected).
23. After the sweep is completed go to the terminal and hit ‘ctrl’ + ‘A’ and then ‘L’. In the ‘Capture file’ box that comes up select ‘Close’ and hit enter. The file with the captured data will be in the Home Folder. (see p. 3-102 in the manual for a description of data)

Note: Exit minicom before disconnecting the USB from the computer. This is done by hitting ‘ctrl’ + ‘A’ and then ‘X’.

Getting the Data from the txt File to Excel

(Note: These directions are for Excel 2010; the procedure might vary slightly for other versions.)

1. Open Excel and click on the “Data” tab
2. In the “Get External Data” section select the option “From Text” and choose the desired file in the window that pops up
3. Choose the appropriate delimiters (typical delimiters are comma, other – “A”, other – “C”, etc.). Note: you might not be able to separate the data entirely in one attempt; see the next step

4. If further delimiting is required:
 - a. Highlight the data that requires delimiting
 - b. In the “Data Tools” section select the option “Text to Columns”
 - c. Select appropriate delimiters
 - d. Repeat until data is in the desired form

D.3 Guide for performing quasi static C-V measurements with the HP4140B

1. Turn on the HP 4140B 1 hour prior to taking measurements by pushing the Line On/Off button so that the lights come on. (Note: the 1 hour prior to taking measurements is a warm up time)
2. Make sure the 16054A Connection Selector is attached to the front of the 4140B.
3. Make sure the "Low Lead Connection" switch of the 16054A is set to 'V_A'.
4. Make sure the HP 4140B is appropriately grounded (on the lower left corner of the front panel behind the 16054A connection selector).
5. Connect a triaxial cable between 'I' on the 16054A (which is connected to 'I Input' on the 4140B) and 'probe 1' via a triaxial to BNC converter connection on the left side of the probe station. (Note: 'probe 1' is an arbitrarily selected probe in the probe station)
6. Connect a short BNC cable between 'V_A' on the 16054A and 'probe 2' via the following steps (Note: 'probe 2' is an arbitrarily selected probe in the probe station):
 - a. Connect 'V_A' to a BNC connection outside of the probe station
 - b. For the same connector in part (a), connect a BNC to banana (female) converter on the inside of the probe station
 - c. Connect ONLY the non-'GND' side of a banana (male) to BNC converter to the female banana labeled 'GND'. The effect is to connect the outer conductor of the initial coax to the inner conductor of the final coax (the probe tip). See Figure 1 for clarification.
 - d. Connect the BNC output from part (c) to 'probe 2'. See Figures 2 and 3 for more detail on the circuit created by the connections described in Steps 5 and 6. The connection is also shown on page 3-40 of the manual.

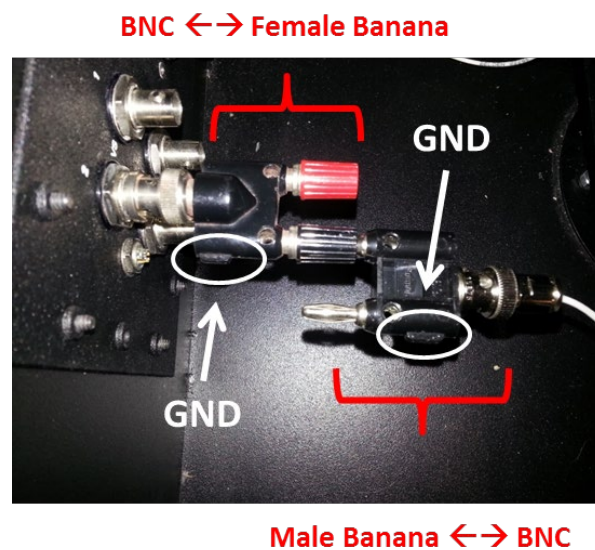


Figure 1: Image showing the details of the connection between 'V_A' on the 16054A and 'probe 2' (color version on computer).

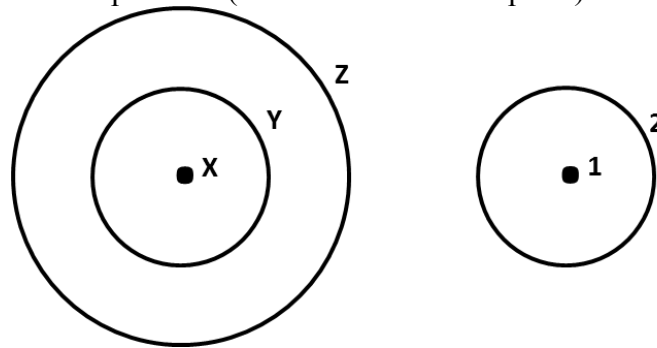


Figure 2: Cross sectional view of cables. Assigning variables to the different conductors of the triaxial cable (left) and the coaxial cable (right).

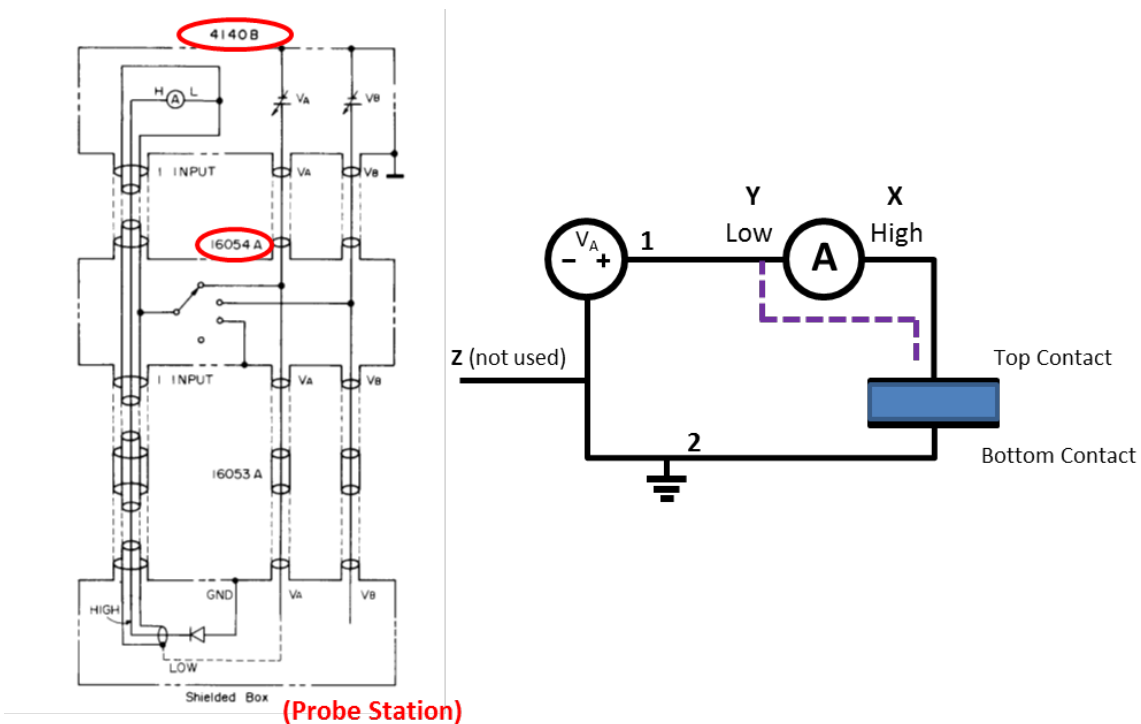


Figure 3: Connection diagram from the manual for 'Grounded DUT Measurement', p. 3-43 (left), and a simplified circuit (right) using the variables defined in Figure 2 (color version on computer). Note: the dashed purple line in the figure on the right may not be relevant.

7. Place the sample to be tested on the chuck and turn the vacuum pump on. Place 'probe 1' on the top metal contact of the capacitor to be tested. Place 'probe 2' on the chuck near the capacitor being tested.
8. Setting the appropriate 'I Range':

- a. Select 'I-V' as the 'Function'
 - b. Set 'I Range' to 'Auto'
 - c. In the 'Function' block for V_A and V_B , make sure the single sided staircase (3) is selected for ' V_A ' and 'OFF' (2) is selected for ' V_B '. (Note: These should be the default settings after selecting 'I-V' as the 'Function' as described in part (a)).
 - d. Set up a voltage sweep by selecting appropriate values for 'Start V', 'Stop V', 'Step V', 'Hold Time', 'Step Delay Time', and 'dV/dt' (see Step 13 below). (Note: These values must be the same values that you will use for your C-V sweep).
 - e. Hit the 'Auto Start' button under 'V Sweep' (note: if the Red LED near 'V Output' is solid, then a test is running. If the LED is blinking, then there is an error.)
 - f. Take note of the highest current magnitude shown in the range display. Range display is between the 'E' and 'A' (Example: -11 is a higher current magnitude than -12).
 - g. After the test is complete ('V Output' LED is off), use the up and down arrow keys in 'Manual' under 'I Range' to select the highest current magnitude observed, as noted in part (f). (Note: Make sure that 'Auto' under 'I Range' is NOT selected; LED off)
9. Select 'C-V' as the 'Function'
 10. Select 'Long' for 'Integ Time'
 11. Make sure the 'Filter' button is on (LED lit)
 12. In the 'Function' block for V_A and V_B , select the smooth, single sided ramp (1) for ' V_A ' and select 'OFF' (2) for ' V_B ' by using the appropriate down arrow keys
 13. Setting the appropriate parameters for V_A :
 - a. Push the ' V_A ' button in the 'Parameter' box
 - b. Push the 'Start V' button and use the keypad to the right to select the desired value. Press 'Enter' to store the value
 - c. Set 'Stop V', 'Step V', 'Hold Time', 'dV/dt', and 'Step Delay Time' in the same manner described in part (b). Typical values of 'Hold Time', 'dV/dt' and 'Step Delay Time' are 60 s, 0.01 V/s and 1 s respectively
 14. Offsetting the effect of the cables (zero offset)
 - a. Remove 'probe 1' from the capacitor, and remove 'probe 2' from the chuck (neither of the probes should be touching anything at this point)
 - b. Push the 'Auto Start' switch under 'V Sweep'
 - c. Wait for the value in the display under 'I . C' to stabilize
 - d. After the value described in part (c) has stabilized, push the 'Zero' button to the left of the 'I . C' display. (The effect is that the displayed capacitance is stored in ROM and it will be subtracted from subsequent capacitance measurements; therefore, the open circuit value should be approximately zero.)
 - e. Hit the 'Abort' button

15. Place 'probe 1' on the top metal contact of the capacitor to be tested. Place 'probe 2' on the chuck near the capacitor being tested.
16. Use the arrows keys in the 'Current Limit (A)' box (pointing to the right) to select 10^{-4} (1) for both V_A and V_B . (Note: the value corresponding to V_B is not really relevant since we are using V_A)
17. Connecting a computer and configuring the settings (Note: this is just one of several possible methods):
 - a. Connect a HPIB-USB controller between the HP 4140B and a laptop
 - b. Adjust the HPIB settings on the HP 4140B to 'Talk Only' (see Figure 4 for clarification).
 - c. On the HP 4140B, hit the 'Local' button so that **only** the LED below 'Talk' is lit (LED under 'Remote' should be off).
 - d. Then hit the 'I' button under 'Function' and make sure that 'Int' is selected under 'I Trig'. (The purpose of this step is to configure the HP 4140B so that it can display values in the terminal in a later step; step (17-L). This is to verify the connection).
 - e. Boot laptop into Ubuntu (or some type of LINUX system)
 - f. Open a terminal and type "dmesg | grep -i USB" to identify the USB port where the connector in part (a) is attached. (Note: you are looking for something in the output like: "FTDI USB Serial Device converter now attached to **ttyUSB0**")
 - g. In the terminal type "sudo minicom -s" for serial port setup
 - h. Scroll down to "Serial port setup" and hit enter
 - i. Hit the 'A' key and change the serial device address to what was found in part (f). Hit enter.
 - j. Hit the 'E' key to set 'Bps/Par/Bits' by doing the following:
 - i. Hit the 'C' key to select 9600 as the speed
 - ii. Hit the 'N' key to select odd parity
 - iii. Hit the 'V' key to select 8 bit data
 - iv. Hit the 'W' key to select 1 stop bit. Hit enter and verify that the values edited for options 'A' and 'E' are correct. If values are correct, hit enter again.
 - k. Scroll down to "Save setup as dfl" and hit enter to save the setup as the default setup if desired.
 - l. Scroll down to "Exit" and hit enter. Data should be displayed in the terminal; if data is not displayed, consult steps (17-C) and (17-D). (Note: if you exit minicom entirely, type "sudo minicom" in the terminal to start dumping data to the terminal)
 - m. At any point while minicom is running, hit 'ctrl' + 'A' and then 'Z' for the minicom command summary.

- n. On the HP 4140B, select 'C-V' under 'Function'; all sweep parameters previously set should be saved. (Note: the data can be cleared from the terminal by hitting 'ctrl' + 'A' and then 'C' if desired)
- o. Hit 'ctrl' + 'A' and then 'L' and type a file name where the data will be captured and then hit enter (Example filename: **C-V_Data.txt**)



Figure 4: HPIB setting for the HP 4140B (located on the back). The switch circled in red should be positioned to the left; 'talk only' (color version on computer).

- 18. Push the 'Auto Start' button under 'V Sweep' to begin the C-V sweep
- 19. After the sweep is completed go to the terminal and hit 'ctrl' + 'A' and then 'L'. In the 'Capture file' box that comes up select 'Close' and hit enter. The file with the captured data will be in the Home Folder. (see p. 3-57 in the manual for a description of data)

Note: Exit minicom before disconnecting the USB from the computer. This is done by hitting 'ctrl' + 'A' and then 'X'.

Note: If the buttons on the HP 4140B become unresponsive while the computer is connected, make sure that the LED under 'Remote' is off; see Step 17-C.

Location of Useful Information in the Manual

- p. 1-6.....Ranges and resolution for several of the operating parameters (Start voltage, stop voltage, step voltage, hold time, step delay time, ramp rate [dV/dt])
- p. 3-3.....Details on the integration times and their relation to the current range being used; the same information is given on p. 3-10
- p. 3-29.....General considerations for performing a CV measurement
- p. 3-31.....Plots showing the relationship between the following 3 things: capacitance being measured, current range, dV/dt
- p. 3-38.....CV function operation instructions (i.e. procedure for performing a CV test)
- p. 3-47.....Error codes ("annunciations")

p. 3-52.....HP-IB interface

D.4 Guide for performing manual C-V sweeps with the Agilent E4980A LCR meter

(Procedure transcribed from p. 41 of Daniel Cutshall's #1 lab notebook and elaborated on by Daniel Cutshall on June 7, 2016. Initial procedure was described by Githin Alapatt on July 30, 2013).

1. Hit the “**Meas Setup**” button and adjust the values as desired. Values usually controlled via Keithley and their typical values are shown below (see p. 91 in the Agilent user's guide for a brief description of each variable name):
 - a. **FUNC** → series or parallel (see p. 195 of the Agilent user's guide for some guidelines about what mode to choose for a particular measurement)
 - b. **FREQ**
 - c. **LEVEL** → typically 50 mV
 - d. **RANGE** → typically 100 Ω
 - e. **MEAS TIME** → typically long
 - f. **TRIG** → set to “**MAN**” to allow for manual triggering
2. In the measurement setup window select the “**List Setup**” soft key.
3. Under the “**Seq**” column select the variable to be swept
 - a. **Freq [Hz]** → frequency sweep
 - b. **Bias [V]** → voltage sweep
 - c. Etc.
4. In the first entry of the sweep variable place the desired start point (e.g. 50 Hz)
5. Use the arrow keys and the “**Next Page**”, “**Prev Page**” soft keys to go to the position of the last entry of the sweep variable and enter the desired stop value for the sweep variable.
 - a. This position is determined from the desired start, stop, and step values of the sweep variable. For instance if we want to sweep from 0 V to 5 V in steps of 0.1 V then the last entry will be in position 51.
6. Select the “**fill linear**” soft key to fill in all values between the start point and the end point.
 - a. Note: You can also choose to “**fill log**”
 - b. Note: The table can be cleared at any point by going to “No.” in the top left of the table and selecting the “**Clear Table**” soft key.
7. Insert a flash drive into the USB port of the LCR meter and hit the “**Save/Recall**” button
8. Hit the “**Save Data**” soft key
9. Hit the “**Start Log**” soft key
10. Hit the “**Display Format**” button

11. Hit the “**List Sweep**” soft key
12. Hit the “**DC Bias**” button (The LED below *DC Bias* on the upper right of the front panel should turn on.)
13. Hit the “**Trigger**” button to manually trigger the sweep to begin. Measurements should begin to populate the list as the desired variable is swept.
14. After the measurement is complete hit the “**Save/Recall**” button
15. Hit the “**Save Data**” soft key
16. Hit the “**Save & Stop**” soft key
17. Note the filename at the bottom of the screen; it will be of the form *E498x037.csv* (If an error message is displayed or no file name is displayed then repeat the measurement.)
18. Hit the “**DC Bias**” button to turn off the DC bias (the LED mentioned in step 12 should be off now.)
19. Remove the flash drive (safe to remove if the LED below *USB* on the upper right of the front panel is off).

D.5 Basic operational guide for the HP4156B precision semiconductor parameter analyzer

Note: Many of the steps here are mentioned in equal or greater detail in the quick start guide (a hard copy should be located somewhere near the HP 4156B).

1. Hit the “**Chan**” button and select the measurement mode (either “**Sweep**” or “**Sampling**”) using the soft keys on the right hand side of the display.
2. In the same screen use the arrow keys to navigate and assign the channels appropriately with the soft keys on the right hand side of the display.
 - a. Consider the example of a two terminal voltage sweep; we would have the following: *SMU1* → *mode: V, FCTN: VARI* and *SMU2* → *mode: COMMON, FCTN: CONST*
3. Hit the “**Meas**” button to select the parameters for the measurement.
4. Use the arrow keys to navigate to the desired parameter, input the desired value using the number pad, and then hit the “**Enter**” button to confirm the value.
5. The window for the plotted data can be selected manually prior to the run by hitting the “**Display**” button and inputting the desired values with the number pad and the “**Enter**” button.
6. Hit the “**Graph/List**” button prior to starting the measurement to see the data being plotted in real time (Note: hitting the “**Graph/List**” button multiple times in succession will toggle between the *graph* of the data and the *list* of the data).
7. Select the integration time by hitting one of the following three buttons in the *Integ Time* section of the front panel: “**Short**”, “**Medium**”, “**Long**” (Note: the integration time can be changed mid run if desired).
8. Hit the “**Single**” button to start the measurement (Note: while the measurement is taking place the LED by *MEASUREMENT* in the top right corner of the front panel will be on).
9. After the measurement is done the plot can be auto scaled by doing the following: select the “**Scaling**” soft key on the bottom of the display and then select the “**Auto Scaling**” soft key on the right hand side of the display.
10. To perform a second measurement while preserving the data from the first measurement hit the “**Append**” button.
11. To save the data as a .DAT file (can be assessed later in the HP 4156B) hit the “**System**” key followed by the “**Save**” soft key. Enter a file name and then select the “**Execute**” soft key at the bottom of the display.

12. To save the data as a .TXT file hit the “**Graph/List**” button until the list is displayed, and then select the “**Spreadsheet**” soft key. Enter a file name and then select the “**Execute**” soft key at the bottom of the display.

D.6 Operation manual for the singly charged ion beamline in Kinard 13

Pumping Down

- Load sample and completely shut vacuum port door
- First hand tighten ‘*Gold-Seal Valve*’ and then tighten to **8 ft-lb (96 in-lb)** with appropriate torque wrench
- Open the gate valve (below *Floating High Voltage Supply* rack)
 - Hit red button under plastic guard. Button should be flush with the panel after pushing.
 - Hit small red push button (reset switch) and listen for sound of gate valve opening.
- Turn on the mechanical/backing pump by switching on the power strip.
- Within **~30 seconds** of turning on the mechanical/backing pump, hit the “*start*” button on the orange box that controls the TMP
- After the TMP reaches “normal” operation, turn on the pressure gauge for channel 1.
- Wait for appropriate pressure before starting up ion beam
 - 10^{-8} Torr → ideal
 - 10^{-7} Torr → o.k.
 - 10^{-6} Torr → something wrong!

Starting Ion Beam

SAFETY NOTE: Once acceleration voltage is turned up everything in the acrylic box is potentially at “*beam potential*”. Be cautious of HIGH VOLTAGES!

- Connect the Arduino to the 9V battery until the three series 6 volt batteries are connected to the ion source, and then remove the 9V battery from the Arduino.
 - Note: Do not leave these batteries connected to the source for extended periods of time while not running the beam to avoid draining the batteries.
- Turn on the *Floating High Voltage Supply* (switch on the far left)
- Turn on the beam deflectors
 - Leftmost switch under “Initial” in *Beam Deflectors* (vertical deflection)
 - Leftmost switch under “El. Field” in *Velocity Filter* (horizontal deflection)
- Turn on “Filament” switch on the right side of the *MIT Ion Source* rack (be careful since switch is not seated properly).
 - Make a note of pressure on channel 1 (active gauge in front of the source)
- Bringing up source current (*MIT Ion Source*):

- For each step below note the time, initial current setting (i.e. before relaxation), and count number on knob. Also **keep an eye on the pressure!** In the event of a pressure spike let everything sit for a while before incrementing the source current.
- Turn dial clockwise until current is ~ 0.5 A. Wait about 10 minutes for stabilization (waiting longer is not detrimental).
- Turn dial clockwise until current is ~ 0.5 A higher than the final stabilized current from the previous step. Wait another 10+ minutes for stabilization.
- Continue incrementing the current in this manner until desired current is reached (~ 2.0 A for Schottky diode experiments)

Troubleshooting – common issues:

- Use high voltage probe and DMM to measure voltage on the isolated part of the source in the acrylic box. (The display for “V-Accel” shows the programmed voltage and not a measured voltage.)
- Use DMM to measure the voltage across the three series 6V batteries (should be around 19V).

Tuning Ion Beam

- Move the Faraday cup so that is in the beam path and connected to the Keithley 617 programmable electrometer for instantaneous current readings.
- Turn the rightmost knob of *Floating High Voltage Supply* so that “V-Accel” is selected. Then use the “V-Accel” knob (top left) to adjust to the desired voltage (Note: this will determine the beam energy, e.g. V-Accel = 1,000 V \rightarrow 1 keV ion beam)
- Turn the rightmost knob of *Floating High Voltage Supply* so that “VF 1” is selected. Then use the “VF 1” knob (top right) to tune the beam in order to maximize beam current. Rule of thumb: VF 1 $\approx 0.75 \cdot$ V-Accel to maximize beam current, e.g. for V-Accel = 1,000 V, VF 1 will probably be around 750 V.
- Use course and fine adjustment knobs (typically fine adjustment only) under “El. Field” in *Velocity Filter* to adjust the horizontal deflection and maximize the current.
- Use course and fine adjustment knobs (typically fine adjustment only) under “Initial” in *Beam Deflectors* to adjust the vertical deflection and maximize the current.
 - Note: Can flip the switch beside the power switch to change the polarity

- Repeat steps to readjust “VF 1”, horizontal deflection, and vertical deflection until there is essentially no further increase in beam current

Note: Reference previous experiments with the same source to see if beam currents are appropriate, but keep in mind that beam current will continually decrease over the life of the source.

Note: Decreasing the beam current (at a given energy) to various percentages of the maximum after completing tuning (as done in Schottky diode experiments) can most easily be achieved by adjusting “VF 1”.

Shutting Down Ion Beam

Note: No time limitations when reducing currents and voltages for shutdown.

- Turn dial for source current (*MIT Ion Source*) back to zero.
- Turn down “V-Accel” (*Floating High Voltage Supply*) to zero for safety.
- Connect 9V battery to the Arduino until the three series 6V batteries are disconnected from the source, and then disconnect the 9V battery from the Arduino.

Stop here if planning to do more experiments the next day otherwise continue.

- Turn down “VF 1” (*Floating High Voltage Supply*) to zero.
- Turn down horizontal deflectors (under “El. Field” in *Velocity Filter*).
- Turn down vertical deflectors (under “Initial” in *Beam Deflectors*).
- Turn off horizontal deflectors
- Turn off vertical deflectors
- Turn off *Floating High Voltage Supply*
- Turn off “Filament” switch of the *MIT Ion Source* (be careful since switch is not seated properly).

Leave system like this if you plan to do more experiments on the currently loaded sample in the next week or two, otherwise turn off pumps and vent chamber (see relevant instructions).

Venting Chamber

Note: Source will be warm after running, so wait **at least 2 hours** for things to cool down before proceeding with venting!

- Turn off pressure gauge for channel 1
- Hit the “stop” button on the orange box below the beamline to stop driving the TMP.
- Close the gate valve (below *Floating High Voltage Supply* rack)
 - Hit red button under plastic guard. Button should be popped out. Should hear gate valve close

- Turn off the power strip on the floor next to the large white box to turn off the mechanical/backing pump.
- Open the ‘*Gold-Seal Valve*’ (near 8 ft-lb label):
 - At first use the appropriate torque wrench
 - Continue to loosen by hand as much as desired
- Open vacuum port door and remove sample

Note: If vacuum port door will not open, then briefly open the green Nupro valve and then close it again (near ‘*Gold-Seal Valve*’). Try again to open the vacuum port door.

Data Collection in LabVIEW for Schottky Diode Experiments

Note: Password is **tiger5** (taped to top of center monitor)

- Open the LabVIEW script from the desktop (*Keithley 24XX Sweep and Acquire File Out - Shortcut*).
- Under “*VISA Resource Name*” select **GPIB 26**
- For “*Source Mode*” select **voltage**
- Select desired values for **compliance**, **min**, **max**, and **# points**.
- Click white arrow in the toolbar to run the IV sweep
- Save data with desired name in the box that pops up

Note: Zero check electrometer before switching connections around throughout the experiment.

D.7 Guide for performing 4-pt probe measurements

1. Turn on the relevant equipment (**Keithley 6221 DC and AC Current Source** and **Keithley 2182A nanovoltmeter**) at least 30 minutes prior to taking measurements to allow the equipment to warm up.
2. Place the sample to be measured on the Teflon disk and center it below the probe tips
 - Note: Larger sample sizes are preferable since they will reduce measurement error.
 - For rectangular samples place the sample such that the larger dimension is parallel to the probe tips.
3. Rotate the lever clockwise as far as it will go in order to lower the probes onto the sample.
 - The height of the probe arm can be adjusted if needed, or glass slides can be used in addition to or in the place of the Teflon plate in order to adjust the sample height.
4. On the nanovoltmeter, select the **DCV1** channel and select **AUTO** for the range.
5. On the current source push the **EDIT/LOCAL** button until the number displayed next to *Compliance*: is flashing. Use the wheel to adjust the compliance to its maximum value of 105 V, and then push the wheel to set the value.
 - Adjust compliance to a lower value if there are concerns about the device breaking down.
6. Set the desired output current on the current source via the following steps:
 - Push the **EDIT/LOCAL** button until the numbers for the current are flashing.
 - Use the wheel and the left and right arrows on either side of *CURSOR* to adjust the current to the desired value. Push the wheel to set the value.
 - Typically a few mA's is a good starting point. Readings obtained using currents smaller than 100 μ A might not be very reliable.
7. Apply the current to the sample by pressing the **OUTPUT ON/OFF** button on the current source.
 - If the blue LED to the right of the button is solid then everything is working as intended.
 - If the blue LED to the right of the button is blinking then the voltage is over the limit. Reduce the current and try again.
8. Read the voltage shown on the nanovoltmeter.

9. Stop applying current by pressing the **OUTPUT ON/OFF** button on the current source.
10. Turn the lever counterclockwise to lift the probe head, and then remove the sample.

Calculating Sheet Resistance

Relevant Variable Names and Fixed Values:

$s \equiv$ probe tip spacing = 0.0625 inches = 0.15875 cm

$\rho \equiv$ sheet resistivity

$t \equiv$ thickness of the sample

$d \equiv$ wafer diameter (for rectangular samples the smaller dimension is used as d)

$V \equiv$ measured voltage

$I \equiv$ measured current

Resistivity is given by the following equation:

$$\rho = \left(\frac{V}{I}\right) * t * CF_1 * CF_2$$

where CF_1 and CF_2 are correction factors as determined by the tables below. If the d/s or t/s values are between two entries in the table, then a simple linear interpolation should be sufficient for a first order approximation of the correction factor. For a more detailed value there are plots for correction factor that can be researched.

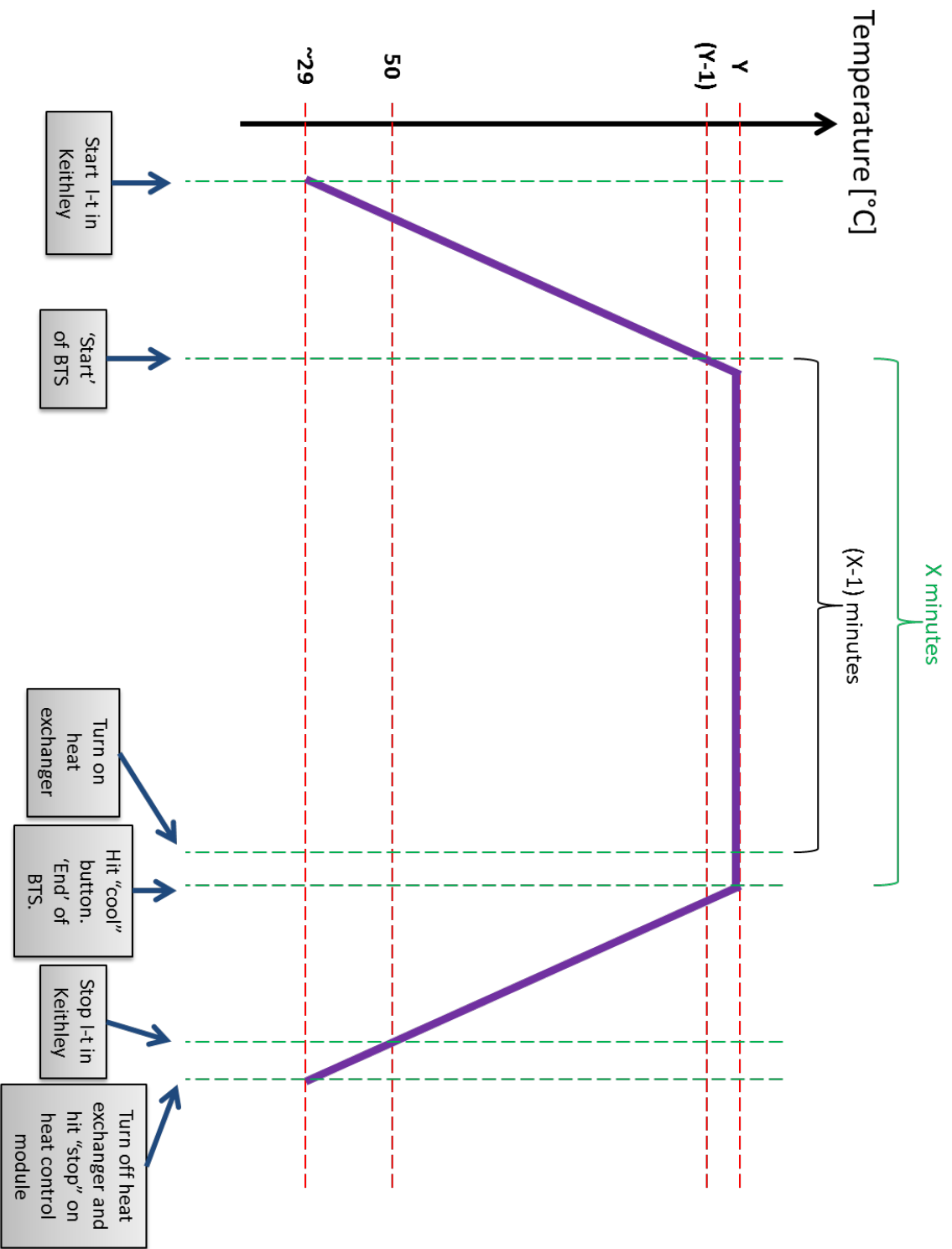
Note: The above equation and correction factor values are only valid for junctions diffused on one side of the sample. Different factors must be used for samples diffused on both sides.

d/s	CF1				
	Circle	Square	Rectangle L/W=2	Rectangle L/W=3	Rectangle L/W=4
1.0	-	-	-	0.9988	0.9994
1.25	-	-	-	1.2467	1.2248
1.5	-	-	1.4788	1.4893	1.4893
1.75	-	-	1.7196	1.7238	1.7238
2.0	-	-	1.9475	1.9475	1.9475
2.5	-	-	2.3532	2.3541	2.3541
3.0	2.2662	2.4575	2.7000	2.7005	2.7005
4.0	2.9289	3.1127	3.2246	3.2248	3.2248
5.0	3.3625	3.5098	3.5749	3.5750	3.5750
7.5	3.9273	4.0095	4.0361	4.0362	4.0362
10.0	4.1716	4.2209	4.2357	4.2357	4.2357
15.0	4.3646	4.3882	4.3947	4.3947	4.3947
20.0	4.4364	4.4516	4.4553	4.4553	4.4553
32.0	4.4791	4.4878	4.4899	4.4899	4.4899
40.0	4.5076	4.5120	4.5129	4.5129	4.5129
infinity	4.5324	4.5324	4.5325	4.5325	4.5324

t/s	CF2
<0.4	1.000
0.400	0.9995
0.500	0.9974
0.555	0.9948
0.625	0.9896
0.714	0.9798
0.833	0.9600
1.000	0.9214
1.111	0.8907
1.250	0.8490
1.429	0.7938
1.667	0.7225
2.000	0.6336

D.8 Guide for performing bias temperature stress (BTS) Measurements

The following diagram was adapted from p. 23 of Daniel Cutshall's #1 lab notebook. The diagram describes how to perform bias temperature stress measurements for samples placed on the chuck in Riggs 11. In the diagram ' X ' is a variable representing the desired time (in minutes) of the BTS procedure, and ' Y ' is a variable representing the temperature (in degrees centigrade) at which the BTS is performed. The procedure was initially described by Radhey Shyam in the summer of 2013.



D.9 Guide for mounting Schottky diode on platen

The platen used for mounting the Schottky diodes was stainless steel and had three posts that were electrically isolated from the platen base by individual insulating rings.

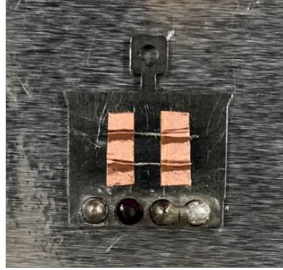
1. Clean the platen with acetone and place two small pieces of 0.25 mm diameter Al wire on the platen as shown in Figure D.9 (a)
2. Secure the two Al wires with double sided Cu tape as shown in Figure D.9 (b)
3. Apply Ag paste/paint to the platen between the Cu tape strips as shown in Figure D.9 (c)
4. Place the Schottky diode on the platen as shown in Figure D.9 (d) and hold in place for ~60 seconds. Allow ~10 minutes to cure before proceeding to the next step
5. Bend a piece of 0.25 mm diameter Al wire such that one end loops around the left most post (ideally the wire sits about half way up the post by itself) and the other end rests on the edge of the Schottky contact. This facilitates contact with the Schottky contact.
6. Apply Ag paste/paint to both ends of the Al wire from the previous step as shown in Figure D.9 (e). Allow ~10 minutes to cure before moving platen and diode
 - a. Note: Minimal overlap with the Schottky contact is preferred to reduce shielding from ion beam
 - b. Note: Typically I attached the post side of the Al wire first, but attaching either end first should work fine
7. Apply Ag paste/paint between the right most post and the platen itself in order to facilitate contact to the backside Ohmic contact as shown in Figure D.9 (f)
 - a. Note: This can be done earlier in the process if desired, and the Ag paste/paint that connects the post to the platen can be left for several samples without needing to clean it off and reapply for each new sample
8. After allowing sufficient time for everything to cure, perform continuity checks for the following:
 - a. Schottky contact connected to left most post
 - b. Right most post connected to platen
 - c. Left most post NOT connected to platen

Note: The Ag paste/paint should be shaken by hand (or somehow mechanically agitated to promote mixing) for a minute or more prior to each application. This ensures good electrical properties.

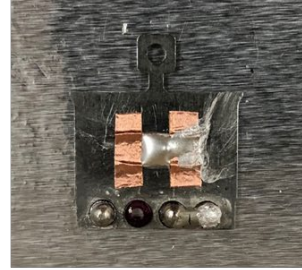
Note: At various times over the years two different products from Ted Pella Inc. were successfully used to mount the diodes: (1) Colloidal Silver Paste, Cat. No. 16032, and (2) Leitsilber 200 Silver Paint, Cat. No. 16035



(a)



(b)



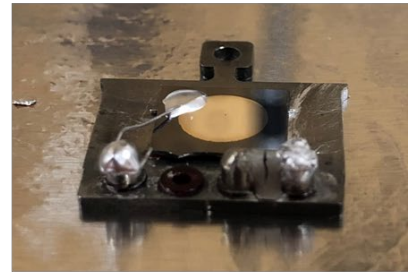
(c)



(d)



(e)



(f)

Figure D.9: Various stages of the Schottky diode mounting procedure.

References

- [1]. F. Issa, V. Vervisch, L. Ottaviani, D. Szalkai, L. Vermeeren, A. Lyoussi, A. Kuznetsov, M. Lazar, A. Klix, O. Palais, and A. Hallen, "Radiation Silicon Carbide Detectors Based on Ion Implantation of Boron," *IEEE Transactions on Nuclear Science*, **Vol. 61**, No. 4, pp. 2105-2111, Aug. 2014.
- [2]. N.I.C. Omar, N.F. Hasbullah, N. Rashid, and J. Abdullah, "Effects on Electrical Characteristics of Commercially Available Si and GaAs Diodes Exposed to Californium-252 Radiation," *International Conference on Computer and Communication Engineering*, pp. 185-189, July 2012.
- [3]. S. Verma, K.C. Praveen, A. Bobby, and D. Kanjilal, "Recovery of Electrical Characteristics of Au/n-Si Schottky Junction Under 60-Co Gamma Irradiation," *IEEE Transactions on Device and Materials Reliability*, **Vol. 14**, No. 2, pp. 721-725, June 2014.
- [4]. A.P. Karmarkar, B.D. White, D. Buttari, D.M. Fleetwood, R.D. Schrimpf, R. A. Weller, L.J. Brillson, and U.K. Mishra, "Proton-Induced Damage in Gallium Nitride-Based Schottky Diodes," *IEEE Transactions on Nuclear Science*, **Vol. 52**, No. 6, pp. 2239-2244, Dec. 2005.
- [5]. P. Mulligan, J. Qiu, J. Wang, and L.R. Cao, "Study of GaN Radiation Sensor After In-core Neutron Irradiation," *IEEE Transactions on Nuclear Science*, **Vol. 61**, No. 4, pp. 2040-2044, Aug. 2014.
- [6]. J.A. Kulisek and T.E. Blue, "Carrier-Removal Comparison (n/p) and Functional Testing of Si and SiC Power Diodes," *IEEE Transactions on Nuclear Science*, **Vol. 57**, no. 5, pp. 2906-2914, Oct. 2010.
- [7]. R.D. Harriss and A.J. Frasca, "Proton Irradiation of Silicon Schottky Barrier Power Diodes," *IEEE Transactions on Nuclear Science*, **Vol. 53**, no. 4, pp. 1995-2003, Aug. 2006.
- [8]. L. Liu, A. Liu, S. Bai, L. Lv, P. Jin, and X. Ouyang, "Radiation Resistance of Silicon Carbide Schottky Diode Detectors in D-T Fusion Neutron Detection," *Nature:Scientific Reports*, **Vol. 7**, Article number 13376, pp. 1-8, Oct. 2017.
- [9]. L.Y. Liu, L. Wang, P. Jin, J.L. Liu, X.P. Zhang, L. Chen, J.F. Zhang, X.P. Ouyang, A. Liu, R.H. Huang, and S. Bai, "The Fabrication and Characterization of Ni/4H-SiC Schottky Diode Radiation Detectors with a Sensitive Area of up to 4 cm²," *Sensors*, **Vol. 17**, Issue 10, p. 2334, Oct. 2017.

- [10]. S. Seshadri, A.R. Dulloo, F.H. Ruddy, J.G. Seidel, and L.B. Rowland, "Demonstration of an SiC Neutron Detector for High-Radiation Environments," *IEEE Transactions on Electron Devices*, **Vol. 46**, No. 3, pp. 567-571, Mar. 1999.
- [11]. J.D. Gillaspay, "Highly charged ions," *Journal of Physics B: Atomic, Molecular and Optical Physics*, **Vol. 34**, No. 19, pp. R93-R130, Sept. 2001.
- [12]. F.W. Meyer, P.R. Harris, C.N. Taylor, H.M. Meyer III, A.F. Barghouty, and J.H. Adams, "Sputtering of lunar regolith simulant by protons and singly and multicharged Ar ions at solar wind energies", *Nuclear Instruments and Methods in Physics Research B*, **Vol. 269**, Issue 11, pp. 1316-1320, June 2011.
- [13]. J.R. Schwank, M.R. Shaneyfelt, and P.E. Dodd, "Radiation Hardness Assurance Testing of Microelectronic Devices and Integrated Circuits: Radiation Environments, Physical Mechanisms, and Foundations for Hardness Assurance", *IEEE Transactions on Nuclear Science*, **Vol. 60**, No. 3, pp. 2074-2100, June 2013.
- [14]. F. Aymayr and H. Winter, "Slow Highly Charged Ions – A New Tool For Surface Nanostructuring?," *e-Journal of Surface Science and Nanotechnology*, **Vol. 1**, pp. 171-174, Dec. 2003.
- [15]. T. Werner, G. Zschornack, F. Grossmann, V.P. Ovsyannikov, and F. Ullmann, "The Dresden EBIT: An ion source for materials research and technological applications of low-energy highly charged ions", *Nuclear Instruments and Methods in Physics Research Section B*, **Vol. 178**, Issues 1-4, pp. 260-264, May 2001.
- [16]. M. Tona, H. Watanabe, S. Takahashi, N. Nakamura, N. Yoshiyasu, M. Sakurai, T. Terui, S. Mashiko, C. Yamada, and S. Ohtani, "Nanofabrication on a Si surface by slow highly charged ion impact", *Nuclear Instruments and Methods in Physics Research B*, **Vol. 256**, Issue 1, pp. 543-546, Mar. 2007.
- [17]. M. Sakurai, M. Tona, S. Takahashi, H. Watanabe N. Nakamura, N. Yoshiyasu, C. Yamada, S. Ohtani, H.A. Sakaue, Y. Kawase, K. Mitsumori, T. Terui, and S. Mashiko, "Nano-scale surface modification of materials with slow, highly charged ion beams", *Nuclear Instruments and Methods in Physics Research B*, **Vol. 257**, Issues 1-2, pp. 297-300, Apr. 2007.
- [18]. J.D. Gillaspay, J.M. Pomeroy, A.C. Perrella, and H. Grube, "The potential of highly charged ions: possible future applications," *Journal of Physics: Conference Series*, **Vol. 58**, pp. 451-456, Aug. 2007.

- [19]. A. Silze, E. Ritter, G. Zsxhornack, A. Schwan, and F. Ullmann, “Investigations of the emittance and brightness of ion beams from an electron beam ion source of the Dresden EBIS type,” *Review of Scientific Instruments*, **Vol. 81**, Issue 2, pp. 023303, Feb. 2010.
- [20]. H. Nienhaus, H.S. Bergh, B. Gergen, A. Majumdar, W.H. Weinberg, and E.W. McFarland, “Electron-Hole Pair Creation at Ag and Cu Surfaces by Adsorption of Atomic Hydrogen and Deuterium”, *Physical Review Letters*, **Vol. 82**, No. 2, pp. 446-449, Jan. 1999.
- [21]. H. Nienhaus, “Electronic excitations by chemical reactions on metal surfaces”, *Surface Science Reports*, **Vol. 45**, Issues 1-2, pp. 1-78, Jan. 2002.
- [22]. F. Becker, D. Krix, U. Hagermann, and H. Nienhaus, “Internal detection of surface plasmon coupled chemiluminescence during chlorination of potassium thin films”, *The Journal of Chemical Physics*, **Vol. 138**, Issue 3, p. 034710, January 2013.
- [23]. U. Hagermann and H. Nienhaus, “Surface plasmon coupled chemiluminescence during adsorption of oxygen on magnesium surfaces”, *The Journal of Chemical Physics*, **Vol. 143**, Issue 24, p. 244703, December 2015.
- [24]. G.F. Knoll, *Radiation Detection and Measurement*, 3rd ed. (John Wiley & Sons, Inc., Hoboken, NJ, USA, 2000).
- [25]. G. Lutz, *Semiconductor Radiation Detectors: Device Physics* (Springer, New York, NY, USA, 1999).
- [26]. S.N. Ahmed, *Physics and Engineering of Radiation Detection*, 1st ed. (Academic Press, London, UK, 2007).
- [27]. C.F.G. Delaney and E.C. Finch, *Radiation Detectors: Physical Principles and Applications* (Oxford University Press, New York, NY, USA, 1992).
- [28]. S. Kumar, Y.S. Katharria, and D. Kanjilal, “Swift heavy ion irradiation-induced defects and electrical characteristics of Au/n-Si Schottky structure”, *Journal of Physics D: Applied Physics*, **Vol. 41**, Number 10, p. 105105, April 2008.
- [29]. I.P. Jain, G. Agarwal, “Ion beam induced surface and interface engineering”, *Surface Science Reports*, **Vol. 66**, Issues 3-4, pp. 77-172, March 2011.
- [30]. ‘NASA Space Science Data Coordinated Archive’. [Online]. Available: <http://nssdc.gsfc.nasa.gov/nmc/spacecraftDisplay.do?id=1966-110A> [Accessed: 09-Feb-2017].

- [31]. ‘Mission Archives: ATS Program’. [Online]. Available: <https://www.nasa.gov/centers/goddard/missions/ats.html> [Accessed: 09-Feb-2017].
- [32]. ‘NASA Space Science Data Coordinated Archive: Telstar 401’. [Online]. Available: <http://nssdc.gsfc.nasa.gov/nmc/spacecraftDisplay.do?id=1993-077A> [Accessed: 09-Feb-2017].
- [33]. ‘AT&T Satellite Malfunction’. [Online]. Available: http://www-istp.gsfc.nasa.gov/istp/cloud_jan97/att.html#rpt3 [Accessed: 09-Feb-2017].
- [34]. H.-L. Lam, D.H. Boteler, B. Burlton, and J. Evans, “Anik-E1 and E2 Satellite failures of January 1994 revisited”, *Space Weather*, **Vol. 10**, Issue 10, Oct. 2012.
- [35]. D.E. Nordell, “Solar Effects on Communications”, *IEEE Power Engineering Review*, **Vol. 11**, No. 9, pp. 6-11, Sept. 1991.
- [36]. Y. Zou and R. Hutton, “Physics Based on Electron Beam Ion Traps,” *Physica Scripta*, **Vol. T120**, pp. 47-52, Jan. 2004.
- [37]. G. Federici, C.H. Skinner, J.N. Brooks, J.P. Coad, C. Grisolia, A.A. Haasz, A. Hassanein, V. Philipps, C.S. Pitcher, J. Roth, W.R. Wampler, and D.G. Whyte, “Plasma-material interactions in current tokamaks and their implications for next step fusion reactors,” *Nuclear Fusion*, **Vol. 41**, No. 12, pp. 1967-2137, Dec. 2001.
- [38]. T. Schenkel, A.V. Hamza, A.V. Barnes, and D.H. Schneider, “Interaction of slow, very highly charged ions with surfaces,” *Progress in Surface Science*, **Vol. 61**, Issues 2-4, pp. 23-84, Jun. 1999.
- [39]. F. Aumayr, S. Facsko, A.S. El-Said, C. Trautmann, and M. Schleberger, “Single ion induced surface nanostructures: a comparison between slow highly charged and swift heavy ions” *Journal of Physics: Condensed Matter*, **Vol. 23**, No. 39, p. 393001, Sept. 2011.
- [40]. J. Burgdörfer, P. Lerner, and F.W. Meyer, “Above-surface neutralization of highly charged ions: The classical over-the-barrier model,” *Physical Review A*, **Vol. 44**, No. 9, pp. 5674-5685, Nov. 1991.
- [41]. R.E. Lake, C.E. Sosolik, and J.M. Pomeroy, “Classical over-the-barrier model for neutralization of highly charged ions above thin dielectric films,” *Physical Review A*, **Vol. 87**, Issue 6, pp. 062901, Jun. 2013.
- [42]. R.E. Lake, J.M. Pomeroy, and C.E. Sosolik, “Critical capture distances for highly charged ions above dielectric covered metal surfaces,” *Nuclear Instruments and Methods in Physics Research B*, **Vol. 269**, Issue 11, pp. 1199-1202, Oct. 2010.

- [43]. R.E. Lake, J.M. Pomeroy, and C.E. Sosolik, “Energy dissipation of highly charged ions on Al oxide films,” *Journal of Physics: Condensed Matter*, **Vol. 22**, No. 8, pp. 084008, Feb. 2010.
- [44]. M. Tona and S. Takahashi, “Highly Charged Ion Beams from the Tokyo EBIT for Applications to Nano-Science and –Technoloty,” *Journal of Physics: Conference Series*, **Vol. 2**, pp. 57-64, Apr. 2004.
- [45]. G. Zschornack, S. Landgraf, F. Großmann, U. Kentsch, V.P. Ovsyannikov, M. Schmidt, and F. Ullmann, “An ion beam facility for HCI-based analysis and materials research,” *Nuclear Instruments and Methods in Physics Research B*, **Vol. 249**, pp. 921-923, May 2006.
- [46]. J.W. McDonald and D.H.G. Schneider, “The next generation refrigerated (cryogenic) electron beam ion trap-source (REBIT-S)”, *Nuclear Instruments and Methods in Physics Research Section B*, **Vol. 241**, Issues 1-4, pp. 870-873, Dec. 2005.
- [47]. M. Tona, H. Watanabe, S. Takahashi, N. Nakamura, N. Yoshiyasu, M. Sakurai, T. Terui, S. Mashiko, C. Yamada, and S. Ohtani, “Nano-crater formation on a Si(111)-(7X7) surface by slow highly charged ion-impact,” *Surface Science*, **Vol. 601**, Issue 3, pp. 723-727, Feb. 2007.
- [48]. R. Ritter, R.A. Wilhelm, R. Ginzler, G. Kowarik, R. Heller, A.S. El-Said, R.M. Papaléo, W. Rupp, J.R. Urrutia, J. Ullrich, S. Facsko, and F. Aumayr, “Pit formation on poly (methyl methacrylate) due to ablation induced by individual slow highly charged ion impact,” *Europhysics Letters*, **Vol. 97**, No. 1, pp. 13001, Jan. 2012.
- [49]. M. Tona, H. Watanabe, S. Takahashi, Y. Fujita, T. Abe, S. Jian, N. Nakamura, N. Yoshiyasu, C. Yamada, M. Sakurai, and S. Ohtani, “Observation of HCI-induced nanostructures with a scanning probe microscope”, *Journal of Physics: Conference Series*, **Vol. 58**, Issue 1, pp. 331-334, 2007.
- [50]. P. Beiersdorfer, E. Behar, K.R. Boyce, G.V. Brown, H. Chen, K.C. Gendreau, A. Graf, M.F. Gu, C.L. Harris, S.M. Kahn, R.L. Kelley, J.K. Lepson, M.J. May, P.A. Neill, E.H. Pinnington, F.S. Porter, A.J. Smith, C.K. Stahle, A.E. Szymkowiak, A. Tillotson, D.B. Thorn, E. Träbert, and B.J. Wargelin, “Overview of the Livermore electron beam ion trap project,” *Nuclear Instruments and Methods in Physics Research B*, **Vol. 205**, pp. 173-177, May 2003.

- [51]. G. Zschornack, S. Landgraf, F. Großmann, U. Kentsch, V.P. Ovsyannikov, M. Schmidt, F. Ullmann, “An ion beam facility for HCI-based analysis and material research”, *Nuclear Instruments and Methods in Physics Research Section B*, **Vol. 249**, Issues 1-2, pp. 921-923, Aug. 2006.
- [52]. G. Zschornack, F. Großmann, R. Heller, U. Kentsch, M. Kreller, S. Landgraf, V.P. Ovsyannikov, M. Schmidt, and F. Ullmann, “Production of highly charged ions for ion-surface interaction studies,” *Nuclear Instruments and Methods in Physics Research B*, **Vol. 258**, Issue 1, pp. 205-208, May 2007.
- [53]. D.D. Kulkarni, C.D. Ahl, A.M. Shore, A.J. Miller, J.E. Harriss, C.E. Sosolik, and J.P. Marler, “Kinetic energy offsets for multicharged ions from an electron beam ion source,” *Review of Scientific Instruments*, **Vol. 88**, Issue 8, pp. 083306, Aug. 2017.
- [54]. K. Kuroki, N. Okabayashi, H. Torii, K. Komaki, and Y. Yamazaki, “Potential sputtering of proton from hydrogen-terminated Si(100) surfaces induced with slow highly charged ions,” *Applied Physics Letters*, **Vol. 81**, No. 19, pp. 3561-3563, Nov. 2002.
- [55]. M. Tona, K. Nagata, S. Takahashi, N. Nakamura, N. Yoshiyasu, M. Sakurai, C. Yamada, and S. Ohtani, “Some characteristics in the interaction of slow highly charge Iq^+ ions with a Si(111) 1X1-H surface,” *Surface Science*, **Vol. 600**, Issue 1, pp. 124-132, Jan. 2006.
- [56]. S. Takahashi, M. Tona, K. Nagata, N. Nakamura, N. Yoshiyasu, C. Yamada, S. Ohtani, and M. Sakurai, “Toward over unity proton sputtering yields from a hydrogen-terminated Si(111) 1X1 surface irradiated by slow highly charged Xe ions,” *Applied Physics Letters*, **Vol. 87**, Issue 6, pp. 063111, Aug. 2005.
- [57]. N. Okabayashi, K. Komaki, and Y. Yamazaki, “Potential sputtering and kinetic sputtering from a water adsorbed Si(100) surface with slow highly charged ions,” *Nuclear Instruments and Methods in Physics Research Section B*, **Vol. 232**, Issues 1-4, pp. 244-248, May 2005.
- [58]. A.V. Hamza, M.W. Newman, P.A. Thielen, H.W.H. Lee, T. Schenkel, J.W. McDonald, and D.H. Schneider, “Light-emitting nanostructures formed by intense, ultrafast electronic excitation in silicon (100),” *Applied Physics Letters*, **Vol. 79**, No. 18, pp. 2973-2975, Oct. 2001.
- [59]. J.E. Sanabia, S.N. Gldie, L.P. Ratliff, L.S. Goldner, and J.D. Gillaspay, “Highly Charged Ion Bombardment of Silicon Surfaces,” *AIP Conference Proceedings*, **Vol. 680**, pp.568-572, Aug. 2003.

- [60]. T. Schenkel, A.V. Hamza, A.V. Barnes, and D.H. Schneider, "Ablation of GaAs by Intense, Ultrafast Electronic Excitation from Highly Charged Ions," *Physical Review Letters*, **Vol. 81**, No. 12, pp. 2590-2593, Sept. 1998.
- [61]. K. Motahashi, S. Tsurubuchi, and A. Koukitu, "Momentum-imaging spectroscopy of secondary ions from GaN and SiC surfaces collided with highly charged ions at grazing angle," *Nuclear Instruments and Methods in Physics Research Section B*, **Vol. 232**, Issues 1-4, pp. 254-260, May 2005.
- [62]. K. Motohashi, K. Hosoya, M. Imano, S. Tsurubuchi, and A. Koukitu, "Analyses of GaN (0001) and (000 $\bar{1}$) surfaces by highly-charged ions," *Surface Science*, **Vol. 601**, Issue 22, pp. 5304-5308, Nov. 2007.
- [63]. Z.L. Qing, Z.C. Hong, Y.Y. Tao, Y.C. Feng, L.B. Sheng, J.Y. Fan, S.Y. Mei, and S.S. Jian, "Surface Erosion of GaN Bombarded by Highly Charged 208Pbq+-Ions," *Chinese Physics Letters*, **Vol. 25**, No. 7, pp. 2670-2673, Jul. 2008.
- [64]. A.S. El-Said, "Nanostructures created in SiO₂ surface: A comparison between the impingement by slow highly charged ions and by swift heavy ions," *Nuclear Instruments and Methods in Physics Research Section B*, **Vol. 282**, pp. 63-67, Jul. 2012.
- [65]. A.S. El-Said, R.A. Wilhelm, R. Heller, S. Facsko, C. Trautmann, and F. Aumayr, "Surface nanostructuring of SrTiO₃ single crystals by slow highly charged ions and swift heavy ions," *Nuclear Instruments and Methods in Physics Research Section B*, **Vol. 269**, Issue 11, pp. 1234-1237, Jun. 2011.
- [66]. M. Tona, Y. Fujita, C. Yamada, and S. Ohtani, "Electronic interaction of individual slow highly charged ions with TiO₂ (110)," *Physical Review B*, **Vol. 77**, Issue 15, pp. 155427, Apr. 2008.
- [67]. T. Schenkel, M. Schneider, M. Hattass, M.W. Newman, A.V. Barnes, A.V. Hamza, D.H. Schneider, R.L. Cicero, and C.E.D. Chidsey, "Electronic desorption of alkyl monolayers from silicon by very highly charged ions" *Journal of Vacuum Science & Technology B*, **Vol. 16**, Issue 6, pp. 3298-3300, Dec. 1998.
- [68]. M. Tona, S. Takahashi, K. Nagata, N. Yoshiyasu, C. Yamada, N. Nakamura, and S. Ohtani, "Coulomb explosion potential sputtering induced by slow highly charged ion impact", *Applied Physics Letters*, **Vol. 87**, Issue 22, pp. 224102, Nov. 2005.
- [69]. M. Tona, K. Nagata, S. Takahashi, N. Nakamura, N. Yoshiyasu, M. Sakurai, C. Yamada, and S. Ohtani, "Secondary ion emission from solid surfaces irradiated with highly charged ions", *Nuclear Instruments and Methods in Physics Research B*, **Vol. 232**, Issues 1-4, pp. 249-253, May 2005.

- [70]. M. Tona, H. Watanabe, S. Takahashi, N. Nakamura, N. Yoshiyasu, M. Sakurai, C. Yamada, and S. Ohtani, "Potential sputtering from a Si surface by very highly charged ion impact", *Nuclear Instruments and Methods in Physics Research B*, **Vol. 258**, Issue 1, pp. 163-166, May 2007.
- [71]. M. Sporn, G. Libiseller, T. Neidhart, M. Schmid, F. Aymayr, HP. Winter, and P. Varga, "Potential Sputtering of Clean SiO₂ by Slow Highly Charged Ions", *Physical Review Letters*, **Vol. 79**, No. 5, pp. 945-948, Aug. 1997.
- [72]. G. Borsoni, V. Le Roux, R. Laffitte, S. Kerdilès, N. Béchu, L. Vallier, M.L. Korwin-Pawlowski, C. Vannuffel, F. Bertin, C. Vergnaud, A. Chabli, C. Wyon, "Ultrathin SiO₂ layers formation by ultraslow single- and multicharged ions", *Solid-State Electronics*, **Vol. 46**, Issue 11, pp. 1855-1862, Nov. 2002.
- [73]. T.P. Ma and P.V. Dressendorfer, *Ionizing Radiation Effects in MOS Devices and Circuits* (Wiley, Chichester, NY, USA, 1989).
- [74]. S.M. Sze and K.K. Ng, *Physics of Semiconductor Devices*, 3rd ed. (Wiley, Hoboken, NJ, USA, 2007).
- [75]. R. Shyam, D.D. Kulkarni, D.A. Field, E.S. Srinadhu, D.B. Cutshall, W.R. Harrell, J.E. Harriss, and C.E. Sosolik, "First multicharged ion irradiation results from the CUEBIT facility at Clemson University," *AIP Conf. Proc.*, **Vol. 1640**, Issue 1, pp. 129-135, Jan. 2015.
- [76]. D.D. Kulkarni, R.E. Shyam, D.B. Cutshall, D.A. Field, J.E. Harriss, W.R. Harrell, and C.E. Sosolik, "Tracking subsurface ion radiation damage with metal-oxide-semiconductor device encapsulation," *J. Mater. Res.*, **Vol. 30**, No. 9, pp. 1413-1421, May 2015.
- [77]. D.B. Cutshall, D.D. Kulkarni, A.J. Miller, J.E. Harriss, W.R. Harrell, and C.E. Sosolik, "Tracking ion irradiation effects using buried interface devices," *Nucl. Instr. Meth. Phys. Res. B*, **Vol. 422**, pp. 47-49, Feb. 2018.
- [78]. D.B. Cutshall, D.D. Kulkarni, J.E. Harriss, D.A. Field, C.E. Sosolik, and W.R. Harrell, "Effects of slow highly charged ion irradiation on metal oxide semiconductor capacitors," *Journal of Vacuum Science and Technology B*, vol. 36, issue 5, pp. 052901-1:7, July 2018.
- [79]. D.K. Schroder, *Semiconductor Material and Device Characterization*, 2nd ed. (Wiley, New York, NY, USA, 1998).
- [80]. J.P. Colinge and C.A. Colinge, *Physics of Semiconductor Devices*, (Kluwer Academic Publishers, Norwell, MA, USA, 2002).

- [81]. J.F. Conley Jr. and P.M. Lenahan, "Molecular hydrogen, E' center hole traps, and radiation induced interface traps in MOS devices," *IEEE Trans. Nucl. Sci.*, **Vol. 40**, No. 6, pp. 1335-1340, Dec. 1993.
- [82]. P.M. Lenahan and J.F. Conley Jr., "A comprehensive physically based predictive model for radiation damage in MOS systems," *IEEE Trans. Nucl. Sci.*, **Vol. 45**, No. 6, pp. 2413-2423, Dec. 1998.
- [83]. B.R. Tuttle, D.R. Hughart, R.D. Schrimpf, D.M. Fleetwood, and S.T. Pantelides, "Defect interactions of H₂ in SiO₂: implications for ELDRS and latent interface trap buildup," *IEEE Trans. Nucl. Sci.*, **Vol. 57**, No. 6, pp. 3046-3053, Dec. 2010.
- [84]. F.B. McLean, "A framework for understanding radiation-induced interface states in SiO₂ MOS structure," *IEEE Trans. Nucl. Sci.*, **Vol. NS-27**, No. 6, pp. 1651-1657, Dec. 1980.
- [85]. D.M. Fleetwood, "Effects of hydrogen transport and reactions on microelectronics radiation response and reliability," *Microelectron. Reliab.*, **Vol. 42**, Issues 4-5, pp. 523-541, Jan. 2002.
- [86]. S.N. Rashkeev, D.M. Fleetwood, R.D. Schrimpf, and S.T. Pantelides, "Defect generation by hydrogen at the Si-SiO₂ interface," *Phys. Rev. Lett.*, **Vol. 87**, No. 16, pp. 165506-1 – 165506-4, Oct. 2001.
- [87]. W.L. Warren, M.R. Shaneyfelt, D.M. Fleetwood, J.R. Shwank, and P.S. Winokur, "Microscopic nature of border traps in MOS oxides," *IEEE Trans. Nucl. Sci.*, **Vol. 41**, No. 6, pp. 1817-1827, Dec. 1994.
- [88]. W. Ensinger, "Modification of materials by irradiation of heavy ions with energies from keV to GeV," *Radiat. Meas.*, **Vol. 40**, Issues 2-6, pp. 712-721, Nov. 2005.
- [89]. R.C. Hughes, "Hole mobility and transport in thin SiO₂ films," *Appl. Phys. Lett.*, **Vol. 26**, No. 8, pp. 436-438, Apr. 1975.
- [90]. J. F. Ziegler, J. P. Biersack, and U. Littmark. The stopping and range of ions in matter. Pergamon, New York, 1985.
- [91]. P.M. Lenahan, "Atomic scale defects involved in MOS reliability problems," *Microelectron. Eng.*, **Vol. 69**, Issues 2-4, pp. 173-181, Sep. 2003.
- [92]. R. Singh, S.K. Arora, and D. Kanjilal, "Swift heavy ion irradiation induced modification of electrical characteristics of Au/n-Si Schottky barrier diode," *Mater. Sci. Semicond. Process.*, **Vol. 4**, Issue 5, pp. 425-432, Oct. 2001.

- [93]. S. Verma, K.C. Praveen, T. Kumar, and D. Kanjilal, "In Situ investigation of current transport across Pt/n-Si (100) Schottky junction during 100 MeV Ni⁺⁷ ion irradiation," *IEEE Trans. Device Mater. Rel.*, **Vol. 13**, No. 1, pp. 98-102, Mar. 2013.
- [94]. S. Kumar, Y.S. Katharria, Y. Batra, and D. Kanjilal, "Influence of swift heavy ion irradiation on electrical characteristics of Au/n-Si (100) Schottky barrier structure," *J. Phys. D: Appl. Phys.*, **Vol. 40**, Number 22, pp. 6892-6897, Nov. 2007.
- [95]. A. Bobby, N. Shiwakoti, P.M. Sarun, S. Verma, K. Asokan, B.K. Antony, "Swift heavy ion induced capacitance and dielectric properties of Ni/n-GaAs Schottky diode," *Curr. Appl. Phys.*, **Vol. 15**, Issue 11, pp. 1500-1505, Nov. 2015.
- [96]. R.A. Wilhelm, E. Gruber, R. Ritter, R. Heller, S. Facsko, and F. Aumayr, "Charge exchange and energy loss of slow highly charged ions in 1 nm thick carbon nanomembranes," *Phys. Rev. Lett.*, **Vol. 112**, Issues 15-18, pp. 153201-1 – 153201-5, Apr. 2014.
- [97]. R.K. Chauhan and P. Chakrabarti, "Effect of ionizing radiation on MOS capacitors," *Microelectron. J.*, **Vol. 33**, Issue 3, pp. 197-203, Mar. 2002.
- [98]. M.P. Ray, R.E. Lake, S.A. Moody, V. Magadala, and C.E. Sosolik, "A hyperthermal energy ion beamline for probing hot electron chemistry at surfaces", *Review of Scientific Instruments*, **Vol. 79**, Issue 7, pp. 076106, Jun. 2008.
- [99]. R.A. Baragiola, "Principles and mechanisms of ion induced electron emission", *Nuclear Instruments and Methods in Physics Research B*, **Vol. 78**, Issues 1-4, pp. 223-238, May 1993.
- [100]. J.W. Mitchell and R.G. Goodrich, "Fermi velocities in silver: Surface Landau-level resonances", *Physical Review B*, **Vol. 32**, No. 8, pp. 4969-4976, Oct. 1985.
- [101]. G. Wilson and J.R. Dennison, "Approximation of Range in Materials as a Function of Incident Electron Energy", *IEEE Trans. on Plasma Sci.*, **Vol. 40**, Issue 2, pp. 305-310, Feb. 2012.
- [102]. M.P. Ray, R.E. Lake, C.E. Sosolik, L.B. Thomsen, G. Nielson, I. Chorkendorff, and O. Hansen, "Subsurface excitations in a metal", *Physical Review B*, **Vol. 80**, Issue 16, pp. 161405, Oct. 2009.
- [103]. 'Fermi Energies, Fermi Temperatures, and Fermi Velocities'. [Online]. Available: <http://hyperphysics.phy-astr.gsu.edu/hbase/Tables/fermi.html> [Accessed: 16-Mar-2019].

- [104]. F. Nava, A. Castaldini, A. Cavallini, P. Errani, and V. Cindro, "Radiation Detection Properties of 4H-SiC Schottky Diodes Irradiated Up to 10^{16} n/cm² by 1 MeV Neutrons," *IEEE Transactions on Nuclear Science*, **Vol. 53**, no. 5, pp. 2977-2982, Oct. 2006.
- [105]. S. Hisamoto, J. Liang, and N. Shigekawa, "Effects of Ar beam irradiation on Si-Based Schottky contacts," *2016 IEEE International Meeting for Future of Electron Devices*, Kansai, June 2016.
- [106]. R. Singh, S.K. Arora, J.P. Singh, F. Singh, and D. Kanjilal, "Swift heavy ion irradiation induced modification of current-voltage characteristics of heavily doped Au/n-GaAs Schottky diode," *2000 International Semiconducting and Insulating Materials Conference*, pp. 167-170, July 2000.
- [107]. Y. Inuzuka, M. Imaizumi, N. Chandrasekaran, M. Nishigaki, H. Taguchi, T. Soga, T. Jimbo, and S. Matsuda, "High Radiation Tolerant GaAs on Si Substrate for Space Solar Cell," *3rd World Conference on Photovoltaic Energy Conversion*, pp. 705-708, May 2003.
- [108]. L'. Stuchlíková, L. Harmatha, D. Búc, J. Benkovská, B. Hlinka, G.G. Siu, "4H-SiC Diode with a RuOx and RuWOx Schottky Contact Irradiated by Fast Electrons," *2006 International Conference on Advanced Semiconductor Devices and Microsystems*, Oct. 2006.
- [109]. M. Pattabi, S. Krishnan, Ganesh, and X. Mathew, "Effect of temperature and electron irradiation on the I-V characteristics of Au/CdTe Schottky diodes", *Solar Energy*, **Vol. 81**, Issue 1, pp. 111-116, January 2007.
- [110]. J. Zhang, I. Pintlilie, E. Fretwurst, R. Klanner, H. Perrey, and J. Schwandt, "Study of radiation damage induced by 12 keV X-rays in MOS structures built on high-resistivity n-type silicon" *Journal of Synchrotron Radiation*, **Vol. 19**, pp. 340-346, January 2012.
- [111]. A. Castaldini, A. Cavallini, L. Rigutti, and F. Nava, "Low temperature annealing of electron irradiation induced defects in 4H-SiC", *Applied Physics Letters*, **Vol. 85**, No. 17, pp. 3780-3782, October 2004.